Investigation of Tunable Parameters Influence on Optimized Hybridization Gap in $In_xGa_{1-x}As/Ga_yIn_{1-y}Sb$ Quantum Well Heterostructures

A thesis submitted by

Xikai Xie

in partial fulfillment of the

requirements for the degree of

Master of Science

in

Materials Science and Engineering

Tufts University

May 2025

advised by

Dr. Paul J. Simmonds

Abstract of the Thesis

Investigation of Tunable Parameters Influence on Optimized Hybridization Gap in

$In_xGa_{1-x}As/GayIn_{1-y}Sb$ Quantum Well Heterostructures

by

Xikai Xie

Master of Science

in

Materials Science and Engineering

Tufts University

2025

Quantum spin Hall insulators (QSHIs) are advanced materials with topologically protected surface states that allow electronic transport without scattering from defects. QSHIs with a large energy gap in the topological phase are of great interest for the development of both quantum and electronic devices. The ability to control the topological phase transition in a QSHI would represent a functional improvement for applications that require in-situ tunability of the material's topological properties such as spintronics and fault-tolerant quantum computing.

It is possible to induce topological states in III-V semiconductor quantum wells (QWs) with a broken-gap band alignment and use the quantum well width to adjust the size of the hybridization energy gap. QSHIs consisting of InGaAs/GaInSb quantum well heterostructures are particularly interesting since by changing the well widths we can control the degree of band inversion and corresponding topological properties. Furthermore, the ability to tune the strain in these structures by varying the composition of both the ternary InGaAs and GaInSb quantum well can enhance the size of the hybridization gap energy between the topological states compared to QSHIs based on binary InAs/GaSb QWs.

We have therefore investigated topological phase transitions in $In_xGa_{1-x}As/Ga_yIn_{1-y}Sb$ quantum well heterostructures by varying different structural parameters. By simulating band topology and topological invariants we can observe changes in wavefunction in reciprocal space and control the quantized responses of the material. Two key parameters that shape a material's band structure are symmetry and strain. We analyzed (111)-oriented III-V semiconductor QW heterostructures under both compressive and tensile strain to explore their effects on the emergent topological states.

We have therefore carried out computational modeling and simulation to investigate InGaAs/GaInSb double QW heterostructures with a (111) crystalline orientation. Our results show how tunable parameters such as quantum well width and strain influence topological band structure.

Contents

List of Figures

List of Tables

Acknowledgements

First and foremost, I would like to express my sincere appreciation to my advisor Professor Paul Simmonds for his advice and support through my Master's academic career. I wouldn't be able to complete this research work without his mentoring.

I would like take this opportunity to thank to Jimmy, who has provided numerous help and suggestion to me since I started with this project. He gave a lot of valuable suggestions based on the perspective of realistic growth condition. I also would like to thank Ethan, who supports simulations for this project.

I would like to thank Professor Aseema Mohanty, Professor Mary Jane Shultz, and the department Chair Professor Thomas Vandervelde for their academic support.

My family have always been supportive through my academic career, and I would like to take this opportunity to thank everyone of them.

1 Introduction

The discovery of topological insulators has revealed a new quantum phase of matter characterized by an insulating bulk and conducting boundaries. Unlike normal insulators, topological insulators possess electronic states at their surfaces or edges that are protected by fundamental symmetries that lead to robust conduction channels immune to scattering from certain types of disorder [1]. In two-dimensional (2D) systems, the quantum spin Hall insulator (QSHI) [2], is a time-reversal-invariant topological insulator with one-dimensional edge states [3]. The QSHI phase has an insulating energy gap in the bulk but supports gapless edge modes that carry charge and spin in a helical manner (opposite spins counter-propagate). This phase is associated with a topological order that distinguishes it from a normal insulator where 2-D band structures fall into two classes that cannot be smoothly deformed into each other without closing the energy gap [3]. A 2-D topological insulator must have topologically protected edge conduction [2]. Backscattering of electrons on a given edge is forbidden without a spin flip due to the helical nature of the edge modes that require antiparallel spins to travel in opposite directions. This property enables dissipationless transport of spin and charge along the edges of a QSHI without an external magnetic field, which makes it an ideal material for spintronics, a proposed approach for low-power electronics that relies on the manipulation of electron spin in solid-state materials [4], to enable for spin currents flowing without energy loss. Therefore, QSHIs represent both a fundamentally intriguing state of matter, and a platform for novel device applications.

The quantum spin Hall effect (QSHE) has been demonstrated in a HgTe/CdTe semiconductor quantum well heterostructure that could achieve a band inversion as a function of quantum well thickness, leading to a QSHI phase [5]. While HgTe quantum wells showed the

existence of the QSHI phase, this material system also has its limitations. The bandgap in the inverted HgTe/CdTe wells is relatively small—just a few meV—that appears due to a delicate band inversion near the Γ-point of the Brillouin zone [5]. The QSHI behavior in HgTe was only observed at cryogenic temperatures (~30 mK), meaning that thermally excited carriers can populate the edge states at higher temperatures due to the small gap, which eliminates quantized conductance [5]. Moreover, HgTe faces the challenge that Hg-based semiconductor compounds are less commonly used for electronic applications than mainstream III-V semiconductor technology, and they also have problems of stability and lattice matching. The HgTe/CdTe system required much more precise control because the interface quality and disorder could limit the edge state mean free path [2,5]. Although HgTe wells proved the QSHI concept, their operating temperature was extremely low, and scaling to practical devices seemed difficult with this material combination. This motivated the search for alternative QSHI platforms with larger bandgaps and composed from more conventional semiconductors.

Other semiconductor quantum well (QW) heterostructures with a broken gap band alignment could exhibit a similar inverted band alignment. One such system is the InAs/GaSb composite QW heterostructure where an InAs QW is coupled to a GaSb [6]. In bulk form, InAs has a small direct bandgap of 0.35 eV and GaSb has a larger gap of 0.73 eV. When layered as a thin QW pair, the confined electrons states in the conduction band of InAs can lie below the confined hole states in the valence band of GaSb, which leads to an overlap at the interface between electron states in InAs and hole states in GaSb that inverts the band structure. The overlap opens a hybridization gap when the electron and hole states tunnel into each other, similar to the band inversion in HgTe [7]. The advantage of the InAs/GaSb system is that it is composed of III-V semiconductors, which are well-studied in the context of high-speed

electronics and optoelectronics for easier integration with existing devices. However, the InAs/GaSb system also has problems including the fact that InAs/GaSb bilayers are semimetallic and need an external gate electric field to align the bands and open a partial gap [7,8]. The hybridization gap in the binary InAs/GaSb system is also small (~3 meV) [7], similar to the HgTe/CdTe QW heterostructure. Although the InAs/GaSb QW heterostructure confirmed that the QSHI phase is not unique to HgTe, and showed more design space for future improvement, it was unable to deliver a large, robust topological energy gap for practical operation.

Given the limitations of HgTe and binary InAs/GaSb quantum wells, identifying and engineering tunable heterostructures that could achieve a larger band inversion gap while maintaining crystalline quality is the top priority. One potential method is to use alloyed III-V semiconductors to adjust both the QW band energies and lattice parameters. Experimental work from [8] demonstrated that using a strained InAs/$Ga_{0.6}In_{0.4}Sb$ composite QW could achieve a topological energy gap of about -35 meV in the QSHI regime, i.e., ten times larger than the binary InAs/GaSb QW heterostructure. Although this gap size is still relatively small, such a proportionally large increase indicates a major step toward practical applications. But despite these developments, several challenges must be addressed when moving to alloyed heterostructures. Introducing ternary compounds could increase carrier scattering that due to alloy disorder, and they often require one to consider strain in the layers due to lattice mismatch. In the InAs/GaSb system, the lattice constants are already slightly different, and adding Ga or In will only serve to increase the lattice mismatch between the two QWs [9]. Growing a coherent multilayer stack requires careful consideration of how each layer is strained to match the others. If the strain is too large or the layer is too thick, the crystal will relax by forming defects such as misfit dislocations, which destroy the electronic properties [10]. A classic result in heteroepitaxy

is to provide an estimate of the critical thickness beyond which a strained film will create dislocations to relieve strain [10]. Exceeding the critical thickness would introduce defects that negatively impact the bulk insulation and scatter the edge states to damage the topological protection. Therefore, a central materials challenge is to design a QW heterostructure such that a large band inversion can be achieved without exceeding the critical thickness limits for coherent growth.

Motivated by the current challenges of InAs/GaSb binary or InAs/GaInSb binary/ternary QW heterostructures, the focus of this thesis to investigate ternary/ternary $In_xGa_{1-x}As/Ga_yIn_{1-y}Sb$ QW heterostructures with different thicknesses and compositions, where x and y are the respective alloy contents of In and Ga ranging from 0 to 1 in the step of 0.1. By incorporating Ga into the InAs layer and In into the GaSb layer, we are able to manipulate the band gap and band alignment of each layer. This material system generalizes the InAs/GaSb QW heterostructure by allowing one to tune the energy band edges through alloy composition and quantum confinement effects via QW thickness. The objective is to find a combination of x, y, and specific QW thickness for both $In_xGa_{1-x}As$ and $Ga_yIn_{1-y}Sb$ that produces the largest hybridization gap without strain relaxation. To achieve this goal, we explore the detailed theoretical background of topological insulators in Chapter 2 through a discussion of the formal definition of topological invariants and the physical implications for electronic band structures. We discuss the topological invariant in 2D systems and review the fundamental properties of QSHIs that include edge state protection and helical conduction. In Chapter 3 we break down the physical and mathematical framework of QWs, explaining how quantum confinement and band alignment can be used to achieve the inverted band structures necessary for the QSHI phase. We review historical QSHI material systems, starting with HgTe/CdTe QWs and their experimental signatures, and then

discuss the InAs/GaSb related system. The limitations of these early systems are analyzed to motivate the exploration of our ternary heterostructure design. We then present the $In_xGa_{1-x}As/Ga_yIn_{1-y}Sb$ QW heterostructure as our proposed solution by describing how band structure engineering and strain management could overcome previous challenges. In Chapter 4 we discuss the epitaxial growth of QWs with atomic precision using Molecular Beam Epitaxy (MBE), as well as introducing the concept of strain due to lattice mismatch. We explain the model for critical thickness calculations applied to our specific material system to predict the maximum allowable thickness for the QW layers with various compositions. This analysis informs the design space for our simulations by ruling out combinations that would likely relax via defect formation. In Chapter 5 we introduce the computational methods used in our study. We introduce the NextNano software package to perform self-consistent Schrödinger-Poisson and k·p calculations of the band structure in our QW heterostructures. The setup of the simulation framework for $In_xGa_{1-x}As/Ga_yIn_{1-y}Sb$ is also described with the material parameters and how they are interpolated for alloy compositions. We also introduce a custom MATLAB routine for interpolating critical thickness as a function of composition, which integrates with the NextNano results to eliminate results that are incompatible with our calculated critical thicknesses. Chapter 6 coves initial simulations of a simpler QW material system. We examined InAs/ $Ga_{0.68}In_{0.32}Sb$ QWs heterostructures for two different crystal orientations: (001) vs. (111) substrates. These simualtions show how substrate orientation, in addition to InAs QW thickness (for a fixed GaInSb composition) affects the band structure, and allow us to determine the point at which the system transitions from a trivial to a topological phase. We also show the $InAs/Ga_xIn_{1-x}Sb$ results for fixed QW thicknesses and varied alloy composition in GaInSb.

In Chapter 7 we cover the key results from this thesis. We explore a range of In (x) and Ga (y) compositions and layer thicknesses to show where the QSHI phase is expected. The first part of the chapter focuses on critical thickness results. We calculate the critical thickness for various alloy fractions to eliminate which combinations of x, y, and individual QW thickness in the $In_xGa_{1-x}As/Ga_yIn_{1-y}Sb$ heterostructure can be physically achieved without dislocations. The second part of the chapter details the band structure simulations across 4–9 nm QW thicknesses and varying compositions. We identify the emergence of a hybridization gap and determine its magnitude for each case, and we present the ten largest hybridization gap results along with their corresponding thickness and composition. Plots of the band structures are shown to illustrate the gaps that indicate a topological phase transition. We also compare our findings with past experimental results. The thesis closes in Chapter 8 with a summary of the key findings and their implications. We highlight how our simulations have allowed us to identify candidate heterostructures that could offer an improved QSHI phase and discuss the remaining challenges for practical experiments and potential future improvements.

2 Topological Insulators

A topological insulator (TI) is a quantum state of matter characterized by an insulating bulk and protected conducting boundary states [1]. Compared to conventional insulators, a TI's electronic structure possesses a non-trivial topology from strong spin-orbit coupling (SOC) and time-reversal symmetry (TRS) [2–4,11]. The topology implies the existence of robust surface or edge states that remain conductive when non-magnetic disorder is present in the surrounding environment [12]. The differences between trivial and topological phases are known as topological invariants, which are global properties of the band structure that cannot be affected without closing the energy gap [1,12]. Up to today, there are many types of topological insulators that have been characterized by their unique topological properties. The focus of this study will be on Quantum Spin Hall Insulators (QSHIs) based on their topological properties of the Quantum Spin Hall effect (QSHE).

This chapter introduces the fundamental concept of topological insulators. In section 2.1, we will be introducing the concept of topology and its application to condensed matter physics. To continue, we will be introducing the topological insulator in section 2.2, explaining the detailed physics in section 2.2.1 and its unique properties in section 2.2.2. Afterwards, we will explain the QSHE and how it has been used to create the QSHI in section 2.3, along with their applications that motivate this study.

2.1 Definition of Topology

Topology originated as a mathematical concept. It is the study of a geometric object's properties that remain invariant under continuous deformations such as stretching or bending. In addition, topology excludes plastic deformation that will break the uniformity of the geometric object's

property such as tearing or gluing [2,13]. For instance, a doughnut and a coffee cup, illustrated in Figure *1*, are topologically equivalent because they both have one hole. However, if the doughnut is torn to pieces, it is no longer topologically equivalent to the coffee cup because the doughnut has undergone a plastic deformation. In condensed matter physics, topology refers to the global structure of the electronic band structure and the properties of the quantum wavefunction that remain invariant under smooth deformations of the Hamiltonian [14], shown in Figure 2. By enabling this unique property within a material, it becomes a topological insulator. A material is a topological insulator if its bulk bands exhibit a non-trivial topology enabled by the inverted bandgap, which occurs when the first electron state energy in the conduction band is lower than the lowest hole state energy, typically the heavy-hole (HH) state, in the valence band [8]. As a result, the material cannot be transformed into a conventional insulator without closing the energy gap. This non-triviality is quantified by topological invariants, such as the Chern number in the integer quantum Hall effect or the $\mathbb{Z}_2$ invariant in time-reversal symmetric systems.

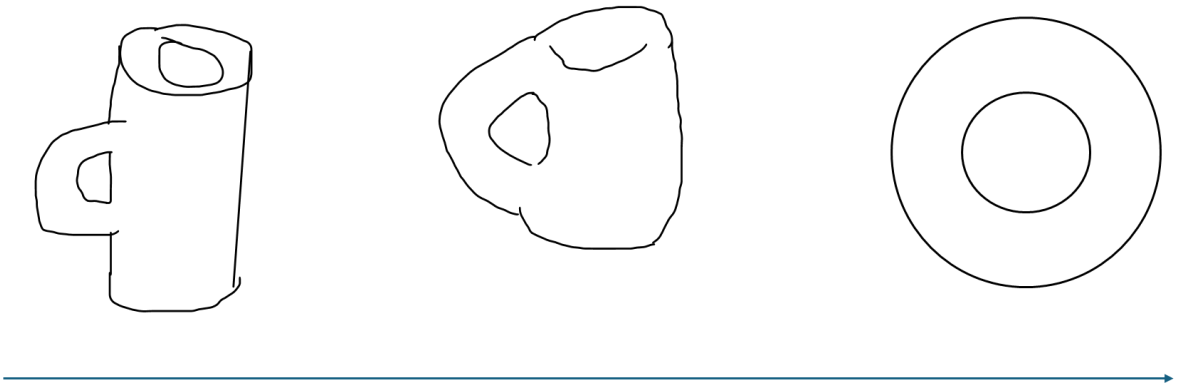

Figure 1: Schematic analogy of a topological effect. A rubber coffee cup could continuously transform into a doughnut without breaking its geometric properties.

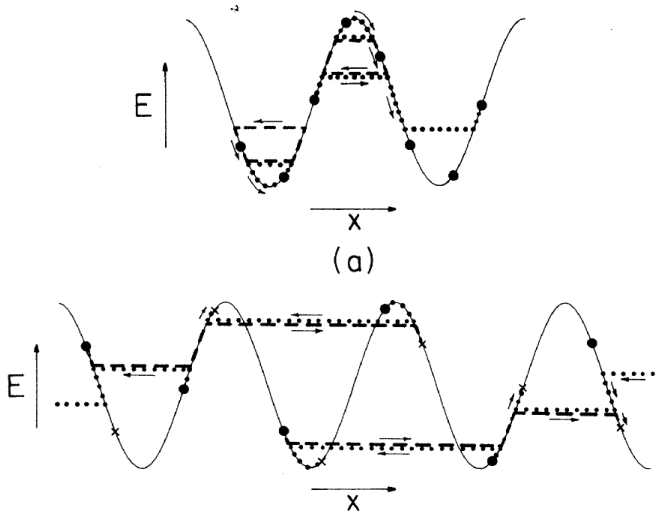

Figure 2: Symmetrical Quantum Wave Function [14].

2.2 Topological Insulators

The TI represents a novel quantum phase of matter that is characterized by the duality of insulating bulk and symmetry-protected conducting boundary states. The insulating bulk characteristic enables conducting edges or surfaces while keeping the inside of the material insulating, which means electricity can't flow through the inside, but it can move along the boundaries. By utilizing this property, a TI is able to allow electronic transport along the edge that is immune to scattering from impurities and defects. Unlike conventional insulators, this separation is from the intrinsic topology of the electronic band structure, governed by invariants such as the Chern number in quantum Hall systems or the $\mathbb{Z}_2$ index in time-reversal symmetry (TRS) materials [3,12]. These invariants are rooted in geometric phases like the Berry curvature that classify phases as trivial or non-trivial, with the latter hosting robust edge or surface states immune to disorder [15]. The defining principle is known as bulk-boundary correspondence, which ensures that non-trivial bulk topology guarantees gapless boundary modes, such as the conducting edge states in 2D quantum spin Hall insulators or Dirac fermions on 3D TI

surfaces[16]. The bulk-boundary correspondence in topological physics is defined as the direct connection between the topological invariants of a material's bulk to the existence and nature of its boundary states. These boundary states are robust against symmetry-preserving perturbations, such as non-magnetic disorder by the protection from its global nature of the bulk topology. The protection is from spin-momentum locking where an electron's spin orientation is coupled to its momentum direction due to strong spin-orbit coupling effects. In TIs, spin-momentum coupling impacts the valence-band structure in strained semiconductor quantum wells by introducing additional coupling between heavy-hole, light-hole, and spin-orbit split-off bands [1,2,8]. This coupling modifies energy dispersion and the effective masses to connect electron spin states to their momentum. Without closing the energy gap, the bulk-boundary correspondence secures the impossibility of smoothly deforming a non-trivial bulk band structure into a trivial bulk band structure [3]. At an interface between topologically distinct phases, for example between a TI and vacuum, the discontinuity in the bulk invariant forces the appearance of gapless boundary modes. A previous study showed a gate-controlled band inversion could create dynamic tuning of the bulk topology in InAs/InGaSb composite quantum wells. A topological phase transition closes the bulk gap and eliminates the protected edge states [3]. Key to this behavior are spin-orbit interactions and symmetries like TRS that enforces spin-momentum locking and the Kramers degeneracy, shown in Figure 3 [17]. The symmetry serves two purposes: a protection mechanism for topological phases that require specific symmetries for their protection, and topological phase classification for defining the variety of possible phases [2]. Recent advances in strain engineering and electric field tuning have enabled more flexible control of energy gaps and topological phase transitions and illustrate the connection between material design and quantum properties [8,18,19]. The coordination between unique combinations of robust

transport, tunability, and topological protection positions TIs as a landmark for exploring emergent phenomena in spintronics, quantum optics, and next-generation technologies such as quantum computing [20].

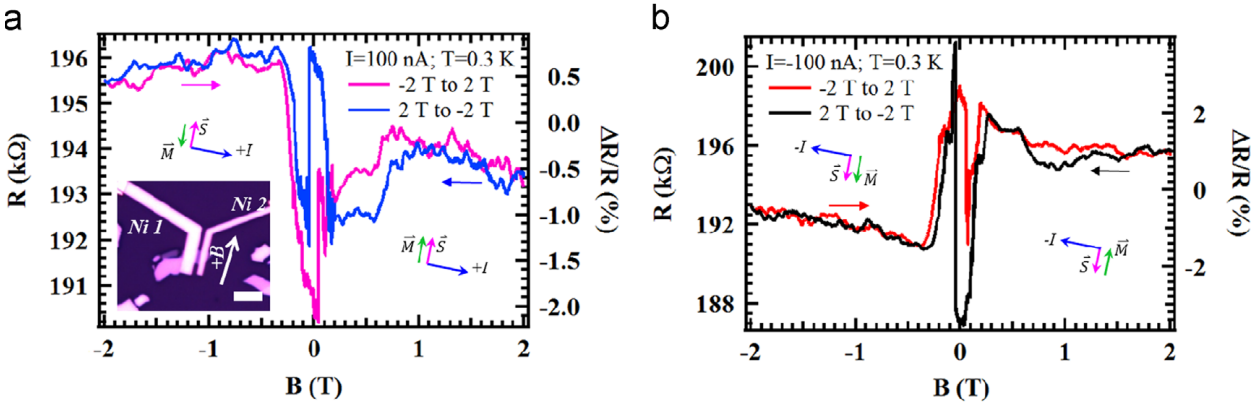

Figure 3: (a,b) Spin-momentum locking observation. Magnetoresistance (MR) measured from an exfoliated 12 nm thick Bi_2Se_3 thin film with a DC current (I= ± 7100 nA) in both directions at T=0.3 K. A MR asymmetry (between large +B and -B fields) is clearly observed [17].

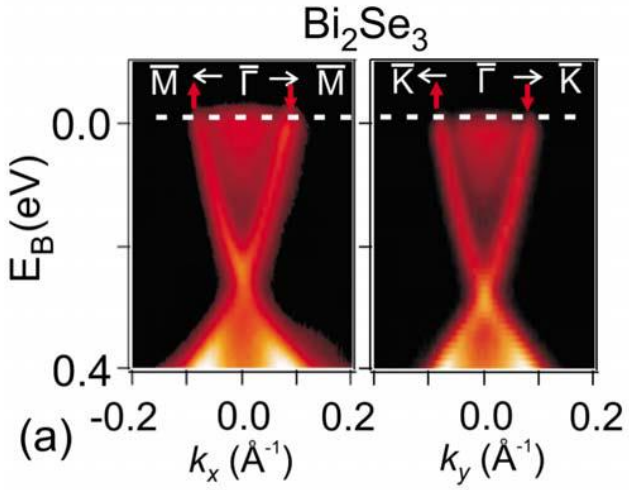

Figure 4: Angle-resolved photoemission spectroscopy (ARPES) data for Bi_2Se_3 reveal surface electronic states with a single spin-polarized Dirac cone [2].

2.2.1 Mathematical concept of topological insulator

Topology classifies phases of matter based on global properties of the quantum wavefunction that remain invariant under smooth deformations of the Hamiltonian, provided the energy gap remains open in TIs. While the bulk of TIs behaves as a normal insulator with a full energy gap, the boundary edges in two dimensions or surfaces in three dimensions are robust against external

interferences[11,21,22], shown in Figure *5* [23]. Unlike conventional symmetry-breaking, topological phases are distinguished by topological invariants of discrete quantities computed from the electronic band structure. These invariants cannot change without closing the bulk energy gap, leading to robust boundary states. These features were theoretically discovered in the 2000s and experimentally verified in materials like HgTe quantum wells and Bi_2Se_3 [2,5]. This section synthesizes the physical framework with mathematical interpretations along with the experimental model of previously grown TIs.

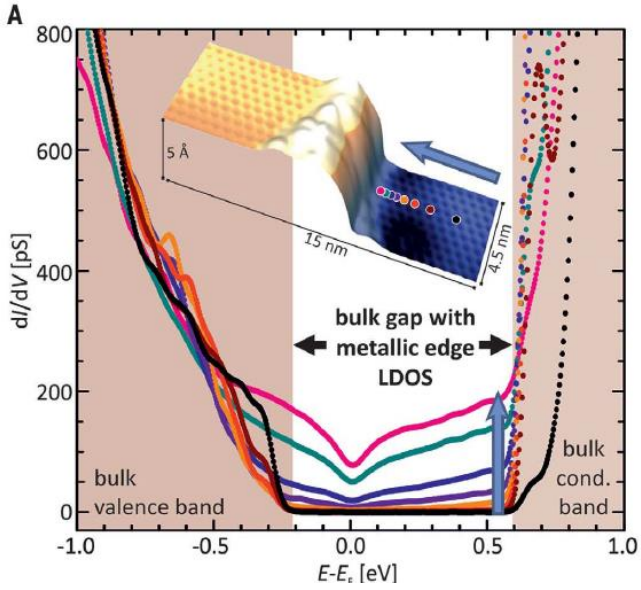

Figure 5: Differential conductivity dI/dV (reflecting the LDOS) at different distances [23].

The physics of topological insulators is governed by the interplay of symmetry, band topology, and SOC, which collectively stabilize their robust boundary states. The core is the bulk-boundary correspondence, which when is a nontrivial bulk topological invariant such as Chern number or $\mathbb{Z}_2$ index guarantees the conducting states at the material's boundaries. Chern number (n) is a 2-D system TKNN invariant, named after the first study of 2-D Quantized Hall Conductance by Thouless, Kohmoto, Nightingale, and Nijs, that defined by Berry curvature and Berry connection [14]. Berry curvature is defined by [11,24]:

$$F(k) = \nabla_k \times A(k) \tag{1}$$

where ∇_k is the gradient operator in momentum space, and $A(k)$ is the Berry connection that is defined by [11,24]:

$$A(k) = i\langle u_k|\nabla_k|u_k\rangle \tag{2}$$

where u_k is the occupied Bloch functions[25]. For systems that break TRS, the Chern number serves as the quantized invariant determining properties such as the quantized Hall conductance through the integration of Berry curvature [11,24]:

$$n = \frac{1}{2\pi}\int_{-k}^{k} F(k)d^2k\,. \tag{3}$$

$\mathbb{Z}_2$ invariant (ν) can be either 2-D or 3-D system invariant that is defined as in a reversal-symmetric system. ν is distinguished between 0 and 1 where $\nu = 0$ represents a trivial state and $\nu = 1$ represents a topological state [3,25–27]. In 2-D TIs, $\nu = 1$ and guarantees helical edge states with spin-momentum locking and n equals the number of chiral edge states that quantize the Hall conductance, and in 3-D TIs, $\nu = 1$ secures an odd number of Dirac cones on all surfaces [28]. Therefore, 2-D TIs host helical edge states with counter-propagating spins protected by TRS from the interpretation of ν and n, and 3-D TIs feature Dirac-like surface states with linear dispersion $E(k) = \pm v|k|$[11,28] and spin-momentum locking $S(k) \propto \hat{z} \times k$ [11,26].

In crystalline solids, electrons are described by a Bloch Hamiltonian $H(k)$, which defines energy bands over a toroidal manifold in momentum space called the Brillouin zone. The eigenstates u_k in the Hamiltonian describe the energy spectrum and the geometric phase information essential for topological classification in Berry connection and Berry Curvature [24,27]. The integral of the Berry curvature over the Brillouin zone leads to topological

invariants that are insensitive to continuous deformations of the Hamiltonian provided the bulk gap remains open. At low energies near band crossings, many TIs are effectively described by Dirac-like Hamiltonians [29,30]. A prominent example is the Bernevig–Hughes–Zhang (BHZ) model for two-dimensional TIs [5], expressed as:

$$H(k) = \begin{pmatrix} h(k) & 0 \\ 0 & h^*(-k) \end{pmatrix} \tag{4}$$

with $h(k) = \epsilon(k) + d(k) \cdot \sigma$, $\sigma = (\sigma_x, \sigma_y, \sigma_z)$ as the Pauli matrices, and $\epsilon(k) = C - D(k_x^2 + k_y^2)$ as the kinetic energy term where C is the energy offset that sets the baseline energy relative to the valence band maximum of the material, and D is the dispersion parameter that adjusts the parabolic dispersion [5]. The parameterization for h(k) can be summarized as: $d_x(k) = Ak_x$, $d_y(k) = -Ak_y$, and $d_z(k) = M - B(k_x^2 + k_y^2)$. A is Dirac velocity parameter that determines the slope of the Dirac cone near $k = 0$, while B is the curvature parameter that controls the quadratic correction to the mass term $d_z(k)$ to ensure the Hamiltonian remains gapped at large k [1–5,11,30]. M is referred to as the mass parameter that undergoes a sign change at the critical point, an indication of a band inversion that illustrates the transition from a trivial to a topologically nontrivial phase [16,30].

2.2.2 Physics of topological insulator

Based on the interpretation of the fundamental mathematical framework of TIs, the nontrivial topology of the bulk bands mandates the emergence of conducting states. The edge states appear as helical modes where electrons of opposite spin counter-propagate [1]. This feature implies the Quantum Spin Hall Effect (QSHE), in which the conductance is robust against nonmagnetic disorder in a 2-D TIs [15]. Section 2.3 will provide specific details of Quantum Spin Hall Insulators (QSHIs), which are based on the property of the QSHE. Bulk-Boundary Correspondence asserts that the number and nature of the boundary modes are directly

determined by the bulk topological invariants [4,8,11–15]. For example, in the quantum Hall effect, the difference in the Chern number across an interface equals the number of chiral edge modes present.

In 3-D TIs, the surface hosts a single Dirac cone with spin-momentum locking that indicates the electron's spin orientation is directly correlated with its momentum[18]. These surface states are protected by TRS and cannot be gapped out until TRS is broken [3,5,14,24–27]. TRS protects the gapless boundary modes from the interference of nonmagnetic impurities to stabilize the topological phase [1–3,5,14,24–27]. Furthermore, strong spin-orbit coupling facilitates the band inversion that represents the topological phase. The unusual electromagnetic response of 3-D TIs is expressed by a topological field theory that supplements Maxwell's equations with an additional "axion" term [4,16]:

$$S_\theta = \frac{\theta e^2}{2\pi h} \int d^3x dt E \cdot B \,, \tag{5}$$

where $\theta = \pi$ in the nontrivial phase. This term shows the topological magnetoelectric effect, wherein an applied electric field induces a magnetic response and vice versa.

Experimentally, TIs are identified via angle-resolved photoemission spectroscopy (ARPES), which allows one to directly visualize Dirac cones and the band inversion that indicates SOC. Material realizations in previous study, shown in Figure *6* [5], illustrate that 2-D HgTe/CdTe quantum wells and Bi_2Se_3 indicates the role of chemical tuning to enhance SOC and minimize bulk conductivity [18,30–34]. The plateau approaches the theoretical value $G = \frac{2e^2}{h}$ only when the edge path length is shorter than the inelastic scattering length. Trace II (blue) implies multiple spin-flip or elastic back-scattering events along the perimeter reduce the hall conductance to $\frac{0.3e^2}{h}$, and trace III (red) with enhanced SOC creates two counter-propagating spin

channels give the quantized $\frac{2e^2}{h}$ conductance for QSHE. Figure 7 illustrates effect of SOC through the two panels follow different high-symmetry directions with a slight anisotropy: the cone tips are identical, but away from Γ the branches deviate, which reflects hexagonal warping of the surface state in this lattice. Without SOC, the bulk valence band at Γ will have lower binding energy compared to the bulk conduction band that implies a normal ordering.

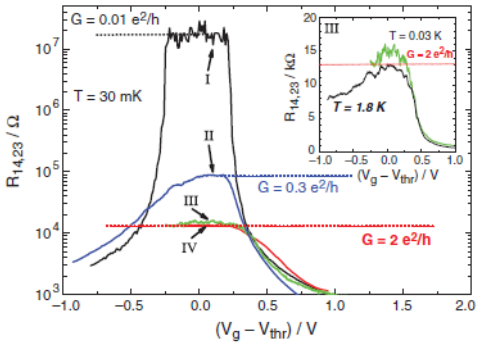

Figure 6: The longitudinal four terminal resistance, R14,23, of various normal (d = 5.5 nm) (I) and inverted (d = 7.3 nm) (II, III, and IV) QW structures as a function of the gate voltage measured for B = 0 T at T = 30 mK. The device sizes are (20.0 × 13.3) mm^2 for devices I and II, (1.0 × 1.0) mm^2 for device III, and (1.0 × 0.5) mm^2 for device IV [5].

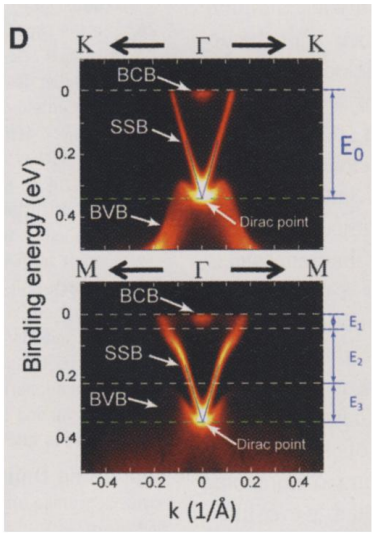

Figure 7: ARPES measurements of band dispersions along K-Γ-K (top) and M-Γ-M (bottom) directions. The broad conduction and valence bulk band (BCB and BVB) the sharp V-shape dispersion is from the surface state band. The apex of the V-shape dispersion is the Dirac point [33].

2.3 Quantum Spin Hall Insulator

The Quantum Hall effect (QHE) is a topological state of matter in two-dimensional electron systems that are subjected to strong magnetic fields [35,36], shown in Figure *8*, where the transverse charge conductance becomes quantized in integer multiples of $\frac{e^2}{h}$ [2–4,11]. This quantization is in the formation of Landau levels and the emergence of dissipation-less chiral edge states through the protection of breaking of TRS due to the external magnetic field [35]. However, the necessity of TRS-breaking fields limits the QHE's applicability to systems where spin-dependent phenomena are suppressed.

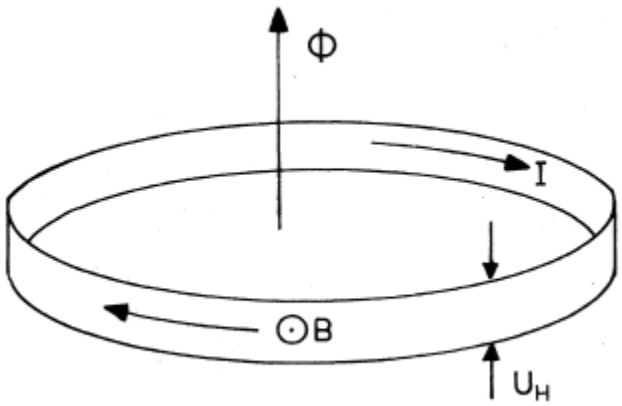

Figure 8: Model of a two-dimensional metallic loop used for the derivation of the quantized Hall resistance [35].

In order to overcome the limit of QHE, preserving TRS while exhibiting a quantized spin Hall conductance is necessary, and QSHE is a perfect phenomenon that has the corresponding properties. Unlike the QHE, the QSHE is based on SOC in materials with strong relativistic interactions to effectively generate opposite "orbital magnetic fields" for electrons with opposite spins [1–4]. This mechanism leads to the formation of spin-polarized Landau levels in the absence of an external magnetic field. As a result, a QSHI phase is characterized by a bulk insulating gap and gapless helical edge states, where electrons with opposite spins propagate in

opposite directions[5,15]. These edge states are topologically protected from non-magnetic impurities to ensure dissipation-less spin currents.

The intrinsic spin Hall conductance in QSHIs is quantized in units of $\frac{2e^2}{h}$ to reflect the spin-momentum locking of the edge modes [15]. While the net charge conductance vanishes due to the cancellation of spin-up and spin-down contributions, the spin conductance remains finite and quantized, implying a robust platform for spintronic applications [5,26]. Experimental realizations of QSHIs have been proposed in zinc-blende semiconductors such as GaAs and InSb [37–39]. By engineering strain configurations or growth-direction asymmetries, these materials can host the requisite spin-orbit-coupled band structures to stabilize the QSHE in order to grow a functional QSHI [8].

This section describes the foundation for understanding the QSHI by introducing its physical origins and key characteristics of QSHE. Subsequent sections will delve into the mathematical framework governing SOC Hamiltonians, the key mechanisms of QSHI behavior, and the emergent properties of these topological states.

2.3.1 Quantum Spin Hall Effect

The QSHE emerges in systems with strong SOC, which introduces an effective velocity-dependent force analogous to a magnetic field [15]. For zinc-blende semiconductors under strain, the conduction band Hamiltonian combines kinetic energy, strain-induced terms, and SOC [4,15]. The SOC term derives from the interplay between strain gradients and momentum, mimicking an effective vector potential . The Hamiltonian is expressed as [15]:

$$H = \frac{p^2}{2m} + Btr(\epsilon) + \frac{C_3}{2\hbar}\sum_{i,j,k}\epsilon_{jk}\left(p_j\sigma_k - p_k\sigma_j\right), \tag{6}$$

where C_3 is the material-dependent SOC strength, ϵ_{jk} is the strain tensor, and σ_k are Pauli matrices that are the same as equation (4). For a strain configuration with gradients g can is expressed as: $\epsilon_{xz} = gy$ and $\epsilon_{yz} = gx$, the SOC term reduces to [15]:

$$H_{SO} = \frac{C_3 g}{2\hbar}\left(yp_x - xp_y\right)\sigma_z, \tag{7}$$

This term acts as an orbital magnetic field $B_{eff} \propto \sigma_z g$, which is opposite for spin-up ($\sigma_z = +1$) and spin-down ($\sigma_z = -1$) electrons [15].

In the presence of a parabolic confining potential $D(x^2 + y^2)$, the total Hamiltonian becomes [15]:

$$H = \frac{p_x^2 + p_y^2}{2m} + \frac{C_3 g}{2\hbar}\left(yp_x - xp_y\right) + D(x^2 + y^2). \tag{8}$$

Under a coordinate transformation $x \to (2mD)^{-\frac{1}{4}}x,\ y \to (2mD)^{-\frac{1}{4}}y$, and defining $R = \frac{C_3 g}{2\hbar}\sqrt{\frac{\hbar}{2mD}}$, the Hamiltonian simplifies at $R = 2$ to [15]:

$$H = \frac{1}{2m}\left(\vec{p} - e\overrightarrow{A_{eff}}\sigma_z\right)^2, \tag{9}$$

where $\overrightarrow{A_{eff}} = \frac{mC_3 g}{2\hbar e}(y, -x, 0)$. This expression resembles Landau levels for each spin, with opposite effective fields. Diagonalizing the Hamiltonian using holomorphic ladder operators $a, a^\dagger$ and antiholomorphic ladder operators $b, b^\dagger$ yields quantized energy levels [15]:

$$E_{\uparrow,\downarrow} = \sqrt{\frac{D}{2m}}\left[\left(1 \mp \frac{R}{2}\right)aa^\dagger + \left(1 \pm \frac{R}{2}\right)bb^\dagger + 1\right]. \tag{10}$$

At $R = 2$, the lowest Landau level for spin-up is holomorphic, which is about $z^m e^{-\frac{|z|^2}{2}}$, and spin down is antiholomorphic, which is about $(z^*)^m e^{-\frac{|z|^2}{2}}$ [15]. Therefore, it reflects the opposite chirality. The spin-up and spin-down electrons inhabit counter-propagating edge states. The edge

modes are described by a helical Luttinger liquid, with conductance governed by the Landauer-Büttiker formula [40,41]:

$$I_i = \frac{e^2}{h}\sum_j \left(T_{ji}V_j - T_{ij}V_i\right) \tag{11}$$

where V_{ij} is the voltage that is determined by the chemical potential μ_{ij} by $V_{ij} = \frac{\mu_{ij}}{e}$, and T_{ij} is the transmission matrix that interpolates the number of channels connecting probe i to probe j.

Each spin species contributes a quantized charge conductance $\pm\frac{e^2}{h}$. However, the net charge conductance cancels ($\sigma_{xy} = 0$) while the spin Hall conductance remains quantized [15]: This quantization leads to the spin-momentum locking of the edge states, with spin up electrons moving clockwise and spin down electrons moving counterclockwise. The QSHI phase is captured by a double Chern-Simons theory [15]:

$$S = \frac{\nu}{4\pi}\int \epsilon^{\mu\nu\rho}\left(a_\mu \partial_\nu a_\rho - c_\mu \partial_\nu c_\rho\right), \tag{12}$$

where a_μ and c_μ are the gauge fields with opposite direction [8,12–15]. This theory avoids chiral anomalies and underpins fractional QSHE states when interactions induce Laughlin-like wavefunctions[2,15]:

$$\psi(z_i, w_i) = \prod_{i<j}(z_i - z_j)\hat{}m \prod_{k<l}(w_k^* - w_l^*)^m \times \prod_{r,s}(z_r - w_s^*)^n \, e^{\frac{-1}{2}(\sum_i z_i z_i^* + \sum_k w_k w_k^*)}, \tag{13}$$

where z_i is the spin up coordinate and w_i is the spin down coordinate.

In conclusion, the QSHE is managed by a spin-resolved Landau level structure induced by strain-mediated SOC that leads to quantized spin conductance and TRS-protected edge states. This approach explains topological field theory in relation to condensed matter physics that provides a theoretical framework for engineering quantum phases and spintronic applications like QSHIs.

2.3.2 Properties of Quantum Spin Hall Insulators

QSHIs represent a distinct class of 2-D topological materials characterized by a bulk insulating gap and gapless, spin-polarized edge states from the characteristics of QSHE. These properties emerge from SOC and TRS, which distinguishes QSHIs from conventional insulators and other quantum Hall systems. The bulk of a QSHI exhibits an insulating gap induced by SOC with the electronic bands acquiring a nontrivial topology quantified by the topological invariant $\mathbb{Z}_2$ [3,4,15,16]. Unlike trivial insulators, the $\mathbb{Z}_2 = 1$ classification ensures the existence of robust edge states [42–44]. The gap comes from relativistic interactions in materials such as zinc-blende semiconductors through strain gradients or structural asymmetries that generate an effective orbital magnetic field for each spin species [15,16]. This field splits the bulk bands into spin-resolved Landau levels breaking TRS. The key for QSHIs is shown in Figure *9*, which is the presence of counter-propagating and spin-polarized edge states [15,16]. Electrons with spin-up and spin-down exhibit a phenomenon called spin-momentum locking by propagating in opposite directions along the sample boundary.

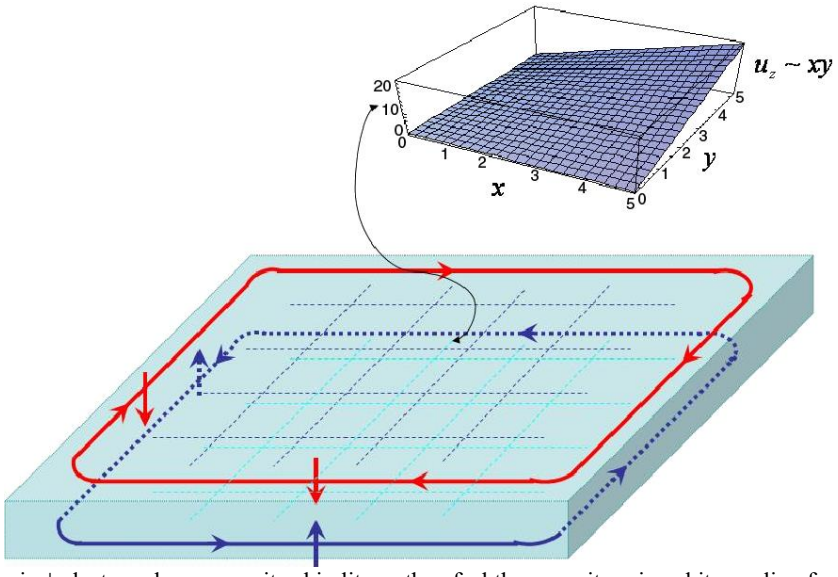

Figure 9: Spin ↑ and spin ↓ electrons have opposite chirality as they feel the opposite spin-orbit coupling force. Total charge conductance vanishes but spin conductance is quantized. The inset shows the lattice displacement leading to the strain configuration [15].

These helical edge states are protected by TRS, so any backscattering process between opposite spins would require breaking TRS and so they are immune from non-magnetic impurities [3,25]. The edge modes form a helical Luttinger liquid, enabling dissipation-less spin currents [44].

2.3.3 Applications of Quantum Spin Hall Insulators

Based on the unique properties from the physical framework of QSHE, QSHIs have emerged as a powerful platform for next-generation technologies spanning spintronics, quantum computing, sensing, and energy-efficient electronics [7,44–51]. The SOC edge states of QSHIs are ideal for generating and controlling pure spin currents, which is critical for spintronics [44]. Unlike conventional charge-based electronics, spintronic devices exploit electron spin to transmit additional information and provide lower power consumption with enhanced efficiency. QSHI-based spin transistors could modulate spin currents via gate voltages to enable non-volatile memory and logic devices [46]. The dissipationless nature of edge states minimizes energy loss during operation. The inherent spin polarization of edge states allows QSHIs to act as efficient spin filters that inject spin-polarized currents into adjacent materials without external magnetic fields [4,8,11–16,46].

Furthermore, the robustness of QSHI edge states against decoherence positions them as candidates for fault-tolerant quantum computing. Proximity coupling QSHIs with superconductors could induce topological superconductivity in the edge states, which are predicted to host Majorana zero modes as shown in Figure *10* [47]. These quasiparticles are pivotal for topological qubits that are intrinsically protected from local noise. The 1-D helical edge states provide a natural platform for composing Majorana fermions for quantum computing. Experiments with HgTe/CdTe heterostructures have demonstrated preliminary evidence of such hybrid systems [5,30].

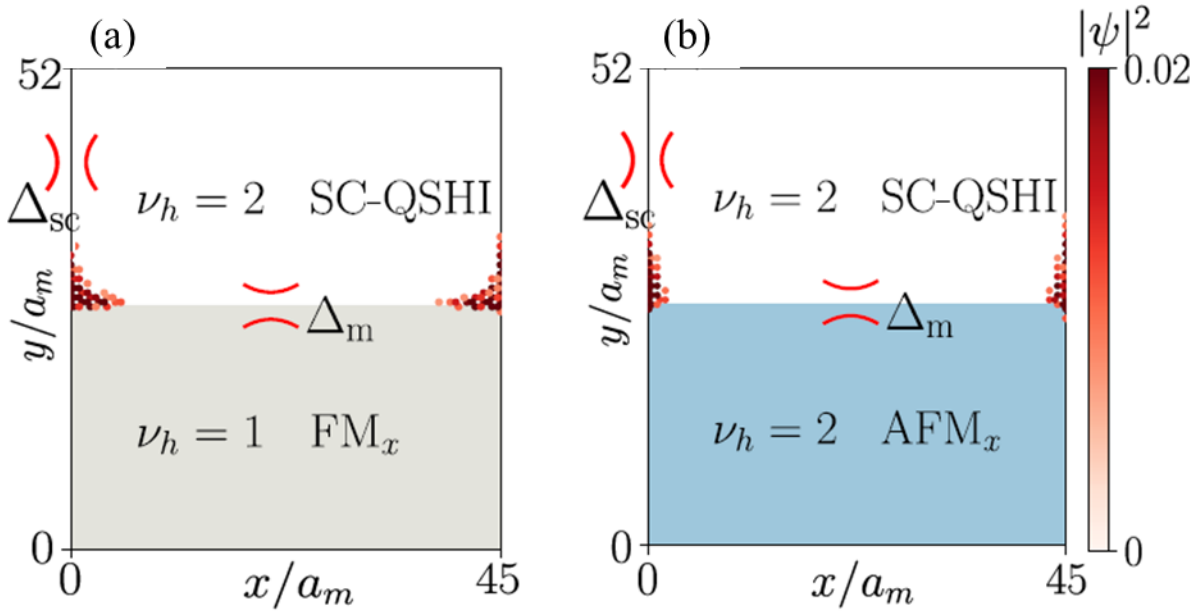

Figure 10: (a,b) Spatial distribution of two Majorana zero modes at the boundaries in SOC-QSHI/AFM$_x$ and SC-QSHI/FM$_x$ junctions [47].

Ultra-Sensitive sensing platforms could also benefit from QSHIs. Strain gradients modulate the effective SOC in QSHIs to manipulate edge conductance [4,15]. This could allow detection of nanoscale mechanical deformations for structural health monitoring [7,48–50]. Proximity-induced exchange coupling between edge states and magnetic materials could be used to construct ultrasensitive magnetometers with sub-pico Tesla resolution[48]. The Seebeck effect in helical edge states generates large spin-dependent thermopower, which could be useful for waste heat recovery in microelectronics [7,50,51].

Quantum Spin Hall Insulators have significant potential in materials science by connecting condensed matter physics with cutting-edge technology. The properties of dissipation-less spin currents, topological robustness, and sensitivity to external stimuli have provided them with the powerful ability to serve as the platform for future spintronic, quantum computing, and sensing applications. Overcoming material and integration challenges will unleash their full potential, which is the motivation for this study. In the remaining chapters we

will explore a new material system to reveal the potential of QSHIs.

3 Quantum Well (QW) Structures

As we explained in Chapter 2, TIs represent a novel class of materials that exhibit insulating behavior within their bulk, while supporting robust conducting states along their boundaries. QSHIs are a distinct subset of 2-D topological insulators, characterized by the QSHE through helical edge states, which are pairs of counter-propagating channels with opposite spin polarizations, that enable dissipationless spin transport along the edges of the material. In order to accomplish this effect, a specific nanostructure like a quantum well (QW) is required. QW consist of a thin semiconductor heterostructures that provide a platform for engineering QSHIs [52–57]. By carefully engineering the layer composition and thickness, these structures allow precise tuning of the electronic band structure to achieve the band inversion that is necessary for the QSHE [8,48]. Prior studies have shown that InAs/GaSb and HgTe/CdTe quantum wells systems are capable of achieving this task [5,7,8,30,38,39]. The earliest experimental confirmation of the QSHE was shown in inverted HgTe/CdTe quantum wells, where the band structure's unique topology enabled the observation of quantized edge conductance independent of sample geometry. This breakthrough indicates the role of band inversion that is achieved by tuning QW thickness to stabilize the topological phase. Recent studies expanded this paradigm to other heterostructures, such as InAs/GaSb [7] and strained InAs/InGaSb [8] composite QWs. They are characterized by a unique band structure configuration where the conduction band minimum of one material lies below the valence band maximum of the adjacent material. This arrangement causes electrons and holes to be separated, which means electrons confined in the conduction band of one layer, and holes confined in the valence band of the other layer [9]. In this configuration, the electron and hole wavefunctions overlap at the interface between the two layers, and it leads to hybridization between the electron-like subband in the conduction-band

material and the heavy-hole-like in the valence-band material. This hybridization opens a finite energy gap, known as the hybridization gap [8]. Moreover, large SOC inherent to heavy-element materials enhances the band overlapping. SOC couples the spin degree of freedom of electrons and holes to their orbital motion [58] to lift degeneracies for reshaping band dispersions. In these heavy-element systems like InAs/GaSb, the strong SOC creates the band inversion to generate topological protected phases. These systems exhibit enhanced tunability because strain engineering and layer thickness optimization amplify the bulk energy gap to improve thermal stability and edge-state robustness. These systems exhibit enhanced tunability because strain engineering and layer thickness optimization significantly amplify the bulk energy gap to improve thermal stability and edge-state robustness.

The tunability of quantum well structures, facilitated by techniques such as molecular beam epitaxy and the application of external electric fields, offers a powerful means to investigate and manipulate topological phases. This chapter will explore the fundamental principles that describe QSHIs in quantum well systems. We will break down the physical framework of QWs by explaining their quantum mechanical properties and solid-state properties. Then, we will introduce the structure of our simulation model along with the comparison of previous studies.

3.1 Definition of QW

QWs are semiconductor heterostructures consisting of a thin layer of a narrow-bandgap semiconductor sandwiched between wider-bandgap semiconductor barriers [52]. A QW's physical construction exhibits quantization of carrier energy states in the dimension perpendicular to the layers that is able to modify their electronic and optical properties compared to bulk materials [52–57]. The confinement of electrons and holes in QW structures are

described by quantum mechanical phenomenon of particles trapped within a one-dimensional potential well, which is also known as particle in the box [52,59].

Carrier confinement in a quantum well results in quantized energy states, which are described by solutions to the Schrödinger equation under finite potential barrier conditions [60]. For an ideal rectangular quantum well, the discrete energy levels (E_n) of confined particles with effective mass (m^*) in a well of finite depth (V) and width (L) [57,60]. These states have either an even or odd parity to exhibit quantization along the growth axis (z-direction) while the motion in the other two dimensions remains unquantized.

Quantum states in thin GaAs QWs confined by AlGaAs barriers have been experimentally observed through optical spectroscopy, shown in Figure *11* [57]. The results indicate clear excitonic transitions attributed to electron and hole states within the QWs. In addition, the GaAs/ AlGaAs structures established well depths of 0.22 eV for electrons and 0.03 eV for holes that lead to a series of quantized states within wells by the layer thickness of 80Å, shown in Figure *12* [55]. The presence of these discrete quantum states is obtained experimentally through optical absorption and emission measurements, where excitonic transitions appear as spectral features [55–57,59].

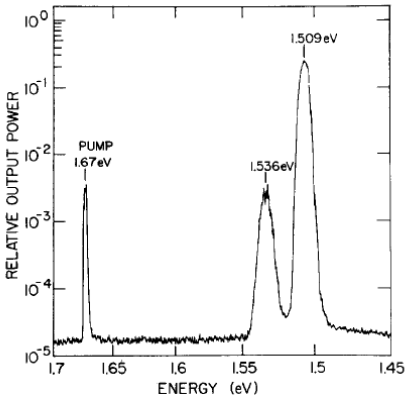

Figure 11: Emission spectrum from the (110) cleaved end face for a pump intensity 50% above the multilayer threshold. Shown in order of increasing energy are the oscillation from the buffer layer at 1. 509 eV, multilayer emission at 1. 536 eV, and scattered pump radiation at 1. 67 eV [57].

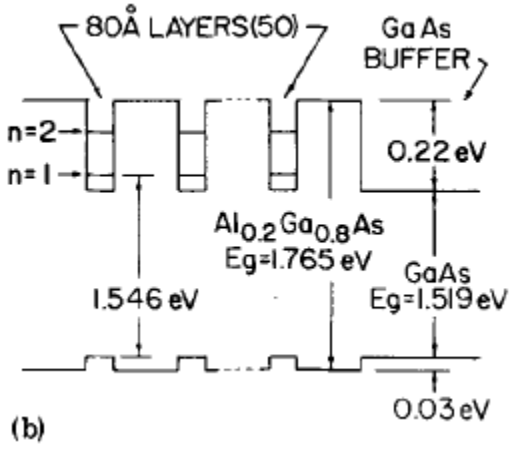

Figure 12: Band structure of SO-A.-thick GaAs layers separated by 240 Å. $Al_{0.2}Ga_{0.8}As$ layers. There are two one-dimensional bound electron states labeled n=l and 2 [55].

The tunability of quantum wells through adjustments of layer thickness and composition is crucial in practical material research for TIs [8,13,14]. The distinct quantum confined states allow precise engineering of electronic band structures, which makes QWs particularly effective in exploring and achieving the band inversion necessary for QSHE [1,8,13–15] Therefore, heterostructure quantum wells have great potential for the engineering and researching of QSHIs materials as a platform for investigating fundamental quantum phenomena for possible improvement.

3.2 Physics of QW to enable topological properties

QWs as semiconductor heterostructures are able confines electrons and holes in one spatial dimension that results in a 2-D electron gas (2DEG) where the motion is perpendicular to the layers that is quantized into discrete energy sub-bands while carriers remain free to move in the plane of the layers. This unique quantum mechanical framework reveals the ability of QWs to achieve topological properties of QSHIs.

The significance of QWs in enabling topological properties comes from their capacity to create a 2DEG, which is a prerequisite for observing effects such as the QHE and the QSHE. The

QHE appears when a high mobility 2DEG is subjected to a strong magnetic field at low temperature, which leads to the quantization of the Hall resistance in units of $\frac{h}{e^2}$ [2]. This quantization, as we explained in Chapter 2, is from the formation of discrete Landau levels that describes the topological phenomenon where the conductance is determined by fundamental constants and remains insensitive to non-magnetic interference. Similarly, QSHIs can emerge in QW systems through band inversion, a reversal of the usual conduction and valence band ordering that leads to the appearance of helical edge states [6,8,14–16,37,50,61,62]. These states enable dissipation-less spin transport, which is an important parameter of QSHIs.

The physics that enables topological properties is based quantum mechanical confinement within QWs that are described by the particle in a box model. The discrete energy sub-bands from the confinement can be affected by tuning parameters such as layer thickness, material composition, or external fields. For example, MBE allows for the specific design of QW structures, which has been demonstrated in a previous study of of InAs/GaSb multilayers [7]. The quantum size effect in QWs shows that when the QW is wider, the additional confinement energy is lower [7,8]. This causes the quantized energy levels move closer to the bulk band edge. This controls the relative positions of the electron and hole sub-bands. Therefore, tuning the QW widths is able to adjust band inversion to manipulate the system's topological properties and the formation of the excitonic insulator gap. When combining with external magnetic fields, the 2DEG in QWs implement Landau quantization that further discrete the energy spectrum to set up for topological phase transitions. The HgTe/CdTe quantum wells study reveals how this tunability can induce band inversion [5,61].

Furthermore, the crystal orientation and lattice properties of semiconductor heterostructures can significantly impact their electronic and optical characteristics, particularly

through strain engineering. Strain induced by lattice mismatch in heteroepitaxial layers modifies band alignments, which alters the electronic band structure and induce topological effects[6,30,61,62]. A previous study showed that biaxial compressive strain in InGaSb layers grown on GaSb substrates enhances the band inversion to increase the hybridization gap that significantly improve the tunability of electronic properties, thermal stability, and edge-state robustness in InAs/InGaSb quantum wells [8]. The connection between the crystallographic orientation, lattice mismatch-induced strain, and the resultant surface morphology influences the material's electronic and optical properties [6,61]. As result, the targeted manipulation of topological phases is enabled.

In this section, we will explore the fundamental mathematical and physical framework that allows QWs to support topological properties. We will examine how quantum confinement leads to the formation of a 2DEG and how this system can be manipulated to exhibit topological phases to create the QSHE in section 3.2.1. While the quantum mechanical concepts are important to form QSHI, the solid-state physical properties such as crystal orientation and lattice properties that support the quantum mechanical concept will also be explored 3.2.2.

3.2.1 Quantum Mechanical Properties of QW

To mathematically understand the quantized energy states in a QW, we start with the fundamental principles of quantum mechanics, specifically Schrödinger's wave mechanics. The fundamental quantum mechanical description of particles in a QW can be described as the model of particle in a box, which can be represent by the Schrödinger equation [60,63]:

$$-\frac{\hbar^2}{2m^*}\frac{d^2\psi(x)}{dx^2} + V(x)\psi(x) = E\psi(x) \tag{14}$$

where is $\psi(x)$ the wavefunction, $\hbar$ is the reduced Planck constant, m^* is the effective mass of the electron or hole, $V(x)$ represents the potential profile of the QW, and E is the energy eigenvalue. In a semiconductor heterostructures that is considered as a simple rectangular potential well model with a thin layer of narrow-bandgap material that is sandwiched between wide-bandgap materials, the potential can be described as [63]:

$$V(x)\begin{cases} 0, & 0 \le x \le L \\ V_0, & x \le 0, x \ge L \end{cases} \tag{15}$$

with L as the width of the well and V_0 is the finite barrier height in the barrier materials. Therefore, $V(x) = 0$ implies inside the well, and $V(x) = V_0$ implies outside the well. The solution of equation (14) depends on boundary conditions determined by the finite potential barriers where the displacement and the first order derivative of the wavefunction must be continuous across these boundaries. Based on the relationship from equation (15), $\psi(x)$ will be zero at the walls at $x = 0$ and $x = L$, then the boundary condition can be expressed as $\psi(0) = 0$ and $\psi(L) = 0$ [63]. Using the wave-like properties [60], the general solution of the wavefunction is [63]:

$$\psi(x) = Ccos(kx) + Dsin(kx), \tag{16}$$

where C and D are constants, and k is the wavenumber that defined by $k = \frac{\sqrt{2m^*E}}{\hbar}$. Applying the boundary condition on equation (16), we will get:

$$\psi(x) = \begin{cases} x = 0, & \psi(0) = C \\ x = L, & \psi(0) = Dsin(kL) \end{cases} \tag{17}$$

Moreover, D cannot be zero for setting up $\psi(L) = 0$ because it indicates the particle cannot be found. Therefore, the sine function in the wavefunction has to be eliminated by itself to achieve that. In order to achieve that, we will set kL $(with\ x = L)$ to equal the multiplication of integers and π, then k can be expressed as [60,63]:

$$k = \frac{n\pi}{L}, n = 1,2,3 \dots \dots \tag{18}$$

Furthermore, n starts on 1 because $\mathrm{n} = 0$ will result in $\sin(\mathrm{kx}) = 0$ for all values of x, similar to the case of setting $D = 0$, which is not a physically interesting solution. With equation (18), n then can be defined as quantum number that specifies the quantized state of the system. Moreover, using the relationship of $E = \frac{k^2\hbar^2}{2m}$, the energy of specific quantized state can be shown as [6,59–63]:

$$E_n = \frac{n^2\hbar^2\pi^2}{2m^*L^2} = \frac{n^2h^2}{8m^*L^2}, \tag{19}$$

where the first term of equation (19) includes π and second term of equation (19) excludes π for the original Planck's constant h.

In past studies, quantum confined states have been observed through optical spectroscopy in different multilayer structures [5,8,18,30–34,55,56]. For optical transitions, the quantum confinement modifies the exciton states and increases their binding energies. The excitonic transition energies E_{ex} and binding energies $\mathrm{E_b}$ are approximated by solving the exciton Hamiltonian:

$$H_{ex} = -\frac{\hbar^2}{2m_e^*}\nabla_e^2 - \frac{\hbar^2}{2m_h^*}\nabla_h^2 - \frac{e^2}{e\pi\varepsilon|r_e - r_h|} + V_e(r_e) + V_h(r_h), \tag{20}$$

where m_e^* and m_h^* are effective masses for electrons and holes, r_e and $\mathrm{r_h}$ are position vectors for electrons and holes, ε is the dielectric constant of the semiconductor, and V_e and V_h are electron and hole confinement potentials. These excitonic states lead to distinct optical transitions that are observed through emission and absorption spectroscopy [53–55].

The mathematical framework connecting quantum wells and topological insulators comes from the band inversion phenomenon, shown in Figure *13*, that occurs when the quantized sub-

band levels in the conduction and valence bands cross due to quantum confinement and spin-orbit coupling effects [1,6,59,61]. For QSHIs, this band inversion guarantees a topologically non-trivial phase that enables dissipation-less spin transport through edge states. The condition for band inversion in a QW system to achieve the QSHE can be summarized as [6,61]:

$$E_c - E_{HH} < 0, \tag{21}$$

where E_c is the quantized ground state in the conduction band and E_{HH} is the quantized (heavy hole) state in the valence band.

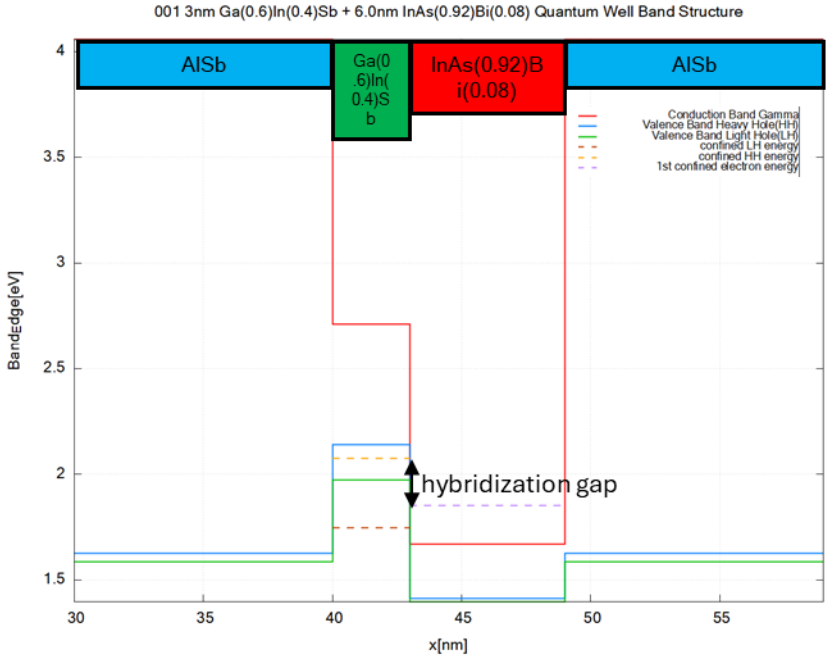

Figure 13: Energy band structure of $Ga_{0.6}In_{0.4}Sb/InAs_{0.92}Bi_{0.08}$ QWs heterostructure.

Quantum mechanics provides the fundamental mathematical and physical basis for describing quantum confinement in a particle in a box model to predict discrete energy quantization, excitonic transitions, and enabling these necessary conditions for topological phases such as QSHIs. In the next section, we will explore the solid-state properties of semiconductors that focus on determining parameters that will impact the size of hybridization gap.

3.2.2 Solid State properties: crystal orientation and lattice properties

Crystal orientation, quantum well thickness, and material composition are primary parameters that dictate the electronic and optical characteristics of QWs [5,19,30,64–69]. These structural parameters impact electronic band alignment, quantum confinement, and lattice strain. As a result, the performance of heterostructure-based devices will be significantly influenced by these solid state properties.

Crystal orientation is the first important parameter that determines the electronic and optical behavior of semiconductor heterostructures during the initial construction of the structure [19,37,66–69]. The impact of crystal orientation comes from the anisotropy of the semiconductor crystal lattice [62]. Different crystal orientations exhibit distinct atomic arrangements and therefore distinct strain distributions and piezoelectric potentials [70].

(111)-oriented substrates exhibit symmetrical strain distributions from their intrinsic C3v symmetry that construct different piezoelectric fields compared to (001)-oriented substrates, and it affect the electron-hole wavefunction overlap and exciton recombination dynamics [19,68–70]. From a recent study, In(Ga)As/GaAs quantum dots grown on a (111) substrate demonstrate intrinsic zero fine structure splitting, which indicate that the (111) In(Ga)As/GaAs quantum dots sources are suitable for entangled photon generation [68]. The (111) orientation continuously maintains higher symmetry to eliminate the lateral anisotropy and piezoelectric fields that are usually found in structures grown on (001) orientations [68], illustrated in Figure *14*, showing the result of enhancing exciton coherence and enabling ideal conditions for entangled photon pair generation. Figure 15 is the (111) GaSb atomic arrangement showing that (001) materials have a mixture of III and V atoms in their surfaces whereas (111) materials have either a III or V atom terminated surface which leads to an intrinsic electric field /polarization in the material [71].

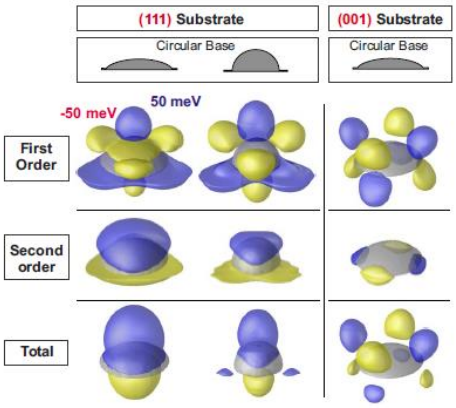

Figure 14: Comparison of the piezoelectric fields (first and second orders) for QDs grown on (111)B substrate to those grown on (001). Isosurfaces are shown for values of 50 meV (blue/gray) and −50 meV (yellow/light gray) [68].

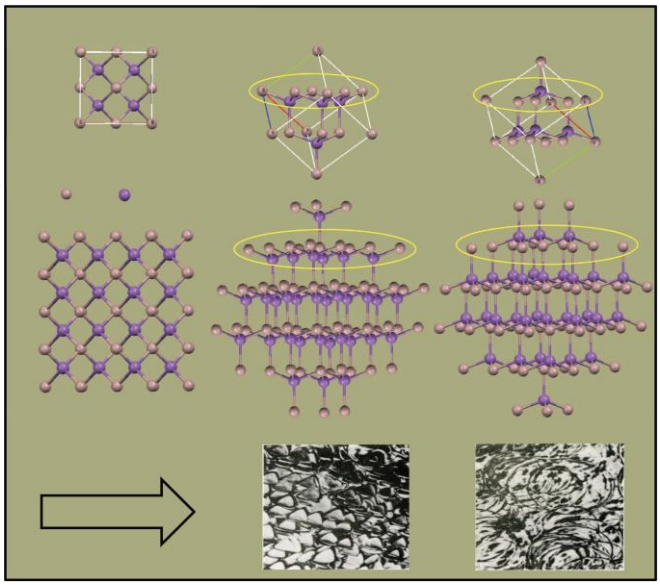

Figure 15: Atomic arrangement and etch patterns of GaSb (111)A and (111)B faces [71] .

Quantum well thickness is another crucial parameter that determines quantum confinement and the emergence of specific quantum phenomena. It influences quantum confinement that impacts the quantized energy levels within a QW [5,8,30,64,65]. Increasing the well thickness reduces energy quantization levels towards the bulk band edges, which in broken gap heterostructures can cause the topological band inversion phenomena through the relationship in equation (19). In HgTe/CdTe QWs heterostructure from previous studies, the quantum well thickness has been proved for its ability to determine a topological phase transition

[5,30]. In these systems, a critical well thickness of approximately 6.3 nm, shown in Figure 16, induces a transition from trivial insulating behavior to topological protected insulating behavior [5]. This thickness-dependent transition can be described by a Dirac-like Hamiltonian from equation (4), where the inversion of electronic bands occurs for a specific QW thickness due to the confinement-induced shift in energy levels [30].

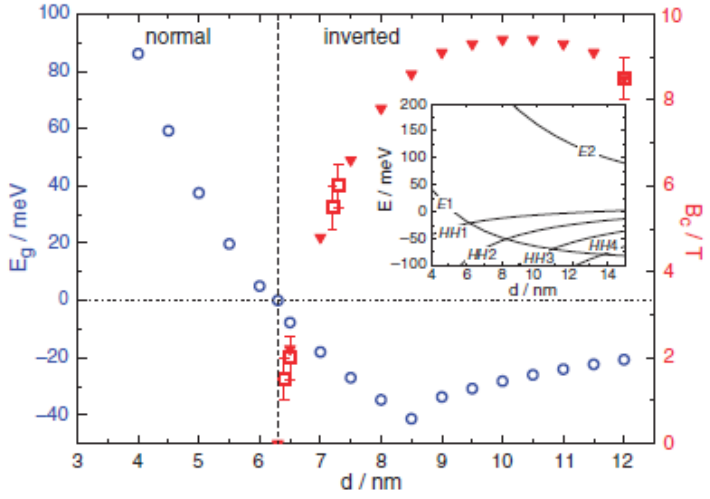

Figure 16: Crossing field, $B^{c}_{\perp}$ (red triangles), and energy gap, E_g (blue open dots), as a function of QW width d resulting from an eightband k·p calculation [5].

Furthermore, material composition dictates lattice constants, which influence the strain in the heterostructure that controls electronic band alignments. Tensile (compressive) strain is introduced when a material is grown with a smaller (larger) lattice constant than the underlying substrate. By controlling the size and direction of the strain, we can engineer changes in the band structure to enable unique optoelectronic properties. [68]. The resulting strain-induced shifts in conduction and valence bands are described using the deformation potential theory [72]:

$$\Delta E_{gap} = (a_c - a_v)\epsilon, \tag{22}$$

where a_c and a_v are the deformation potential of the conduction and valence bands respectively, , and ϵ is the biaxial strain induced due to lattice mismatch between heterostructure

layers. From a past study, GaAs quantum dots (QDs) grown on (111)-oriented substrates under tensile-strained conditions exhibit different growth dynamics compared to compressively strained quantum dots. Such tensile-strained QDs demonstrate reduced bandgaps and enhanced emission wavelengths that are tunable through adjustments in the QDs volume and growth parameters, shown in Figure 17 [19]. Moreover, Figure 18 illustrate a systematic redshift in photoluminescence emission with increased tensile-strained GaAs deposition thickness, which indicates strong quantum confinement and the direct correlation between structural parameters and emission energies [19].

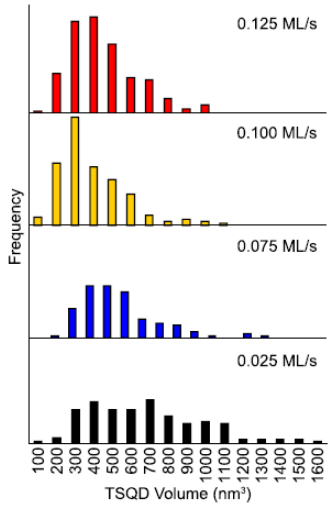

Figure 17: (Color online) Histograms of average TSQD volume as a function of increasing growth rate [19].

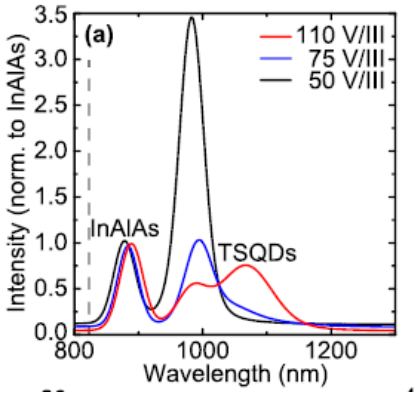

Figure 18: PL emission wavelength and intensity with increasing V/III ratio. Peak TSQD PL wavelength remains constant with increasing growth rate. Peak PL intensity decreases significantly with V/III ratio [19].

3.3 Introduction to the structure

The first functional topological heterostructure was demonstrated in HgTe/CdTe QWs [5]. The result of the study built the foundation for further explorations of materials with inverted band structures. Further research explored strain-engineered InAs/GaInSb quantum wells to show the enhancement in bulk gaps and edge state properties compared to traditional binary systems [65]. This approach illustrated the potential to manipulate electronic properties through strain, providing greater tunability for practical device implementations [65,68]. What is more, a study demonstrated evidence for a topological excitonic insulator in InAs/GaSb bilayers that suggest a phase transition into a novel state characterized by spontaneous electron-hole pairing [7].

An unrelated study investigated the optical properties of In(Ga)As/GaAs quantum dots (QDs) grown on (111) substrates that identify their potential as ideal sources for entangled photon pairs [68]. Another study further supported these findings by presenting strain-driven self-assembly of GaAs QDs on InP(111)A substrates [37]. In both cases, the threefold symmetry of the (111) substrate eliminates piezoelectric-induced anisotropy to secure negligible fine-structure splitting essential for quantum optical applications [37,68]. This symmetry-induced property suggests (111)-oriented nanostructures as beneficial for high-symmetry quantum structures [68].

Moreover, another study conducted a comparative analysis between compressive and tensile strain-induced interfacial hole localization in self-assembled quantum dots through contrasting InAs/GaAs with InAs/InSb systems [39]. Their study revealed that strain profiles critically influence carrier confinement and electronic states that support strain's importance in QSHI material optimization. In addition, a later study further support that by analyzing tensile-strained growth of GaP on various low-index GaAs surfaces to reveal that tensile strain could

effectively drive the formation of dislocation-free nanostructures to expand material possibilities beyond conventional compressively strained QDs [62]. Their findings established a robust foundation for exploring a wider range of tensile-strained QSHI materials.

What is more, a study demonstrated evidence for a topological excitonic insulator in InAs/GaSb bilayers that suggest a phase transition into a novel state characterized by spontaneous electron-hole pairing [7]. This finding revealed the connection between excitonic effects and topological properties in bilayer QW systems. Follow up on that, a recent study provided detailed insights into energy gap tuning and gate-controlled topological phase transitions in InAs/InGaSb composite quantum wells that showed the capability of electrical fields to induce reversible transitions between trivial and topological insulating phases [8]. Their work exhibits the significant potential for gate-controlled devices and practical applications of QSHIs.

Motivated by this past research we are eager to explore how the effects of strain and surface orientation could be used to enhance emergent topological properties of broken gap III-V QW systems. For our study we selected the InGaAs/GaInSb double quantum well structure. To understand the effects of substrate crystal orientation, QW layer thickness, material composition, and strain, we simulated the electronic band structure of these heterostructures to analyze and optimize the electronic structure for the construction of enhanced robust topological edge states.

3.3.1 Previous Study

In order to optimize the structure for these simulations, we investigated previous studies to determine necessary parameters that can impact the performance of QSHIs. The first study we looked at introduced strain engineering into InAs/GaInSb QWs motivated by the goal of enhancing the bulk gap and improving edge conduction properties through a ternary QW

heterostructure instead of the traditional binary system [12,65]. Anticipating larger bulk hybridization gaps and enhanced robustness of edge states, they chose strained-layer InAs/GaInSb due to its adjustable lattice mismatch [49,65]. Their results shown in Figure 19 confirmed these expectations, demonstrating a fivefold increase in the hybridization gap from ~4 meV in unstrained InAs/GaSb QWs to ~20 meV in strained InAs/$Ga_{0.68}In_{0.32}Sb$ QWs. This substantial enhancement validated strain engineering by implementing a ternary structure as a viable approach for QSHIs with tunable electronic characteristics for device applications.

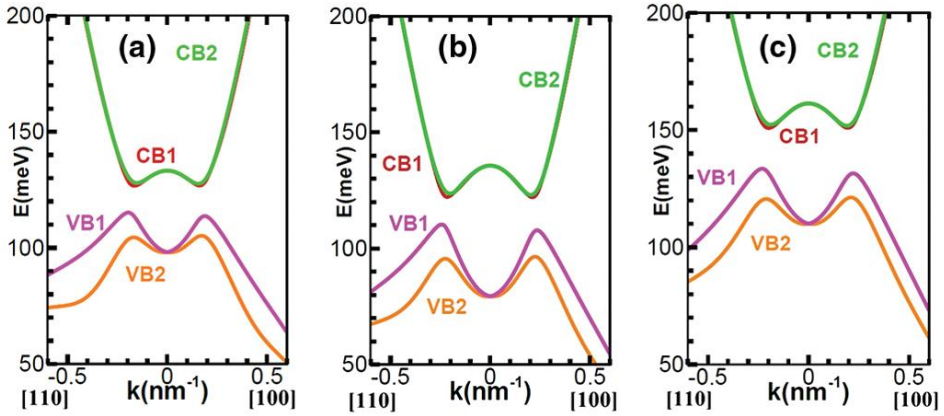

Figure 19: Calculated bulk band structure of the InAs/$Ga_{0.80}In_{0.20}Sb$ (8.7/4 nm) QWs, InAs/$Ga_{0.75}In_{0.25}Sb$ (9/4 nm) QWs, and InAs/$Ga_{0.68}In_{0.32}Sb$ (8/4 nm) QWs; CB1, VB1 and CB2, VB2 are bands of different spin component [65].

In strained QW structures, the valence band states shift depending on whether the strain is tensile or compressive [73]. Figure 20 illustrates that under tensile strain, the LH band moves above the HH band, resulting in a higher energy position for the LH state at the valence band maximum compared to the compressively strained or unstrained cases. Under compressive strain, the HH band is raised in energy that is larger than the LH band at the valence band maximum. Therefore, the LH states appear at a significantly higher energy position under tensile strain conditions than under compressive strain. This shift occurs because tensile strain elongates the lattice in-plane to cause a contraction along the growth direction [73], which raises the LH states above the HH states to change the density of states and band dispersion.

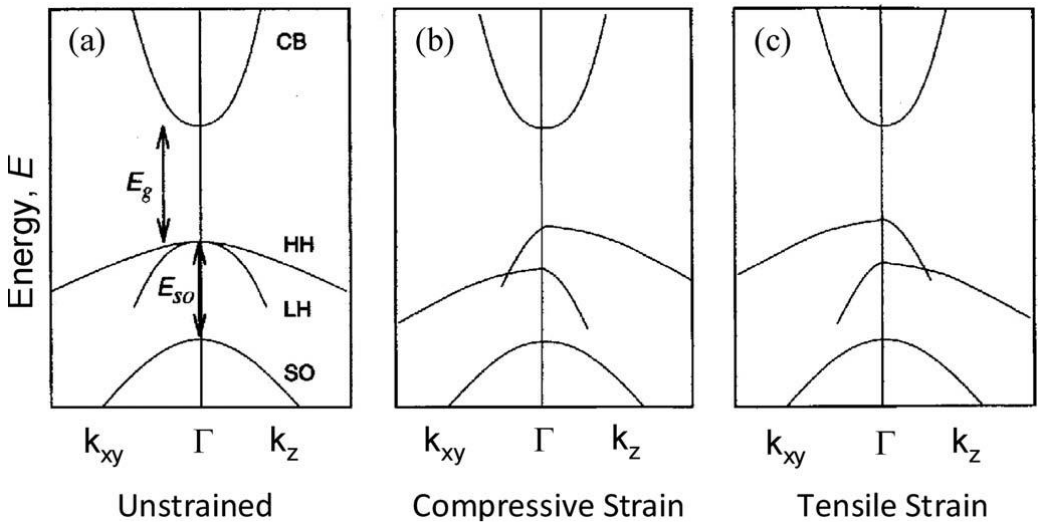

Figure 20: In a direct bandgap, bulk, unstrained structure, (a) the HH band and the LH band are degenerate at the valence band maximum at the Brillouin zone center Γ. Compressive strain (b) splits the degeneracy so that the highest band is light in the x–y plane of the layer, but heavy in the z (growth) direction. (c) This shows the converse situation when there is tensile strain in the x–y plane [73].

Furthermore, another study of InAs/GaSb bilayers were examined with the motivation to verify the existence of a topological excitonic insulator phase [7]. InAs/GaSb bilayer structure has an inverted band alignment, which construct electron-hole coexistence at low densities without external excitation [9]. This setup has the potential to spontaneously form an excitonic insulating gap at low temperatures due to electron-hole pairing. The study's result from Figure *21* of terahertz spectroscopy and electronic transport measurements confirmed their predictions by revealing a spontaneous electron-hole pairing gap of about 2 meV [7]. This finding shows the observation of a topological excitonic insulator state through electron-hole interaction's influence on topological properties.

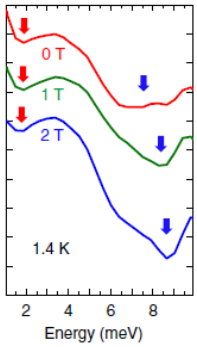

Figure 21: Spectra at different magnetic fields at 1.4K [7].

Lastly, a recent study achieved significant band-gap tuning and electrically controlled topological phase transitions in InAs/$In_xGa_{1-x}Sb$ composite QWs [8]. They were motivated from previous challenges in achieving adequate band gaps and efficient electronic manipulation in binary InAs/GaSb structures [7,39,65,70]. By adjusting the alloy composition and quantum well thickness, they anticipated a larger band gap and greater control through external electric fields. Their results achieve a of 35 meV at alloy compositions of x = 0.4 [8], shown in Figure 22, and it is relatively higher than previously reported values [65]. In addition, they successfully demonstrated gate-controlled topological transitions to show the significance of in-situ electrical control over the topological and electronic properties [8].

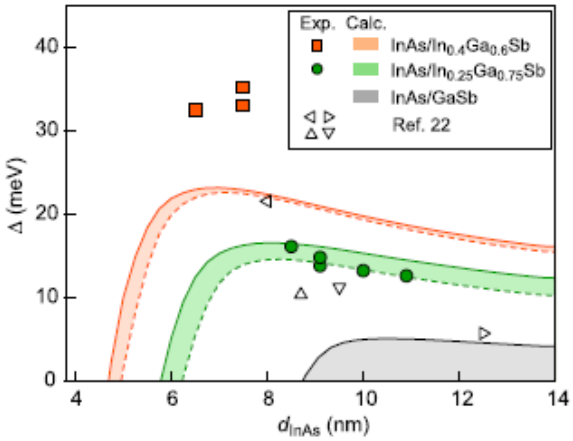

Figure 22: Measured and calculated energy gap Δ of InAs/$In_xGa_{1-x}Sb$ QWs in the inverted regime as a function of d_{InAs} [8].

Past studies of QWs heterostructures illustrated significant advancements made through targeted structural choices and strain engineering through different parameters to enhance the robustness of quantum spin hall state, which inspire the selection of QWs heterostructure of our QSHI system simulation.

3.3.2 Our structure

Inspired by the past studies [5,7,8,37,39,62,65,68], we have selected $In_xGa_{1-x}As/Ga_yIn_{1-y}Sb$ heterostructure for our QSHIs properties simulation. The simulation focused on the improvement of the hybridization gap, and influential parameters that include substrate crystal orientation, QW thickness, and material composition in heterostructure.

Semiconductor heterostructures on different substrate orientations have highlighted distinct behaviors between (001) and (111) surfaces. Inducing lattice mismatch in to the heterostructure through ternary has been shown as a potential method for enhancing the hybridization gap [65]. While manipulating the alloy composition of ternary alloy [8] exhibited its ability to tune the misfit strain within heterostructure, type of strain [73] and substrate orientation [71] has also shown their influence in the energy gap engineering. Therefore, a pre-simulation study will be conducted to validate the improvement of (111) substrate crystal orientation in enhancing hybridization gap.

From historical studies, binary system of InAs/GaSb has been well studied [7], and recent studies are also investigated in ternary system of $InAs/Ga_xIn_{1-x}Sb$. However, there are limited experimental studies in $In_xGa_{1-x}As/Ga_{1-y}In_ySb$ heterostructure. The main reason for that is the large lattice mismatch between GaAs and InSb as the ternary add-on. Ternary semiconductor materials' lattice profiles are interpolated based on their binary composition [9]. For instance, $In_xGa_{1-x}As$ will be interpolated by InAs with a lattice constant of 6.05 Å and GaAs with a lattice

constant of 5.65 Å [9]. As the composition x changes in $In_xGa_{1-x}As$, so does the lattice constant, as shown in Figure 23. Excessive strain from lattice mismatch could lead to dislocations at the substrate-film interface [10,74,75]. These defects propagate into the QW layer and act as scattering centers that disrupt electron transport and topological edge states [2,5]. Furthermore, strain relief through dislocations or cracks affect the electronic band structure. For QSHIs, this can eliminate the band inversion needed for topological protection, which render the material a trivial insulator [76], which is illustrated in Figure 24. Although the risk exists when introducing strain to the structure, the benefit of it is valuable for the improvement of the hybridization gap. Therefore, the purpose of studying material composition in this computational work will be focus on the optimizing composition for $In_xGa_{1-x}As/Ga_{1-y}In_ySb$ heterostructure to determine the best composition that bring in the best enhancement for hybridization gap without breaking the structural integrity. In addition, the thickness of QWs is also an important parameter. Theoretically, it affects the confinement of the quantized state while affecting the size of the hybridization gap [6–8,59–65].

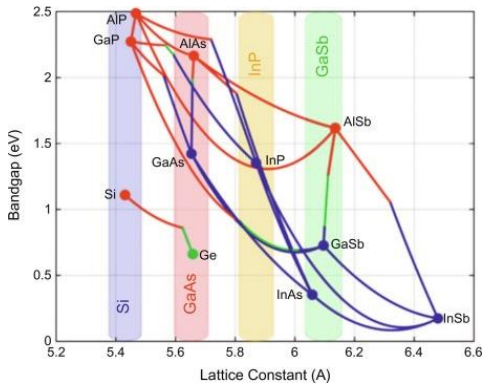

Figure 23: Graph displaying the bandgaps and lattice constants of III–V semiconductors [74].

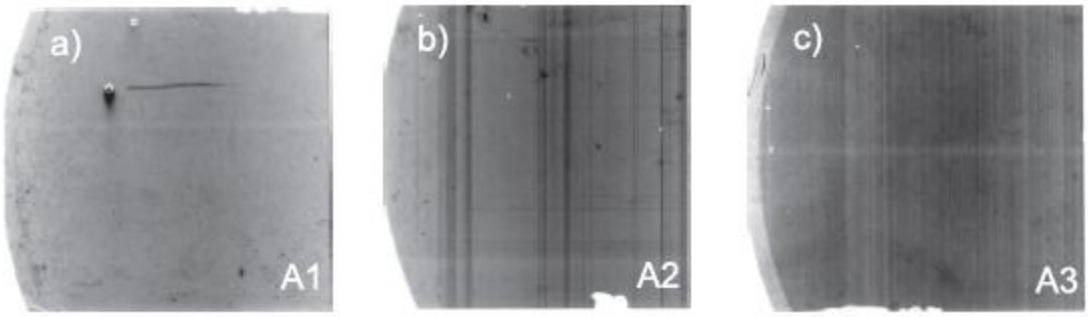

Figure 24: XRT images of GaInAs samples with different x RC characteristics. Sample A1 appears free of dislocations (a) while dislocation lines are clearly visible in samples A2 (b) and A3 (c) [76].

The final simulation structure are shown in Figure 25, with the substrate orientated on GaSb(111), a common substrate for InAs/GaSb binary and ternary heterostructure construction [75,76]. The QWs will be confined by the AlSb barrier, as it exhibits a much larger energy gap compared to $In_xGa_{1-x}As$ and $Ga_yIn_{1-y}Sb$ [9,74]. The variation in thickness from 4-10 nm is based on the data from previous studies of similar structures [7,8,37,39,62,65]. We will vary the Ga-composition x of the $In_{1-x}Ga_xAs$ QW from 0 to 1 with an increment of 0.1. Similarly, we will vary the indium-composition y of the $Ga_{1-y}In_ySb$ QW from 0 to 1 with an increment of 0.1. For strained QW structures we will calculate critical thicknesses (i.e. the maximum thickness that can be grown before the onset of plastic strain relaxation via dislocation nucleation and glide) and use these to exclude parameter sets that would not be possible to grow experimentally.. Furthermore, we will investigate whether the order in which we grow the InGaAs and GaInSb QWs has an effect on strain engineering and hence band structure. Moreover, a pre-simulation of the comparison in (001) and (111) orientated InAs/$Ga_{0.68}In_{0.32}Sb$ and InAs/$Ga_yIn_{1-y}Sb$ will be conducted to verify the impact of substrate orientation on topological states.

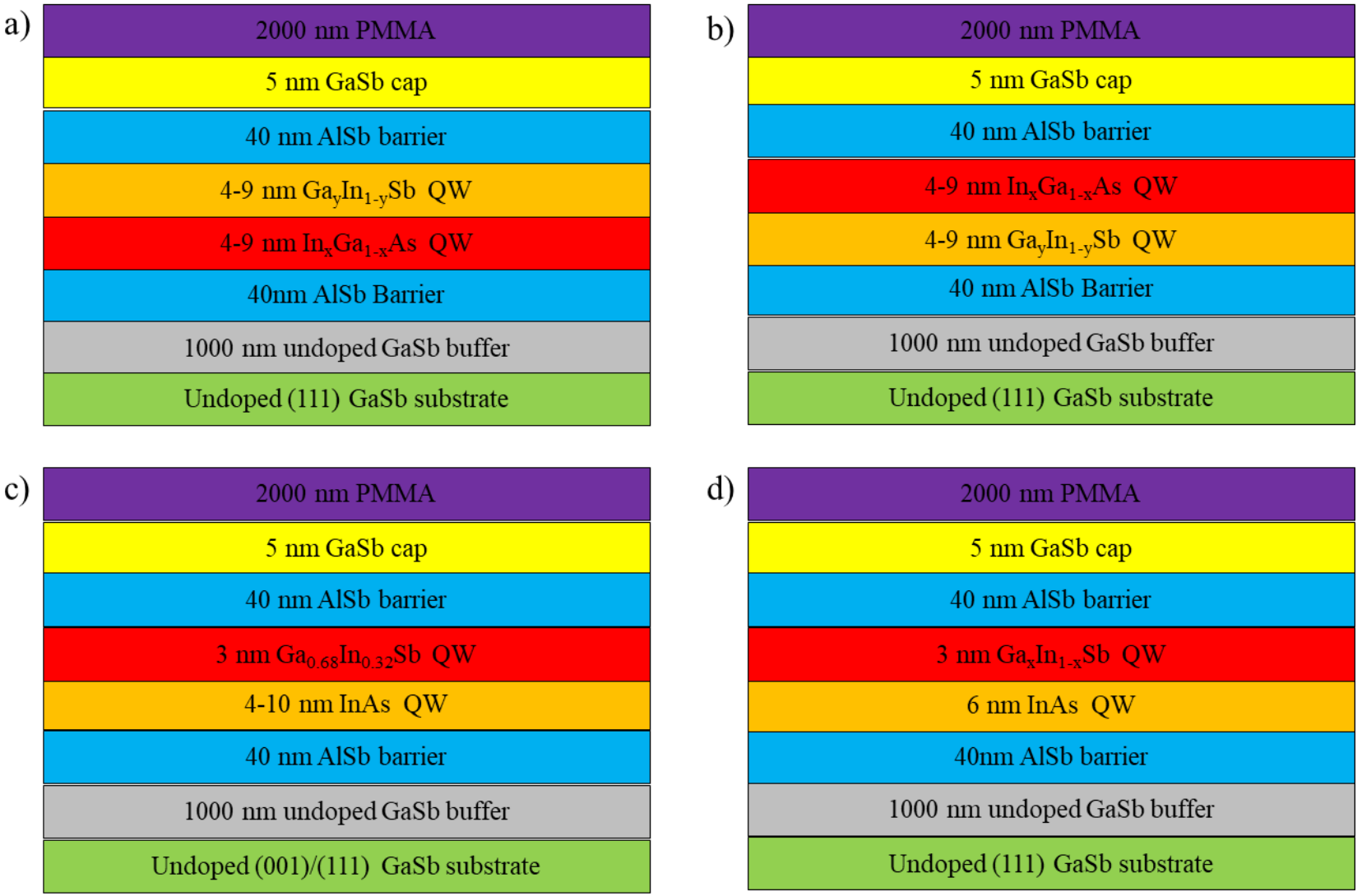

Figure 25: Simulation QWs Heterostructure a) $In_xGa_{1-x}As/Ga_yIn_{1-y}Sb$ on (111), b) $Ga_yIn_{1-y}Sb/ In_xGa_{1-x}As$ on (111), c) (001)/(111) InAs/ $Ga_{0.68}In_{0.32}Sb$ pre-simulation d) (111) InAs/ $Ga_xIn_{1-x}Sb$) pre-simulation

4 MBE Growth for $In_xGa_{1-x}As/Ga_yIn_{1-y}Sb$ Heterostructure and Critical Thickness Calculation

In this chapter we will explore molecular beam epitaxy (MBE) as a sophisticated method for the precise growth of $In_xGa_{1-x}As/Ga_yIn_{1-y}Sb$ heterostructures, which is critical for the physical realization of the TI materials we simulate. MBE is a vacuum-based deposition technique that facilitates epitaxial film growth to produce crystalline quality with high purity and integrity for advanced semiconductor devices [10,75–78], and ultrathin films with atomically abrupt interfaces that are essential for controlling electronic and topological properties within quantum wells.

This chapter begins by describing the foundational aspects of MBE, emphasizing the precise control of growth parameters including substrate temperature, beam fluxes, and deposition rates, along with their impact on the structural integrity and surface morphology of the grown heterostructures [75,77].

Then we will introduce the concept of critical thickness, which is an important factor in epitaxial growth involving lattice-mismatched heterostructures. When a thin epitaxial layer exceeds its critical thickness, strain-induced defects like misfit dislocations will appear to relieve accumulated strain [10,76]. Dislocations will negatively impact the electronic, optical, and topological characteristics of quantum wells and so to avoid them we therefore typically want to keep films below their critical thickness [79–81]. We will theoretically define the critical thickness based on thermodynamic equilibrium conditions [10], and discuss as kinetic considerations that account for practical deviations observed experimentally [76]. Experimental methodologies including high-resolution X-ray diffraction (HRXRD), and transmission electron

microscopy (TEM) are highlighted as essential tools for identifying dislocations and quantifying the extent of strain relaxation [10,75,76,78].

Lastly, the chapter indicates the importance of precise critical thickness calculation in achieving optimal epitaxial growth conditions [10,76] by minimizing defect formation to preserve the quantum and topological functionalities of our $In_xGa_{1-x}As/Ga_xIn_{1-x}Sb$ QWs heterostructures. This overview serves as a foundation for understanding the intricate interplay between epitaxial growth processes and the structural quality necessary for realizing the advanced materials we simulate.

4.1 Introduction to MBE

MBE operates by directing molecular or atomic beams of constituent elements onto a heated substrate under ultra-high vacuum conditions, where epitaxial layers form with atomically sharp interfaces and precise thickness control down to single monolayers [77]. In recent years, MBE has emerged as a primary tool for fabricating advanced TI materials [7,8,10,50,69,75–80,82]. These heterostructures require high precision in composition, thickness, and structural quality to achieve specific electronic and topological states, and MBE meets these requirements due to its capability to precisely control growth parameters including substrate temperature, growth rate, beam flux, and elemental composition.

MBE growth of TI materials that consist of Bi_2Se_3 on GaAs (111) substrates was an early application that illustrates the technique's ability to achieve coherent heteroepitaxy with minimal lattice mismatch that is necessary for preserving the topologically protected surface states [82]. Optimizing growth parameters like substrate temperature and Se-to-Bi flux ratio ensures films exhibit high crystalline quality and atomically flat terraces extending hundreds of nanometers,

which significantly reduces defects that could destroy the electronic structure inherent in topological materials [79,82].

Another advantage of MBE for TIs is its facilitation of van der Waals epitaxy, a method particularly beneficial for layered TI structures that naturally have weak interlayer bonding [69,83]. The ultra-high vacuum environment of MBE minimizes contamination and impurity incorporation for maintaining high purity and constructing the robust spin-momentum locking characteristic of TI surface states [69]. This control has been validated by the successful observation of charge-current-induced spin polarization in MBE-grown Bi_2Se_3 films [83], which reveals the direct correlation between MBE process parameters and functional TI properties. Furthermore, MBE is employed for growing lattice-matched ternary III-V compounds such as InGaAs and InAlAs on non-traditional substrate orientations such as (111) [19,62,69]. The (111) surface of the zinc-blende crystal structure of the III-V semiconductors is of interest for TIs due to their shared hexagonal symmetry which may simplify their integration [22,37,69,83].

In summary, MBE's precise control over growth parameters, epitaxial quality, and interface sharpness is necessary for fabricating topological insulator heterostructures. MBE provides control over various parameters that can impact the growth process for TIs, and which will affect the final topological properties. Therefore, a detailed investigation of growth parameters will be necessary to set up the correct simulation. We will explore these parameters along with the analysis of the growth process in the next chapter for a deeper understanding of the simulation.

4.2 MBE process

MBE process involves several steps, beginning with the preparation of substrates. Substrates for the MBE process are in the form of semiconductor wafers, and the process begins with initial

cleaning and oxide removal through thermal treatments under ultra-high vacuum conditions [69,82]. In MBE, high purity elemental sources are heated in effusion cells under ultra-high vacuum conditions and produce beams of atoms or molecules directed toward a heated substrate [77]. The beams can be rapidly turned on or off by opening or closing shutters in front of each effusion cell. The interaction of these beams with the substrate surface leads to epitaxial growth, where the deposited atoms arrange themselves in a crystalline structure matching the substrate's lattice [69]. At an atomic level, the growth rate R during MBE can be mathematically represented by the following relation [69,77]:

$$R = \frac{J \cdot \alpha}{N}, \tag{23}$$

where J is is the incident atomic flux in the unit of atoms per unit area per second, α is the sticking coefficient that represents the probability of an atom attaching to the surface upon impact, and N is the atomic density of the growing film by the unit of atoms per unit volume The substrate temperature, effusion cell temperature, and beam flux ratios are managed to achieve epitaxial growth layer-by-layer [82]. This equation indicates the importance of controlling the atomic flux and the sticking coefficient to achieve the desired growth rate and film thickness.

After atoms adhere to the substrate, they migrate across the surface through the process of surface diffusion until they encounter other adatoms to form stable nuclei [69,75,77]. The dynamics of nucleation and subsequent layer formation determine the film's structural quality [69]. The energy barriers associated with surface diffusion and nucleation dictate the growth mode, which can be categorized as Frank–van der Merwe (layer-by-layer) growth: atoms form complete monolayers before the deposition of subsequent layers for achieving atomically smooth films, Volmer–Weber (island) growth: atoms form 3-D islands due to strong adatom-adatom

interactions that exceed adatom-substrate interactions, Stranski–Krastanov (layer-plus-island) growth: initial layer-by-layer growth transitions into island formation after a few monolayers due to strain accumulation [69,77]. The choice of growth mode is influenced by factors such as substrate temperature, deposition rate, and lattice mismatch between the film and substrate [77].

The precise control in MBE is needed for synthesizing high-quality TIs. For example, the growth of the TI Bi_2Se_3 requires careful regulation of the Bi to Se flux ratio and substrate temperature to achieve stoichiometric films with minimal defects [82,83]. Studies have demonstrated that optimizing these parameters leads to atomically flat Bi_2Se_3 films with robust surface conductivity for exploring novel quantum phenomena and potential spintronic applications [82,83]. Researchers have achieved layer-by-layer growth of atomically flat Bi_2Te_3 films on Si(111) substrates[81]. Clear topological surface states were confirmed by angle-resolved photoemission spectroscopy (ARPES) shown in Figure 26 [81]. These studies highlight MBE's capability to engineer materials at the atomic level for advancements in TI-based technologies.

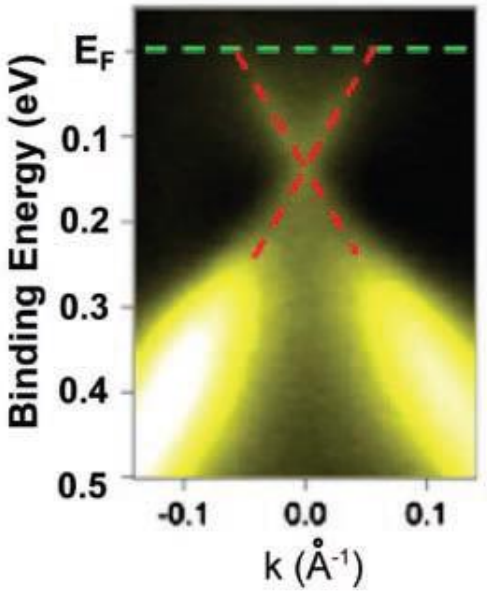

Figure 26: ARPES intensity map of the 26 QL Bi_2Se_3 film along the Γ-K direction. The green dotted line indicates the Fermi level, and the red ones indicate the topological surface states [81].

Reflection High-Energy Electron Diffraction (RHEED) is an in-situ analytical technique employed to monitor and characterize the surface structure of crystalline materials during the process of MBE [84]. In a typical RHEED setup, a high-energy electron beam of 10–30 keV is directed at a glancing angle of 1°–5° toward the surface of a crystalline sample [76–84]. Due to this shallow incidence, electrons interact with the top atomic layers and produce a diffraction pattern that is projected onto a phosphorescent screen [84]. This pattern provides information about the surface's crystallographic structure and surface morphology. The interpretation of RHEED patterns relies on the reciprocal lattice concept and the Ewald sphere construction. For surface diffraction, the reciprocal lattice is represented by rods extending perpendicular to the surface plane, reflecting the 2-D periodicity of the surface atom reconstruction [84]. The Ewald sphere, with a radius inversely proportional to the electron wavelength, intersects these rods at points that correspond to the observed diffraction features [84]. The condition for constructive interference (diffraction) is given by [84]:

$$G_{\parallel} = k_{out} - k_{in}, \tag{24}$$

where k_{out} and k_{in} are the diffracted and incident electron wave vectors, and $G_{\parallel}$ is a reciprocal lattice vector parallel to the substrate surface. During layer-by-layer growth, the intensity of specific RHEED diffraction features exhibits oscillatory behavior [84,85]. These RHEED intensity oscillations are directly related to the periodic completion of monolayers on the surface [69,84,85]. The oscillation period corresponds to the time required to deposit one atomic layer, which provides a real-time measure of the growth rate and surface smoothness [84].

RHEED has been extensively utilized in the study and fabrication of TIs to ensure high-quality film growth. Figure 27 shows that in the growth of Bi_2Te_3 thin films, RHEED patterns exhibit clear and prolonged intensity oscillations of the reflected electron beam [85]. These oscillations indicate a smooth and layer-by-layer growth mode for preserving the topological surface states inherent to TIs [85]. Figure 28 illustrates RHEED patterns of a deposited thin film GaAs, which indicates its ability to analyze thermal desorption of oxide to study the surface reconstruction as a growth parameter before the initial growth [78]. Such studies reveal the importance of RHEED in pre-growth surface analysis for securing a desired growth.

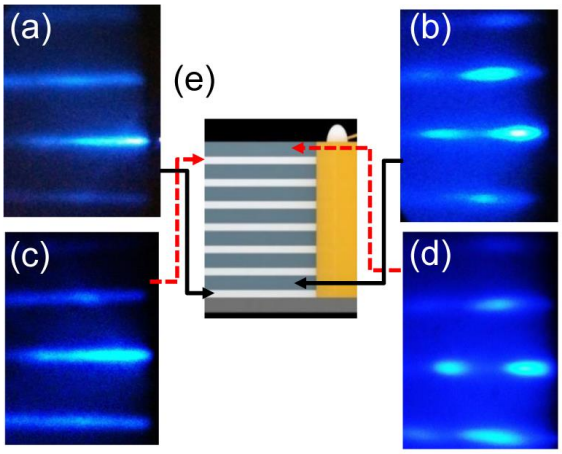

Figure 27: RHEED patterns of the sample surface: (a) and (c) are of the bottom-most and the top-most Bi_2Se_3 layers. (b) and (d) of the bottom-most and the top-most $Zn_xCd_{1-x}Se$ layers, x = 0.49. (e) A sketch linking RHEED patterns to their corresponding layers [85].

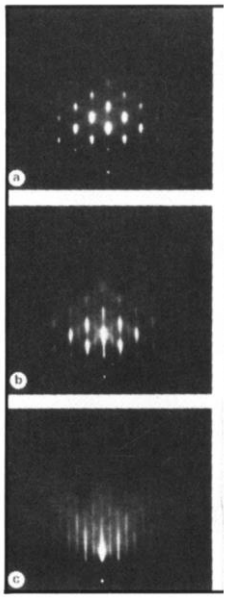

Figure 28: RHEED Pattern of (a) polished-etched (001) GaAs substrate heated in vacuum to 855 K for 5 min, (b) deposition of GaAs with an average thickness of 150 A , and (c) deposition of 1 μm GaAs [78].

4.3 Critical Thickness

MBE growth of epitaxial layers onto a substrate with a dissimilar lattice parameter result in lattice mismatch-induced strain [10,19,37,39,62]. Managing the strain to minimize or control the nucleation and glide of unwanted dislocations will determine the structural quality, electronic properties, and overall stability of semiconductor heterostructures [10,37,39]. The critical thickness is defined as the maximum thickness of a strained epitaxial film that can be grown coherently, free of dislocations and other structural defects for a given lattice mismatch [10]. Above this critical thickness threshold, the elastic strain energy becomes sufficiently high, which results in the formation of dislocations that negatively impact the heterostructure's quality and performance [85].

Critical thickness is influenced by several parameters, including lattice mismatch, elastic constants of the film and substrate materials, and growth conditions, particularly substrate

temperature [9,10,76,84]. Theoretical models have a quantitative basis for predicting critical thickness that relies on equilibrium conditions between strain energy in the epitaxial layer and the energy associated with dislocation formation [9,10]. Section 4.3.1 will provide details of the mathematical and physical framework for a theoretical prediction of critical growth thickness. Experimental determination and verification of critical thickness typically involve advanced characterization techniques like high-resolution X-ray diffraction (XRD), and transmission electron microscopy (TEM), which allow precise identification of the onset of strain relaxation through dislocation formation [76,78]. Studies of MBE-grown GaInSb/GaSb and GaInAs/GaAs heterostructures have revealed the complexities associated with accurately predicting and controlling critical thickness [76,78]. For instance, in $Ga_yIn_{1-y}Sb$ layers grown on GaSb substrates, maintaining compositional uniformity and precise control of growth conditions can delay the onset of misfit dislocations and enhance structural integrity [65]. Similarly, research on GaInAs/GaAs heterostructures emphasizes the impact of growth parameters such as substrate temperature and beam flux on critical thickness and structural properties [76]. Specific detail will be discussed in section 4.3.1.

Understanding critical thickness is important for developing advanced semiconductor devices, including the TIs based on strained QWs that are of interest in this project, where specific structural integrity is required for maintaining the integrity of quantum and electronic states. The following sections will discuss critical thickness calculations and illustrate the practical importance of maintaining critical thickness in epitaxial multilayers.

4.3.1 Importance of critical thickness

A past study has shown the practical implications of managing critical thickness [78]. When layers are grown below their calculated critical thickness, epitaxial films maintain

coherent, defect-free interfaces. This coherence guaranteed optimal electronic properties to improve carrier mobility and reduce interface scattering, which will enhance high-performance electronic and optoelectronic devices. Figure 29 illustrates strained $Ga_{1-x}In_xSb$/GaSb films grown below their critical thickness (Samples (a) and (b)) have good structural quality and electrical properties with minimal strain-induced defects [78].

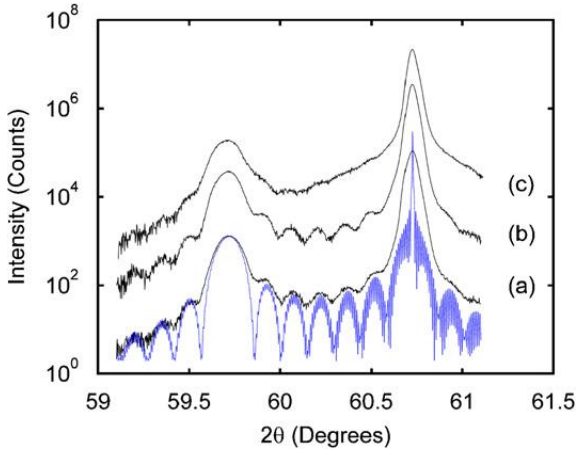

Figure 29: XRD scans from different positions on the same sample along with a simulated spectrum for position (a). GaInSb thickness of 71.5 nm and In mole fraction of 12.3% for (a), 73.4 nm and 12.3% for (b), and 74.1 nm and 12.4% for (c). [78].

In contrast, exceeding the critical thickness (Sample (c)) degrades the material properties through the formation of misfit dislocations, which serve as scattering centers and recombination sites [10,76]. This phenomenon negatively impacts the electronic and optical performance of devices. Another past study has shown that strained GaInAs/GaAs heterostructures grown beyond their critical thickness show significant increases in threading dislocations and interface roughness (see linear dislocation features in Figure 30a), resulting in reduced electron mobility, optical efficiency, and device reliability [76]. In comparison, GaInAs/GaAs samples grown below the critical thickness (Figure 30b) are free of dislocation defects (the dot and horizontal line are physical scratches). For TI heterostructures, preserving the intrinsic surface states is very important, and exceeding critical thickness can introduce defects that may disrupt topologically protected states. Therefore, keeping films below the critical thickness threshold ensures defect-

free interfaces for maintaining the integrity of quantum states for optimizing the TI's electronic and spintronic functionalities.

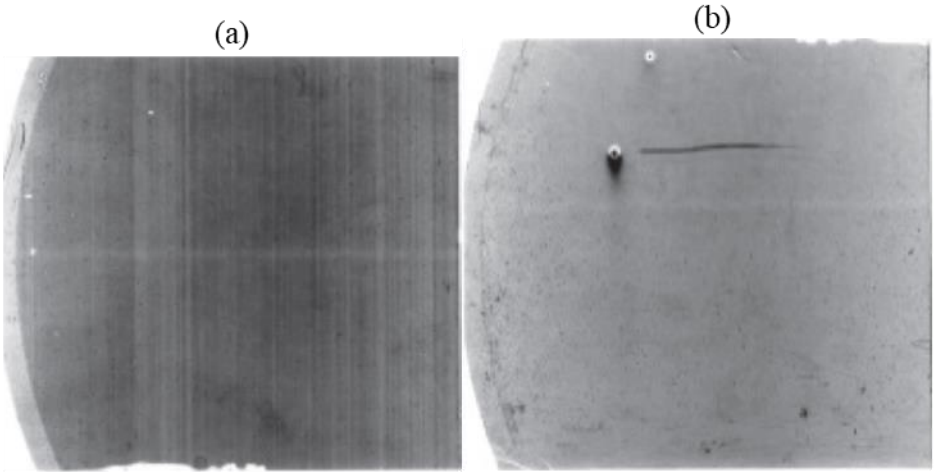

Figure 30: a) XRT of 250nm GaInAs with 46% strain relaxation. b) XRT of 250nm GaInAs with 0% strain relaxation [76].

For our study, critical thickness also will be used for directing and optimizing our experimental growths. As we explained in section 3.3.2, our simulations will explore how the band structure of coupled InGaAs and GaInSb QWs depends on the alloy composition and thickness of each QW, investigating 6 different thickness settings and 11 different composition settings for each individual ternary alloy. Therefore, more than 5000 hybridization data points will be generated. These critical thickness calculations will allow us to reduce the total number of these data points we need to consider by excluding material combination where QW thicknesses exceed the critical thickness for a given alloy composition/strain.

4.3.2 Critical thickness calculation

Critical thickness is governed by the balance between elastic strain energy and dislocation formation energy within a heterostructure [10]. The formation of misfit dislocations at the interface between the epitaxial layer and the substrate occurs when the strain energy accumulated

due to lattice mismatch exceeds the energy required to generate and propagate dislocations. This equilibrium condition can be expressed as [10]:

$$h_c = \frac{b}{2\pi f}\frac{1-\nu\cos^2\alpha}{(1+\nu)\cos\lambda}\left(ln\frac{h_c}{b}+1\right), \tag{25}$$

where h_c is the critical thickness, b is the magnitude of the Burgers vector, ν is Poisson's ratio, f is the lattice mismatch strain, α is the angle between the Burgers vector and the line direction of the dislocation, and λ is the angle between the Burgers vector and the normal interface. In the example of InGaAs ternary material, the magnitude of the Burgers vector is material lattice dependent and can be calculated by [9]:

$$b_{InGaAs} = \frac{a_{InGaAs}}{2\sqrt{h^2+k^2+l^2}}, \tag{26}$$

where h, k, l, represent the substrate crystal orientation, and a_{InGaAs} is the lattice constant of ternary alloy that lies between the two binary end-point alloys InAs and GaAs. In the case of $In_xGa_{1-x}As$, the lattice constant is calculated by [9]:

$$a_{InGaAs} = xa_{InAs} + (1-x)a_{GaAs}, \tag{27}$$

where $0 \le x \le 1$ is the material composition in the ternary alloy. Similarly, the Poisson ratio ν of a ternary alloy is also linearly interpolated between the Poisson ratios of the two binary alloys [9]:

$$\nu_{InGaAs} = x\nu_{InAs} + (1-x)\nu_{GaAs}. \tag{28}$$

The misfit strain f will be the sum of all misfit strains between layers [10]:

$$f = f_1 + f_2 + f_3 \ldots\ldots \tag{29}$$

and each individual misfit strain between two contacted layers, in the example of InGaAs and GaInSb with InGaAs at the bottom layer, will be interpolated by their lattice constants [9,10]:

$$f = \frac{(a_{GaInSb} - a_{InGaAs})}{a_{GaInSb}} \tag{30}$$

Further modifications to this classical equilibrium model account for kinetic factors since dislocation nucleation is a thermally activated process. According to the kinetic theory from [76], the critical thickness can be influenced by epitaxial growth conditions that include substrate temperature and growth rate. These kinetic considerations state the practical variations observed experimentally, which suggests that the thermodynamic model alone may inadequately predict the exact critical thickness under dynamic growth conditions, particularly in a far-from-equilibrium growth process like MBE. High-resolution XRD analysis takes advantage of the sensitivity of diffraction patterns to lattice strain and dislocations to enable precise determination of the onset of strain relaxation and subsequent dislocation generation [76,78]. TEM further complements HRXRD by providing direct visualization and characterization of dislocation structures at interfaces [76].

In conclusion, theoretical calculations incorporate detailed material parameters for accurate predictions of critical thickness [10]. These parameters are thoroughly documented in [9], which provide essential data for performing precise band structure and strain calculations. Accurately predicting and controlling critical thickness involves a comprehensive understanding of both equilibrium thermodynamics and non-equilibrium kinetics, supported by empirical observations and detailed characterization. Conducting a theoretical study before growth and characterization after test growths, ensure the successful synthesis of strained epitaxial quantum wells that are free from dislocations and hence meet the demanding structural and electronic quality requirements necessary for advanced TIs. With that in mind, our calculated critical thicknesses for various combinations of QW thickness and alloy composition (see Figure *25*) allow us to exclude regions of the band structure calculation phase space that would not be achievable experimentally, which will be shown in Chapter 7.

In summary, managing critical thickness is essential to achieve optimal structural and electronic properties in TIs based on strained QWs. Maintaining these layers below the critical thickness preserves interface coherence, reduces defect densities, and enhances device performance.

5 Methods

This chapter describes the computational methods and software tools employed in this research to model and analyze the double QWs heterostructure from Figure *25*, particularly focusing on hybridization gap optimization through QW thickness and alloy composition manipulation. To provide comprehensive and accurate predictions of the material properties and device behavior, two primary computational tools were used: NextNano [86] software for heterostructure simulations and MATLAB for critical thickness calculations.

NextNano software, developed by Dr. Stefan Birner, offers capabilities for modeling the electronic and optical properties of complex semiconductor nanostructures through solutions of the Schrödinger [60], Poisson [87], and strain [88] equations. It has become an important resource for semiconductor research due to its ability to simulate quantum mechanical behaviors and strain-induced effects in layered structures, to predict device performance under realistic operational conditions. NextNano employs methods including single-band and multi-band k·p envelope function approximations that enables precise analysis of carrier dynamics and quantum confinement effects within heterostructures [86]. Furthermore, it integrates detailed analysis of strain distributions using continuum elasticity theory, accurately capturing the effects of lattice mismatch and piezoelectric fields [86,87]. These features allow the user to predict the electronic band structure, energy levels, wavefunction localization, and optical transitions in complex semiconductor devices such as quantum cascade lasers, LEDs, and photodetectors. NextNano also provides a graphical interface along with extensive capabilities for visualizing simulation outputs, facilitating easy interpretation and analysis of complex results [86].

Complementing these simulations, MATLAB was utilized for the calculation of critical thicknesses (see Section 4.3). Accurate determination of critical thickness is crucial to avoid

strain-related defects and ensure optimal device reliability and performance. The method implemented here provides clear insights into the limits of epitaxial layer thickness to guide experimental design and improve structural quality, along with simulation result optimization.

The combination of these computational tools facilitates a deeper understanding of the physical behaviors within the studied nanostructures. In section 5.1 we will introduce the function of NextNano and how we utilize it for simulations. In section 5.2 we will explain the use of MATLAB for data interpolation and critical thickness calculations.

5.1 NextNano Software

NextNano's capability is built around single-band and multi-band k·p envelope function approximations [86] to provide flexibility and precision in simulating various semiconductor materials and heterostructures. These methods enable the simulation of band structures with realistic considerations of anisotropy, non-parabolicity, and coupling effects among different conduction and valence band states [58,89,90]. Additionally, the software calculates strain distributions using continuum elasticity theory that reflects the impact of lattice mismatch, piezoelectric, and pyroelectric fields in semiconductor devices [86–88].

The software features numerical algorithms that support self-consistent calculations of electronic states, carrier distributions, and optical properties across multiple dimensions [86]. Moreover, NextNano facilitates the simulation of realistic operational conditions by incorporating doping profiles, external electric and magnetic fields, and temperature-dependent material parameters [86]. With the built-in graphical tool in NextNano, band structures, energy states, and wavefunctions can be visualized and easily exported for using the figure generation application Gnuplot.

The following subsections will explain the internal workflow and computational processes of NextNano, covering the logic behind simulations, the generation of energy band structures, and the precise calculation of quantum states within a heterostructure.

5.1.1 Work logic of the Software

NextNano operates by solving coupled equations for semiconductor heterostructure simulations through the Poisson equation, strain equations, and Schrödinger equations using both single-band and multi-band k·p approaches [60,87,88]. Specifically, for generating band structures for broken-gap semiconductor heterostructures such as InAs/GaSb or HgTe/CdTe QWs, NextNano adopts a self-consistent computational approach, with specific band structure illustrations [86] shown in Figure 31 and Figure 32.

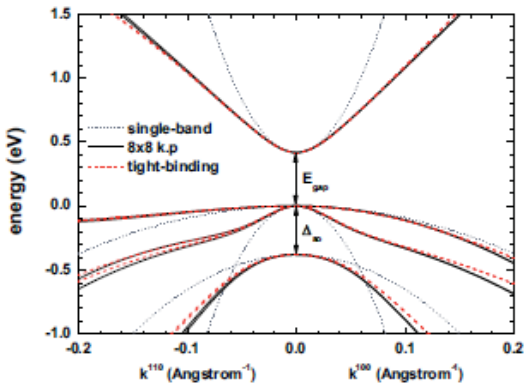

Figure 31: Energy dispersion of bulk InAs along the [110] and [100] directions in k space calculated with the parabolic model (dotted lines), the 8×8 **k·p** model (black solid lines) and with the $sp^3d^5s^*$ tight-binding parameterization (red dashed lines) [86].

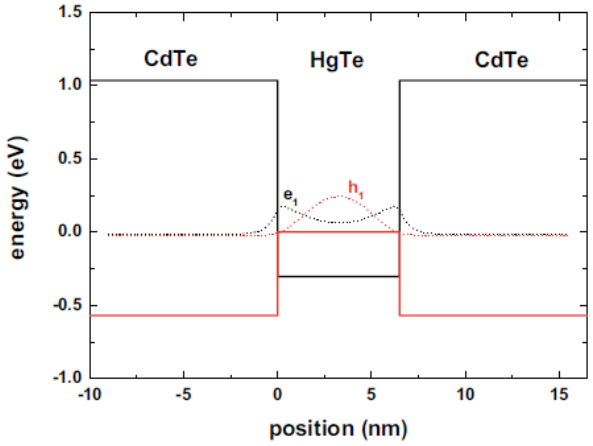

Figure 32: Probability density of the lowest electron (e_1) and highest hole (h_1) eigenstates of a 6.5 nm HgTe quantum well calculated with the k · p method [86].

NextNano begins the simulation by calculating the spatial strain distributions within the semiconductor layers based on continuum elasticity theory [91]. It identifies the effects of lattice mismatch and calculates associated strain tensor components that significantly influence the band edge profiles. NextNano then employs deformation potential theory [72] to translate these strain distributions into energy shifts in the conduction and valence band edges to enable accurate modeling of broken-gap alignments. Following the determination of strain-induced band shifts, NextNano constructs the resulting band profile by solving the Poisson equation [87] to account for built-in fields from doping and other charge distributions, including piezoelectric charges that emerge from strain-induced polarization [88]. The coupling between conduction and valence bands in broken-gap systems is addressed using a multi-band k·p envelope function approximation [92] that incorporates the interaction between conduction and valence states and accurately represents the unique band alignment of broken-gap heterostructures. Lastly, the Schrödinger equation [60,93] is solved within this self-consistently derived potential landscape to determine the quantum confined energy states and wavefunctions. These wavefunctions and

energy states are necessary for the interpolation of tunneling effects and carrier transport in broken-gap structures to validate the computation until convergence is achieved. The iterative self-consistent calculation ensures accurate and physically meaningful results for device design and analysis.

NextNano thus provides a reliable computational method from structural definition to precise electronic characterization that is ideally suited to complex systems like the broken-gap QW heterostructures used in our advanced QSHI simulations. Therefore, a detail analysis of the energy structure generation will be discussed in next section.

5.1.2 Energy band structure generation

The accurate generation of energy band structures in semiconductor heterostructures using NextNano involves solving a coupled system of equations. This comprehensive approach ensures precise simulations of complex semiconductor structures for our InGaAs/GaInSb QW heterostructures grown on GaSb(111) substrates. Firstly, the electrostatic potential profile is established through solving the Poisson equation [87]:

$$\nabla \cdot [\epsilon_0(x)\epsilon_r(x)\nabla\phi(x)] = -\rho(x), \tag{31}$$

where $\phi(x)$ represents the electrostatic potential, $\epsilon_0(x)$ is the vacuum permittivity, $\epsilon_r(x)$ is the spatially dependent dielectric constant, and $\rho(x)$ are charge densities from electrons, holes, ionized dopants, and fixed charges. NextNano discretizes this equation using finite-difference methods on a nonuniform grid that is then solved through Newton–Raphson algorithms [86]. Boundary conditions typically include Neumann conditions at boundaries and Dirichlet conditions at contacts or interfaces for accuracy in capturing the electric field distribution and band bending.

Lattice mismatch between layers induces strain effect on electronic band structure through deformation potential theory. The strain tensor components $\varepsilon_{ij}(x)$ are computed using continuum elasticity theory, defined as [72,88]:

$$\epsilon_{ij} = \frac{1}{2}\left(\frac{\partial u_i}{\partial x_j} + \frac{\partial u_j}{\partial x_i}\right), \tag{32}$$

where $u_{ij}(x)$ are the displacement fields. Strain effects in heterostructures, especially on (111) substrates, involve complex hydrostatic and shear components, influencing conduction and valence band shifts. These shifts are represented by [88]:

$$E_c(x) = E_{c0}(x) + a_c\epsilon(x) E_v(x) = E_{v0}(x) + a_v\epsilon(x) \pm \Delta E_{split}\epsilon(x), \tag{33}$$

where $E_{c0}(x)$ and $E_{v0}(x)$ are unstrained band edges, a_c and a_v represent hydrostatic deformation potentials, and $\Delta E_{split}\epsilon(x)$ is strain-induced splitting due to shear strain. The resultant electrostatic and strain-adjusted conduction and valence band profiles form the potentials for solving the Schrödinger equations. Two levels of Schrödinger equations are considered: the single-band effective mass model and the multi-band k·p approach [86]. The single-band effective mass Schrödinger equation, useful for preliminary analyses or simpler cases, is represented in equation (14). For accurate simulations involving complex band alignments and anisotropic behavior typical in InGaAs/GaInSb QW heterostructures on GaSb(111) substrates, the multi-band k·p model is crucial. The 8-band k·p Schrödinger equation can be expressed as [86,92]:

$$H_{\text{k·p}}(x, -i\nabla)\psi(x) = E\psi(x), \tag{34}$$

where $H_{\text{k·p}}(x, -i\nabla)$ is the multi-band Hamiltonian containing conduction band, valence bands, and interband coupling terms. This matrix equation is solved using finite-difference

discretization to form a Hermitian eigenvalue problem [92], which includes proper boundary conditions to ensure physical correctness.

The incorporation of the Poisson, strain, and Schrödinger equations enables one to accurately capture the type-III (broken-gap) band alignment characteristics of InGaAs/GaInSb QW heterostructures grown on GaSb(111) substrates. The multi-band model provides a comprehensive description of complex band interactions and illustrates accurate resolution of the overlap between conduction and valence bands inherent in such structures, which can be found in Figure *31*. The comprehensive strain calculation and deformation potentials defines precise band offsets and alignments that directly influence carrier confinement and wavefunction distribution at the interfaces [86]. Accurate calculation of electrostatic potential profiles that derived from solving the Poisson equation further refine these band alignments, which incorporates realistic effects from doping profiles and piezoelectric fields prevalent in (111)-oriented structures [88]. These precise band alignments significantly influence the wavefunction overlap between electron and hole states. Accurately modeling this overlap dictates interband tunneling rates, carrier recombination efficiencies, and optical transition strengths, which are the fundamental parameters for device operation. The detailed analysis of this wavefunction overlap will be explored in the next section for energy state calculation within NextNano.

5.1.3 Energy state calculation

The quantized energy levels in the InGaAs/GaInSb QW heterostructure are obtained by solving the Schrödinger equation within the envelope-function framework as discussed in 5.1.2. Both the single-band effective mass approximation and the multi-band approaches are able to calculate electron and hole eigenstates. The multi-band framework is essential for materials with closely aligned or inverted bands, where strong coupling between conduction and valence bands occurs

[58]. For our simulation case, we used the single-band approximation to generate the energy state and determine the hybridization gap, and we used the multi-band approximation to validate the single-band result and the corresponding inversion symmetry. In this section, we outline how NextNano computes these energy states through describing the extraction of eigenenergies and sub-bands from both model's their numerical simulation result.

In the single-band envelope approximation, the Schrödinger equation reduces to a one-band (typically conduction-band) effective mass equation for the envelope function $\psi_n(x)$. Neglecting band coupling, one obtains a twofold (spin-degenerate) Schrödinger equation for electrons in the heterostructure. An analogous equation with a negative effective mass can be solved for holes in the valence band. Solving these separate single-band equations yields a set of electron sub-band energies $E_{e1}, E_{e2}, \ldots \ldots$ and hole sub-band energies $E_{h1}, E_{h2} \ldots \ldots$ with corresponding envelope wavefunctions confined in the quantum well through equation (17). Each eigenstate can be identified as electron- or hole-like based on whether its wavefunction is localized in the InGaAs layer or the GaInSb layer. However, the single-band model cannot capture any direct interaction between electron and hole states because the calculation treats them independently. This approach is computationally efficient and often reasonably accurate when bands are well separated, but it requires additional validation for strongly interacting or inverted band scenarios, such as for the coupled InGaAs/GaInSb QWs [58].

In the multi-band k·p approach, coupled Hamiltonians are solved for multiple conduction and several valence bands simultaneously. In this work, a full 8-band Hamiltonian k·p-like equation (34) is used. The electron wavefunction is represented as an 8-component envelope spinor of $\psi_c, \psi_{HH}, \psi_{LH}, \psi_{SO}$ for the conduction band, heavy-hole, light-hole, and split-off valence

bands respectively. The k·p envelope equations are matrix eigenvalue equations derived from [86]:

$$\widehat{H}_{8\times8}\Psi_n = E_n\Psi_n \tag{35}$$

where $\widehat{H}_{8\times8}$ includes kinetic energy with effective mass parameters and coupling terms between bands as well as band-edge potential offsets and strain effects. This multi-band Schrödinger equation is solved at $k_{\parallel} = 0$ (zone center) to find the quantized subband energies in the growth direction. Importantly, the multi-band eigenstates appear as mixtures of electron and hole characters. The lowest-energy state may have a significant heavy-hole component if the valence band edge is higher in energy in one layer. In essence, the k·p method produces hybridized electron–hole states when the band edges are close or inverted [86]. All relevant subbands are obtained in a unified calculation, and one can distinguish them by inspecting the dominant component of the wavefunction in each region. While the single-band model captures the basic confinement and effective mass properties, the k·p approach is essential to validate these results and ensure that the symmetry properties, especially the inversion, account for the anisotropy and nonparabolicity of the bands, and naturally includes the symmetry operations (such as inversion) inherent to the crystal lattice [86]. For our InGaAs/GaInSb QW heterostructure simulation, a k·p calculation can verify that the inversion of band ordering is robust, confirming our model that the potential profile and strain-induced shifts yield an inverted gap. Moreover, because the k·p basis functions are derived from eigenfunctions of the inversion operator, the method provides a sanity check on whether the simulation maintains (or appropriately breaks) inversion symmetry, which is a key aspect when analyzing topological phases [1].

In advanced heterostructure simulations like our InGaAs/GaInSb QW systems grown on GaSb(111) substrates, the interplay of strain, quantum confinement, and band alignment leads to

the formation of an inverted energy gap [6], which is the prerequisite for topological insulator behavior. The InGaAs/GaInSb heterostructure is designed such that the conventional ordering of the conduction and valence bands is reversed. In a single-band calculation, the effective potential $V(x)$ derived from the conduction band edge provides a first approximation of the confined electron states [60,86]. When the layer is grown on a GaSb(111) substrate, the maximum hydrostatic strain further shifts the band edges compared with the conventional GaSb(001) substrate [86]. This engineered shift can lead to a situation where the confined electron state in one layer lies energetically below the corresponding state in the adjacent layer and result in the formation of hybridization gap.

This section has reviewed the important theoretical concepts for band structure generation and energy state calculation in semiconductor nanostructures. Starting with the continuum models of electrostatics and strain, we have detailed the derivation and numerical solution of the single-band Schrödinger equation. The discussion then connected these methods to the multi-band k·p approach, which serves not only to enhance the quantitative results but also to validate symmetry properties such as inversion symmetry. In the context of InGaAs/GaInSb heterostructures on GaSb(111) substrates, these methods indicate how engineering strain and band offset can lead to the formation of a hybridization gap. The connection of efficient single-band calculations and symmetry-validated k·p simulations offers a comprehensive framework for analysis our simulation results, which will be presented in Chapters 6 and 7.

5.2 MATLAB interpolation for critical thickness

This section details a MATLAB-based simulation aimed at calculating the critical thickness h_c for InGaAs/GaInSb heterostructures across a range of compositions. As discussed in Section 4.3, the critical thickness is the maximum layer thickness below which a strained epitaxial film can

remain fully coherent on its substrate [10]. By mapping h_c over a compositional grid of varying In content in InGaAs, and Ga content in GaInSb, we established the design space within which layers can be grown without misfit dislocation formation. These simulations provide a matrix of h_c values for each pair of InGaAs and GaInSb compositions, serving as a guideline for NextNano simulation set-up and future MBE experiments. Ultimately, this MATLAB interpolation approach supplements the strain and band structure methodology by quantitatively defining the strain limits for the physical InGaAs/GaInSb QW system.

The structure shown in Figure *25*a consists of an InGaAs QW layer grown on a GaInSb QW layer., with AlSb barriers above and below. From a strain perspective, InGaAs has a smaller lattice constant than GaInSb[9], meaning InGaAs would be under tensile strain if grown directly on GaInSb. For the purposes of modeling the critical thickness, we conceptually invert the growth order of the top two layers. In other words, we treat the scenario as if GaInSb were grown on InGaAs purely to simplify the application of the strain formula. This reversal converts the tensile strain case into an equivalent compressive strain case of the same magnitude, allowing us to use standard critical-thickness equations without loss of generality. The Matthews–Blakeslee theory [10] of critical thickness is largely symmetric with respect to the sign of misfit strain, so this assumption does not change the predicted h_c; it simply ensures that all misfit strain inputs to our model are treated as positive values for numerical stability. After solving, we interpret the result as the critical thickness of the InGaAs film on GaInSb in the actual growth order, which will be shown in Chapter 7.

Accurate computation of misfit strain requires lattice constants and elastic parameters for each material as a function of composition. We obtained binary compound lattice constants and Poisson ratios from [9] and applied Vegard's law [94] to interpolate these values for the ternary

alloys. Vegard's law assumes a linear interpolation between endpoints, which are illustrated in equation (25) and (26). This linear approximation is reasonable for lattice parameters in III–V alloys and is commonly used in heterostructure modeling. In a similar fashion, composition-dependent Poisson's ratios were interpolated linearly. By doing so, the Poisson's ratio and other needed elastic constants for any intermediate composition are available. All interpolation results were validated to ensure they fall between the known values of the constituent binaries, with no significant bowing expected for these parameters [9]. Using these interpolated material parameters, the simulation captures how strain conditions evolve continuously across the compositional grid rather than only at a few discrete alloy compositions. With the lattice constants determined for each layer at a given composition, the next step is to calculate the lattice mismatch at each relevant interface in the layer stack. We consider three interfaces in our heterostructure: GaSb to AlSb (barrier on substrate), AlSb to GaInSb (first QW on first barrier), GaInSb to InGaAs (second QW on first QW), and InGaAs to AlSb(second barrier on second QW). The misfit strain f at an interface is defined in the conventional way as the relative difference in lattice constant between the film and the substrate, which has been illustrated in equation (28). This dimensionless quantity is positive when the film's natural lattice constant is larger than the substrate's (tensile strain in the film) and negative when it is smaller (compressive strain in the film). In our calculations, we use the magnitude of misfit strain and track the sign separately. For each interface, we compute misfit strain using the interpolated lattice constants based on equation (25). These values represent the lattice mismatch that would drive strain in each newly grown layer.

In our strain model, we assume each layer remains fully strained to match the substrate lattice up to its critical thickness. This means that the GaInSb layer initially adopts the in-plane

lattice constant of the AlSb and GaSb beneath it, and the InGaAs layer in turn adopts the in-plane lattice constant of the GaInSb layer, which is effectively dictated by AlSb as long as GaInSb is coherent [9,65]. The net effect is that the top InGaAs layer is strained relative to the GaInSb layer, which itself may be strained relative to AlSb, and AlSb relative to GaSb [10]. However, when solving for the critical thickness of the top layer, the primary driver is the local misfit at the GaInSb/InGaAs interface since misfit dislocations at that interface will relieve the strain in the InGaAs film. We ensure that the intermediate layers of AlSb and GaInSb are not driven beyond their own critical thickness in the range of compositions considered, so that our assumption of their coherence holds true. This approach isolates the calculation to the top interface. Effectively, we are finding how thick the InGaAs layer can be before it generates misfit dislocations, given the strain inherited from the underlying GaInSb.

To determine the critical thickness h_c for the InGaAs film at a given misfit, we employ the Matthews–Blakeslee equilibrium model [10]. Matthews and Blakeslee's theory balances the elastic strain energy in a coherently strained film against the energy cost of forming a misfit dislocation at the film/substrate interface. The result is a condition for mechanical equilibrium that can be expressed as a transcendental equation involving h_c. In simplified form for a 60° dislocation, which is the typical case in zincblende heterostructures, the equation is shown as equation (25). The left-hand side of equation (25) represents the force per unit length of dislocation line due to the film's elastic strain, and the right-hand side represents the resisting force per unit length due to the substrate interaction, proportional to film thickness times misfit stress. In equilibrium, beyond a certain thickness the driving force will equal the resisting force, and any additional thickness makes it energetically favorable for a dislocation to form and relieve strain [10]. That thickness is defined as the critical thickness h_c. Notably, h_c appears on

both sides of equation (25) (inside the logarithm and as a linear factor), which means the equation is transcendental and cannot be rearranged to solve for h_c in closed form. Instead, one must solve it iteratively. The formulation above is a slightly idealized form. In practice, Matthews–Blakeslee-style equations may include geometric factors for different dislocation types or account for differences in film/substrate elastic constants [10]. In our implementation, we assume a 60° misfit dislocation with a Burgers vector appropriate for the <111> orientation because our structure is grown on (111) GaSb. Thus, for each given misfit strain, we must solve equation (25) to find the corresponding critical thickness.

Because equation (25) cannot be solved analytically for h_c, we resort to a numerical root-finding approach. In MATLAB, this is accomplished with the *fsolve* function from the Optimization Toolbox. The function fsolve finds a solution h_c that satisfies $F(h_c) = 0$ for a given nonlinear equation $F(h) = 0$. We formulated $F(h) = 0$ based on equation (25) by bringing all terms to one side. In particular, the function is defined as:

$$F(h) = \frac{b}{2\pi f}\frac{1 - \nu\, cos^2\,\alpha}{(1+\nu)\, cos\lambda}(ln\frac{h_c}{b} + 1) \tag{36}$$

so that the critical thickness corresponds to $F(h_c) = 0$. The MATLAB implementation uses this function to compute $F(h) = 0$ for any trial thickness h_c. We supplied *fsolve* with an initial guess for h_c on the order of tens of nanometers. The choice of initial guess is not very sensitive in this problem because $F(h) = 0$ is a monotonic function for positive h_c given a fixed positive misfit strain. It starts negative at very small h_c and becomes positive at large h_c since the logarithmic term grows slowly while the linear $F(h)$ term dominates, so a root in between is assured by continuity. The solver uses a trust-region dogleg algorithm to refine the estimate of h_c. At each iteration, *fsolve* evaluates $F(h)$ and it adjusts to h_c to reduce the magnitude of $F(h)$. We configured the solver with tight tolerances to ensure a high-precision solution for h_c, given that

the critical thickness can vary over orders of magnitude across our compositional grid. We also limited the maximum iterations to a reasonable number. In all cases, *fsolve* converged to a positive real solution for h_c for compositions where the misfit strain is very small (approaching zero).

The above procedure is executed within a double loop over the composition variables. In our simulation, composition varies in increments across their ranges from 0 to 1 with a step-size of 0.1. The result is stored in a matrix with indices corresponding to the discrete values of composition. After the loops conclude, we have a complete 2D array of critical thickness values covering the entire compositional grid of interest. To present these results, the MATLAB code formats the output both as a matrix and as a table. All results are generated automatically by the MATLAB script, ensuring reproducibility. This interpolation and critical thickness calculation routine provides a correlation analysis between the theoretical strain model and practical growth considerations, guiding how we select compositions and layer thicknesses for experimental work in subsequent chapters.

6 Pre-simulation: InAs/GaInSb Result

This chapter presents a comprehensive pre-simulation study of InAs/GaInSb heterostructures to understand how key parameters of QW layer thickness, substrate orientation, and alloy composition impact the hybridization energy gap between the lowest confined electron energy state E_1 in the InAs QW and the lowest confined heavy-hole energy state HH in the GaInSb QW. The results will provide necessary information and reference for subsequent InGaAs/GaInSb heterostructure simulations, which will be presented and discussed in Chapter 7.

In Section 6.1, we analyze the (001)-oriented InAs/GaInSb system, where a systematic increase in the InAs thickness from 5.0 nm to 10.0 nm shows a clear trend: a large positive energy gap at smaller InAs thicknesses gradually decreases and eventually becomes negative. This result indicates the transition from a trivial state to a topological state. The analysis relies on single-band models that capture the QW thickness-dependence of the confinement energy to validate the theoretical predictions from earlier chapters. Section 6.2 extends this study to the same QW material system but with a (111) orientation, revealing how the enhanced symmetry and distinct strain distribution inherent to the (111) surface modify the quantum confinement effects. The thickness required to achieve band inversion is slightly shifted relative to the (001) case, and the multi-band dispersion diagrams reveal subtle differences in sub-band curvature and energy levels. These observations confirm that substrate orientation is an important tuning parameter for engineering topological properties. In Section 6.3, the focus shifts to the effect of GaInSb alloy composition while maintaining a fixed InAs thickness of 6 nm in the (111) orientation. We demonstrate that increasing the In content increases the tensile strain in the GaInSb layer and show that this tensile strain could help induce band inversion and enhance the hybridization gap.

The pre-simulation studies in this chapter offer insights into how to manipulate hybridization gap through engineering of QW thickness, alloy composition, and substrate orientation. These results serve as a foundation for optimizing material parameters and guiding future experimental efforts in the development of topological devices based on InGaAs/GaInSb heterostructures.

6.1 (001) InAs/ $Ga_{0.68}In_{0.32}Sb$: Effect of changing InAs QW thickness for a fixed GaInSb composition

In this section, we illustrate the pre-simulation results in Figure *33* for a fixed GaInSb composition of $Ga_{0.68}In_{0.32}Sb$ while varying the InAs layer thickness from 5 nm to 10 nm with a step-size of 1 nm. The focus is on the energy gap between the lowest electron sub-band (E_1) and the heavy-hole (HH) band. A change in sign of this hybridization energy gap from positive to negative indicates the transition from the trivial phase to topological phase, and the emergence of a robust edge state in these heterostructures with high spin-orbit coupling. These simulations was run for these QWs with a (001) substrate orientation. Figure 33 shows the band structure profiles for InAs thicknesses ranging from 5.0 nm to 10.0 nm with the conduction band edge (E_1) in the InAs QW, and the valence band heavy-hole (HH) state in the GaInSb QW clearly identified.

As discussed in Chapter 3, the energy levels in a QW can be approximated by the particle-in-a-box model. For a rectangular QW, the quantization of energy levels for electrons is given by equation (19). Because the electron effective mass is relatively small in InAs, E_1 is highly sensitive to changes in the InAs QW width. As the InAs thickness increases, the E_1 energy level decreases. Compared to E_1, the heavy hole in GaInSb has a much larger effective mass, which implies that the HH energy level is less sensitive to variations in the GaInSb QW width.

This differential sensitivity directly affects the hybridization gap, defined as the energy difference between E_1 and HH. At 4-5 nm InAs thickness, the band structures shown in Figure 33a-b illustrates a large positive separation between the E_1 state and the HH state consistent with a trivial insulating gap. The strong quantum confinement in the thin InAs layer pushes the E_1 state upward, which results in this relatively large hybridization gap and indicates strong electron confinement and minimal band mixing. As the InAs thickness increases, the quantum confinement effect weakens. The E_1 state shifts downward in energy while the HH state remains stable due to its larger effective mass and weaker sensitivity to the confinement. This results in a reduction in the hybridization gap. Figure 33c-d reveals this trend, where the gap between the confined E_1 and HH states narrows, until band inversion occurs in between these thickness configurations: in Figure 33c the E1 and HH states are almost degenerate and in Figure 33d we see a small inverted (i.e. negative) hybridization gap emerge. In the thicker wells, the confinement is significantly reduced. The downward shift of the E_1 state towards the conduction band edge continues, such that the size of the inverted energy gap between E_1 and HH increases, shown in Figure 33e-g. Figure 33g shows that the inverted hybridization gap is largest for the 10nm InAs QW band. This band inversion behavior reflects an increased coupling between the conduction and valence band states consistent with a transition from the trivial to topological state in the high spin-orbit coupling materials.

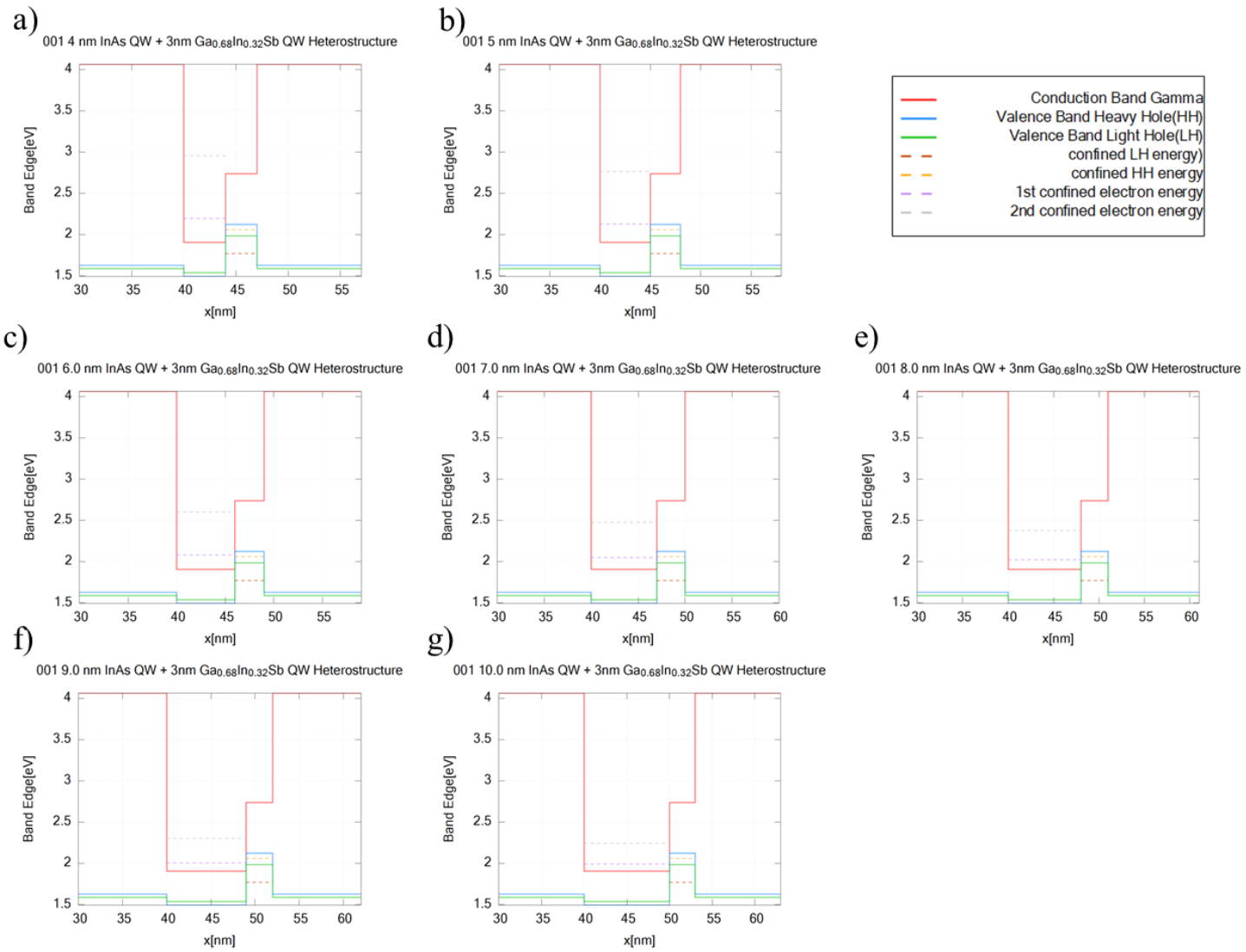

Figure 33 (a-g): Simulated InAs/$Ga_{0.68}In_{0.32}Sb$(001) band structures for InAs QW thicknesses from 4 nm to 10 nm with a step of 1 nm. The width and composition of the 3 nm $Ga_{0.68}In_{0.32}Sb$ QW is held constant in each.

InAs thickness (nm)	E_1 (eV)	HH (eV)	Energy gap (meV)
4	2.058	2.193	135
5	2.125	2.058	67
6	2.079	2.058	21
7	2.046	2.058	-12
8	2.022	2.058	-36
9	2.003	2.058	-55
10	1.989	2.059	-69

Table 1: Hybridization gap result s for 4-10 nm InAs/3nm $Ga_{0.68}In_{0.32}Sb$ band structure grown on (001) GaSb substrate.

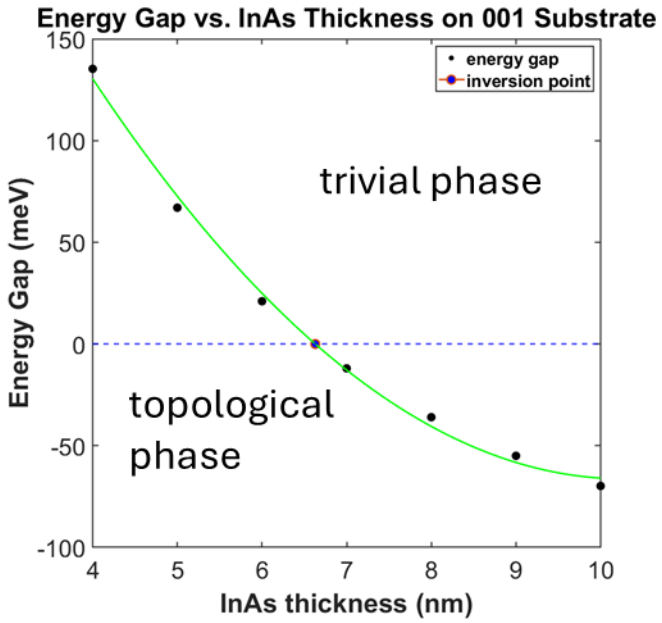

Figure 34: Energy gap as a function of InAs thickness interpolation from varied thickness InAs/3nm $Ga_{0.68}In_{0.32}Sb$(001) heterostructure on (001) substrate.

Table 1 shows the detailed hybridization gap results calculated from 5-10 nm InAs/3nm $Ga_{0.68}In_{0.32}Sb$ band structures grown on (111) GaSb substrate. The data quantify how the energy gap between E_1 and HH changes in both magnitude and sign. At smaller InAs thicknesses the gap is large and positive, which implies a trivial band ordering where the conduction band minimum lies above the heavy-hole band. Between 6 nm and 7 nm, the energy gap crosses zero. The result shows 21 meV at 6 nm and -12 meV at 7 nm, which suggests that band inversion lies in this range. Once the gap becomes negative, the conduction band is “pulled” below the valence band, leading to an inverted ordering associated with topological insulator behavior. From 7 nm

onward, the negative inverted hybridization gap continues to increase in magnitude. By 10 nm, the inverted gap is approximately -70 meV, indicating a strong band inversion. As discussed in Chapter 2, the inverted band structure is the indication of topological insulators, where robustness of edge states is related to the size of the inverted gap. Figure *34*

is the plot of the Energy Gap vs. InAs Thickness on the 001 substrate for further visualization of the relationship between the hybridization gap and InAs thickness. The plot is quadratic fitted with a polynomial function. A horizontal dashed line at 0 meV to emphasizes the trivial-to-topological transition. The gap decreases as the InAs thickness increases following a $\frac{1}{L^2}$ trend, which corresponds to the relationship from equation (17). From this fitting to the data we extract a thickness for the topological phase transition of 6.2 nm InAs. For InAs thicknesses below 6.2 nm, the system remains in a trivial state with positive energy gap, while for thicknesses greater than 6.2 nm, the gap becomes increasingly negative reflecting a progressively stronger band inversion that influences the size of the protected edge states and the material's robustness against perturbations.

By integrating these numerical data with the theoretical simulation, we gain a comprehensive understanding of how quantum confinement drives band inversion in (001)-oriented InAs/GaInSb heterostructures. The table and the plotted trend reveal the connection between layer thickness, confinement energy, and topological phase emergence, which also provide insights for the (111) oriented InAs/GaInSb heterostructure as a comparison reference.

6.2 (111) InAs/ $Ga_{0.68}In_{0.32}Sb$: Effect of changing InAs QW thickness for a fixed GaInSb composition

In this section, we analyze the results of simulated band structures for the (111)-oriented InAs/GaInSb QW heterostructures with a fixed GaInSb composition while varying the InAs layer thickness from 4 nm to 10 nm in the step of 1nm, which is same as section 6.1 except for the substrate orientation. Our focus is still on the energy gap between E_1 and the HH band that defines the hybridization gap. We also compare these results with the (001) orientation to evaluate the effects of substrate symmetry on quantum confinement and band inversion.

For the (111) orientation, Figure *35* illustrates the band structures at each thickness. These plots show the detailed positions of E_1 and HH to provide the visualization of the hybridization gap within the band structure. The band diagram for the thinnest 4 nm InAs QW layer from Figure *35*a shows a strong quantum confinement effect. The E_1 state is pushed significantly upward relative to the HH state and hence we observe a substantial positive hybridization gap. The confinement in the (111) plane is enhanced by the high symmetry of the (111) orientation, which can lead to a slightly larger energy separation than that observed in the (001) case at the same thicknesses. As the InAs layer thickness increase to 5 nm and 6 nm, the quantum confinement weakens, which results in a lower E_1 and therefore a smaller energy gap. The E_1 level shifts downward, predicted by the previous section and the mathematical relationship of $\frac{1}{L^2}$ dependence, and HH band still remains nearly unchanged because of its larger effective mass, shown in Figure *35*b-c. However, the hybridization gap appears to shrink slightly faster for the (111)-oriented structure compared to (001). For instance, the gap is still slightly positive at 5, but a small inverted gap appears by 6 nm that indicates the transition to the topological state. For InAs QW thicknesses above 6 nm, Figure *35*d-g show that the size of the negative inverted

hybridization gap increases, creating a more robust topological insulating phase. These data are summarized in Figure *36* and Table 2. Table 2 indicates that the gap drops through an exponential decay from +44 meV at 5 nm to -97 meV at 10 nm due to the quantum confinement theory discussed in Chapter 3. From our $\frac{1}{L^2}$ fitting to the data in Figure *36*, we extract an exact InAs QW thickness for band inversion of 5.9 nm for the (111) orientation. In section 6.1, the (001) orientation demonstrated a similar inversion phenomenon, but the exact thickness for band inversion was different. Band inversion for the (111) orientation with higher symmetry and different strain distribution, is shifted by a few tenths of a nanometer compared to the (001) orientation from 6.6 nm to 5.9 nm. Beyond 6.0 nm, the gap quickly becomes more negative and reaches -97 meV at 10 nm, representing a larger inverted hybridization gap than -69 meV from (001) orientation. Therefore, the numerical data and graphical illustrations confirm that the (111)-oriented InAs/GaInSb QWs reaches band inversion at a lower thickness and could create larger hybridization in similar thickness setting due to improved symmetry and strain effects along the (111) plane compared to the (001) orientation.

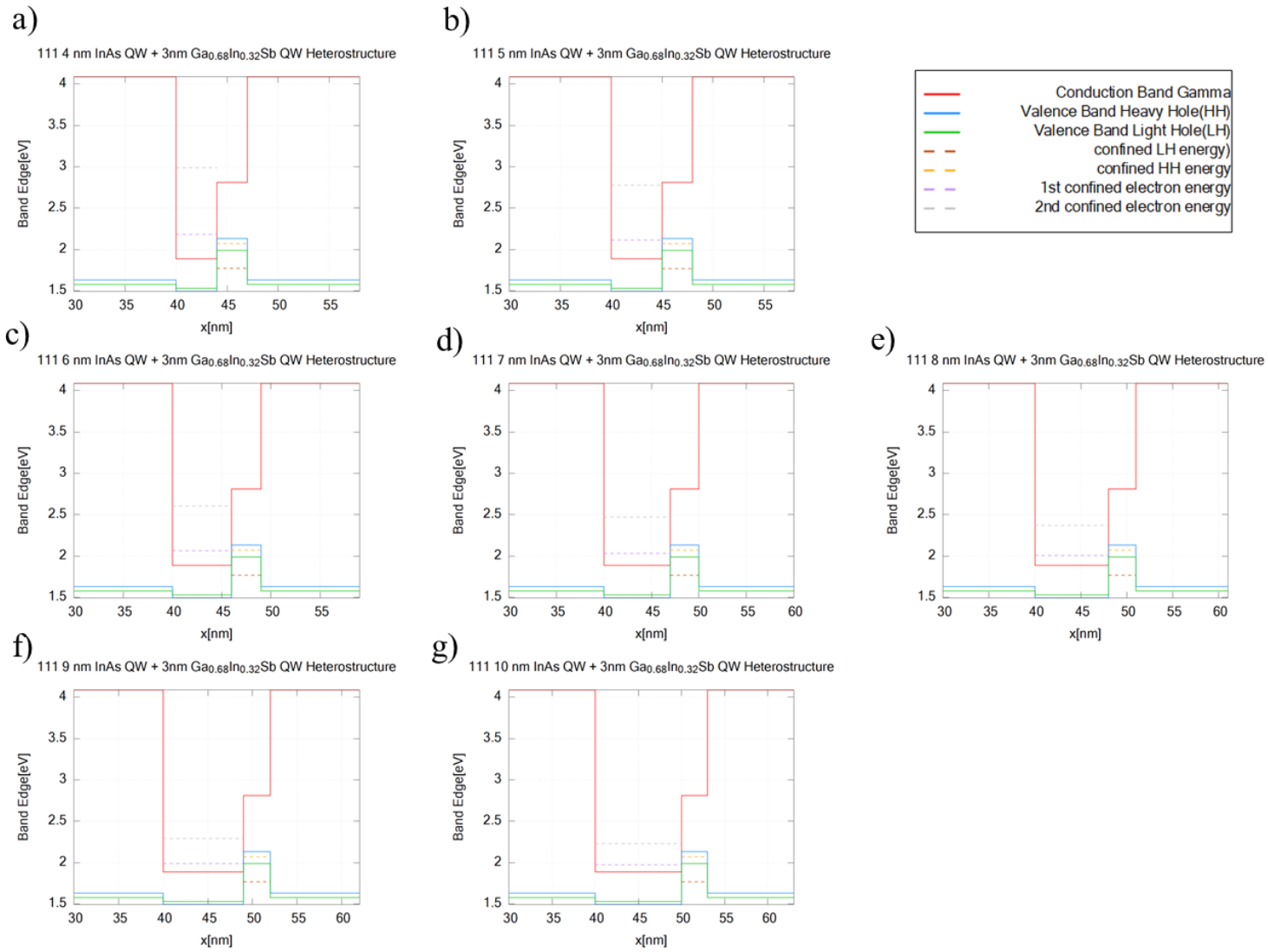

Figure 35: a-g: Simulated (111) InAs/$Ga_{0.68}In_{0.32}Sb$ band structure with varied InAs layer thickness from 4 nm to 10 nm with the step of 1 nm.

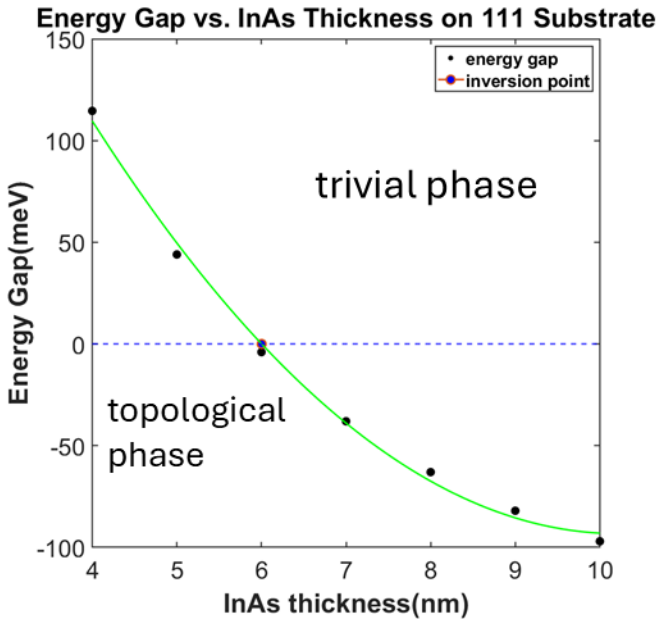

Figure 36: Energy gap vs. InAs thickness interpolation from variable thickness InAs/3nm $Ga_{0.68}In_{0.32}Sb$ heterostructure on (111) substrate.

InAs thickness(nm)	E_1(eV)	HH(eV)	Energy gap(meV)
4	2.183	2.069	114
5	2.113	2.069	44
6	2.065	2.069	-4
7	2.031	2.069	-38
8	2.006	2.069	-63
9	1.987	2.069	-82
10	1.972	2.069	-97

Table 2: hybridization gap result of 5-10 nm InAs/3nm $Ga_{0.68}In_{0.32}Sb$ band structure grown on (111) GaSb substrate

In addition to the single-band edge profiles where only E_1 and HH are tracked, the multi-band dispersion diagrams from 8 band k·p simulations provide a more comprehensive view of the band structure in momentum space. These diagrams plot several conduction and valence sub-bands as functions of the in-plane wavevector k to reveal important symmetries and confirm the presence (or absence) of band inversion. Figure *37* shows the energy bands appear symmetric about $k = 0$. This symmetry is the indication of TRS systems in the absence of external

magnetic fields or magnetization that we mentioned in Chapter 2. TRS requires that the energy eigenvalues satisfy $E(k) = E(-k)$ for all bands when spin-orbit coupling is included but no magnetism is present. Observing this symmetry in the multi-band dispersion indicates that the system respects TRS at the electronic structure level. Although the plots may not explicitly label spin-up and spin-down sub-bands, TRS guarantees that each electronic state at wavevector $+k$ and spin-up has a degenerate partner at wavevector $-k$ and spin-down. Near the center of the Brillouin zone, this degeneracy appears as band pairs touching each other. This behavior confirms the absence of any effective magnetic field or magnetic doping that would lift the Kramers' degeneracy. Figure *37*a shows that the conduction sub-bands lie distinctly above the valence sub-bands at $k = 0$ in 5 nm InAs, which confirms a positive energy gap that agree with the single-band edge analysis. In comparison, Figure *37*b for 7 nm InAs shows anti-crossing between conduction and valence sub-band at $k = 0$. The anti-crossing behavior reveals the system has entered the topological phase, which is also consistent with the single-band simulation result. Electrons states appear on these dispersion diagrams as regions where $d^2E/dk^2 > 0$ i.e. minima, while hole states occur where $d^2E/dk^2 < 0$ i.e. maxima. We can clearly see from Figure *37*b that at $k = 0$ this anti-crossing leads to electron states that lie below the heavy-hole states, indicating a large hybridization gap that matches our single-band results of strong inverted ordering. This effect is even stronger for a 10 nm InAs QW (Figure *37*c) where the valence-like states appear even higher in energy than certain conduction-like states at $k = 0$ confirming the robust inversion. Compared to the (001) orientation, the (111) orientation can affect the effective masses and the strain distribution within the quantum well. This leads to shifts in the curvature of the bands. Compared to the previous single band analysis, the multi-band analysis helps visualize anti-crossings that occur when conduction and valence states of

similar symmetry approach each other. The single-band diagrams only capture the minimum energy points, but the multi-band plots reveal how these states mix over a range of k. Observing a strong anticrossing or a distinct crossing at $k = 0$ confirms that an inversion of band order is taking place. Also, additional subbands can appear above or below the primary conduction or valence sub-bands. While these do not directly affect the hybridization gap, they are relevant for understanding spin-orbit splitting and excited-state phenomena.

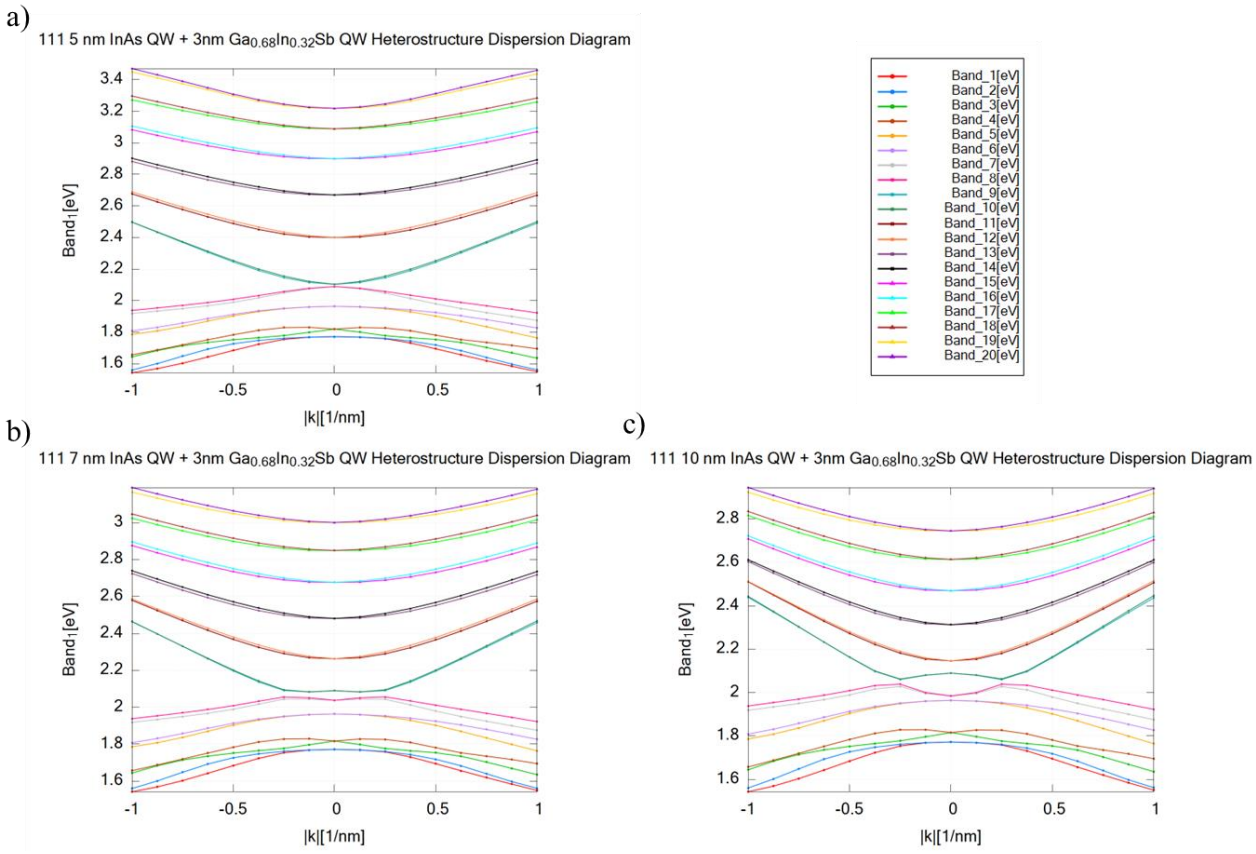

Figure 37 (a-c): Dispersion diagram of InAs/ $Ga_{0.68}In_{0.32}Sb$ on (111) substrate orientation with three different InAs thickness: (a) 5 nm InAs, (b) 7 nm InAs, (c) 10nm InAs thickness.

6.3 (111) InAs/ $Ga_{0.68}In_{0.32}Sb$: Effect of changing GaInSb composition for a fixed InAs QW thickness

In this section, we investigate how varying the alloy composition of the GaInSb QW layer with a fixed InAs QW thickness of 6 nm affects the hybridization gap between E_1 and HH. Figure 40 illustrates band diagrams of Ga compositions in $Ga_xIn_{1-x}Sb$ ranging from x = 0.53 to 0.83 to show the relationship between alloy composition and hybridization gap. The lattice constant of the GaInSb layer is interpolated between the lattice constant of GaSb and InSb. As the Ga content, x, decreases (i.e. the In content increases), the overall lattice constant increases. This variation serves to raise the lattice mismatch between the GaInSb layer and the underlying GaSb substrate. As we discussed in Chapters 3 and 4, strain from lattice mismatch can manipulate the band structure. Enhanced tensile or compressive strain affects the conduction and valence band edges through deformation potentials. In our coupled QW (111) heterostructure, a change in GaInSb composition shifts the lattice constant, which tunes the misfit strain experienced by both the GaInSb and the InAs layers. Figure *22* illustrates how the GaInSb lattice parameter changes with composition and hence how it will affect the band offsets at the heterointerface.

For low Ga content of 0.53-0.58 where the strain is highest (Figure *38*a-b), our simulated band diagrams show that the E_1 state appears below the HH state, implying a topological insulating state. Here, the conduction band edge is dominated by the compressively strained GaInSb layer whose lattice constant is closer to InSb, and the InAs quantum confinement is relatively modest at this profile. Table 3 summarizes the hybridization gap values extracted from the band diagrams, and we see large inverted gaps of -38 meV and -27 meV for the $Ga_{0.53}In_{0.47}Sb$ and $Ga_{0.58}In_{0.42}Sb$ QW composition profiles. As the Ga content increases, the lattice constant of the GaInSb layer decreases, reducing the compressive strain, and resulting in the shrinkage of the

negative inverted hybridization gap. Figure *38*c-d illustrates this trend by showing that the gap remains negative, but with decreased inversion magnitudes of -16 meV in $Ga_{0.63}In_{0.37}Sb$ and -4 meV in $Ga_{0.68}In_{0.32}Sb$ (Table 3) indicating a weakening of the band inversion compared to lower Ga compositions. At even higher Ga content, the compressive strain is further reduced and the resulting band diagrams from Figure *38*e-g reveal that a positive gap indicates the return to a trivial state with no topological phenomenon present in the structure. In Figure *39* we fit the data for Table 3 with a function that reveals the critical composition for achieving band inversion is $x \leq 0.7$ in this 6nm InAs/3nm $Ga_xIn_{1-x}Sb$ heterostructure. Furthermore, Figure *39* shows that reducing the Ga content in the GaInSb alloy increases the compressive strain that induces a larger hybridization gap. The resulting band inversion confirms that at lower Ga compositions the system enters a topological phase. This result provides implications for our simulations for InGaAs/GaInSb QW heterostructures.

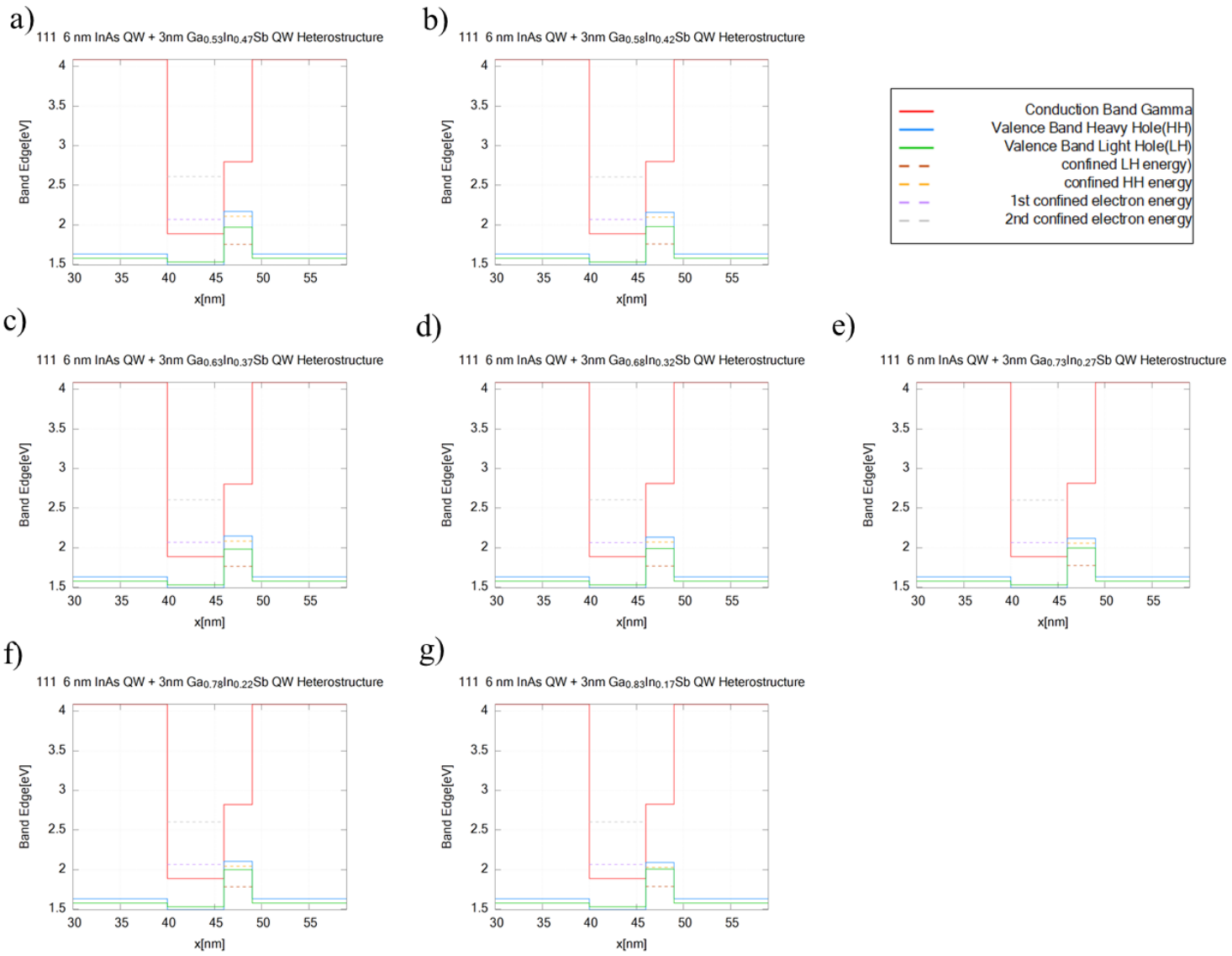

Figure 38: Simulated (111) InAs/$Ga_xIn_{1-x}Sb$ band structure with varied Ga alloy composition from 0.53 to 0.83 with the step of 0.05.

Ga content, x	E_1 (eV)	HH (eV)	E1-HH (meV)
0.53	2.0678	2.1061	-38
0.58	2.0668	2.0945	-27
0.63	2.0658	2.0822	-16
0.68	2.0649	2.0693	-4
0.73	2.0639	2.0556	8
0.78	2.0630	2.0412	21
0.83	2.0620	2.0260	35

Table 3: Hybridization Gap Values for a 6 nm InAs/3 nm $Ga_xIn_{1-x}Sb$(111) heterostructure.

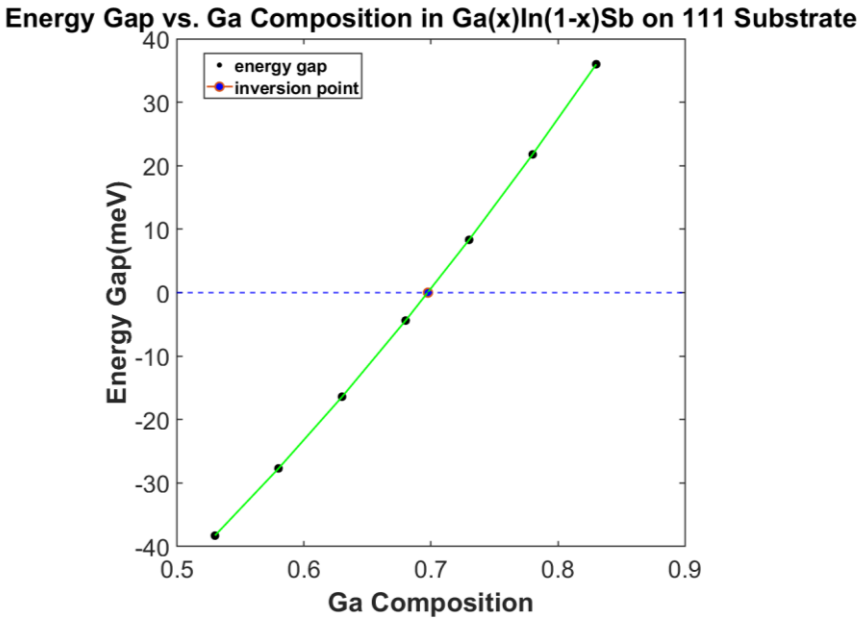

Figure 39: Energy gap vs Ga composition interpolation from varied composition 6nm InAs/3nm $Ga_xIn_{1-x}Sb$ heterostructure on 111 substrate.

7 Simulation results for (111) $In_xGa_{1-x}As/Ga_yIn_{1-y}Sb$ QWs as a function of thickness and composition

This chapter presents a detailed computational simulation of the $In_xGa_{1-x}As/Ga_yIn_{1-y}Sb$ QW heterostructure system with a view to maximizing inverted hybridization gaps for improved QSHI performance. Building on foundational concepts discussed in previous chapters, this chapter provides a comprehensive analysis of the simulated outcomes across a chosen parameter space involving QW layer thicknesses of 4–9 nm and alloy compositions of x and y ranging from 0 to 1. With the purpose of exploring the largest hybridization gap, we simplified the simulation process down to only (111) substrate based simulations are considered because Chapter 6 has indicated that (001) substrate based heterostructure will produce smaller hybridization gap compared to (111) substrate based heterostructure.

Section 7.1 investigates the impact of critical thickness constraints on the selection of viable heterostructures. Different layer growth sequences are considered because they reveal how growth order can influence allowable alloy composition and layer thickness through strain balancing. The differences in growth sequences are quantified through detailed critical thickness calculations that filtered impractical designs to ensure subsequent simulations focus on experimentally achievable configurations. A QW whose thickness exceeds the critical thickness for its particular compositional strain is excluded from subsequent simulations since, regardless of its hybridization gap, it could not be experimentally realized. This selective filtering reduces the extensive simulation space, which provides better clarity and efficiency in identifying optimal structures. Section 7.2 further refines this investigation by analyzing the simulation of hybridization gaps across the narrowed-down parameter set. After filtering through critical

thickness and inverted gap, we identify 209 combinations of coupled $In_xGa_{1-x}As$ / $Ga_yIn_{1-y}Sb$ QWs that exhibit the inverted band alignment required for a QSHI. A detailed comparative analysis demonstrates that heterostructures grown with the InGaAs layer deposited first exhibit larger achievable thicknesses, which implies enhanced inverted gaps due to the lowering of the confined electron ground state with increased QW width. Band structure simulations confirm that while growth order affects the practical growability of structures by influencing their critical thickness, it does not affect the inherent size of the hybridization gap when layers of identical thickness and composition remain coherently strained. Section 7.3 places these results within the broader context of past studies. By comparing our simulated hybridization gaps and structural designs to published experimental findings on similar strained layer heterostructures, we establish a clear validation of our results. The comparison shows that our obtained theoretical value of hybridization is larger than previous studies, which prove the importance of strain engineering and layer thickness tuning. These elements provide expectation into further MBE studies of advanced topological insulator heterostructures.

7.1 Critical Thickness Results

In this study, critical thickness calculations are necessary for narrowing down suitable QW structures for simulations of $In_xGa_{1-x}As/Ga_yIn_{1-y}Sb$ heterostructures. Critical thickness defines the maximum allowable epitaxial layer thickness before strain-induced misfit dislocations form. High quality, dislocation-free materials are a key requirement for robust QSHIs as we discussed in Chapter 4. We divided the simulation to explore growing the two QWs in different orders: 4-9 nm $In_xGa_{1-x}As$/4-9nm $Ga_yIn_{1-y}Sb$ and 4-9 nm $Ga_yIn_{1-y}Sb$/ 4-9nm $In_xGa_{1-x}As$. This allowed us to investigate the influence on strain distribution across the layers, and the resulting difference in allowable critical thickness values due to strain-balancing effects.

From Table 4 to Table 7, the misfit strain profiles and differences in critical thickness values are observed based on the growth order due to variations in lattice strain interactions between the adjacent layers. The strain balancing difference between the two growth orders can be explained through the misfit strain and lattice constants provided in Table 4 and Table 5. When InGaAs is grown first, the misfit strain is relatively large, even for low Ga content, which results in a smaller critical thickness. When GaInSb is grown first, the misfit strain remains relatively low for low In content alloys due to the closer lattice match between GaSb and AlSb, and so thicker QWs are allowed.

The first two columns in Table 6 show the critical thickness results for the situation where the $In_xGa_{1-x}As$ QW is grown first and strained by the underlying AlSb barrier. Critical thickness is reduced from 51.5 nm to just 1.9 nm as Ga content is increased from 0 to 0.2. This significant difference occurs because GaAs has a much smaller lattice constant of 5.653 Å compared to AlSb of 6.135 Å [9], which creates an increasingly large misfit strain as the Ga content in the InGaAs QW is raised. In contrast, the first two columns in Table 7 show the critical thickness results for the situation where the $Ga_yIn_{1-y}As$ QW is grown first and strained by the underlying AlSb barrier. The critical thickness for the GaInSb QW is reduced from 291.5 nm to 14.3 nm as the indium content is raised from 0 to 0.3. Although the difference in critical thickness is still large, the closer lattice constants of AlSb and GaSb (6.09 Å [9]) means that thicker layers can be grown compared to InAs-based QWs. Therefore, the growth order with InGaAs grown first exhibits tighter constraints in thickness due to the larger lattice mismatch. The strain balancing difference between the two growth orders can be explained through the misfit strain and lattice constants provided in Table 4 and Table 5. When InGaAs is grown first, the misfit strain is relatively large, even for low Ga content, which results in a smaller critical thickness. When

GaInSb is grown first, the misfit strain remains relatively low for low In content alloys due to the closer lattice match between GaSb and AlSb, and so thicker QWs are allowed.

$In_xGa_{1-x}As$ Composition	1	0.9	0.8	0.7	0.6	0.5	0.4	0.3	0.2	0.1	0
InGaAs Critical Thickness (nm)	51.5	21.3	12.4	8.3	6.0	4.6	3.4	2.8	2.3	1.9	1.6
InGaAs lattice constant (nm)	0.349	0.347	0.345	0.342	0.34	0.338	0.335	0.333	0.330	0.328	0.326
f	0.0065	0.013	0.0196	0.0261	0.0326	0.0391	0.0473	0.0538	0.0603	0.0669	0.0734

Table 4: $In_xGa_{1-x}As$ misfit strain result is aligned from GaSb to AlSb, then AlSb to InGaAs.

$Ga_yIn_{1-y}Sb$ Composition	1	0.9	0.8	0.7	0.6	0.5	0.4	0.3	0.2	0.1	0
GaInSb Critical Thickness (nm)	291.5	76.9	26.8	14.8	9.7	7.0	5.3	4.4	3.5	2.8	2.3
GaInSb lattice constant (Å)	3.516	3.539	3.562	3.585	3.608	3.631	3.654	3.671	3.695	3.718	3.741
f	0.0016	0.0049	0.0114	0.018	0.0245	0.031	0.0375	0.0424	0.0490	0.0555	0.0620

Table 5: I $Ga_yIn_{1-y}Sb$ misfit strain result is aligned from GaSb to AlSb, then AlSb to GaInSb.

Bottom InGaAs QW thickness (nm)		Top GaInSb QW thickness (nm)						
		$Ga_{1.0}In_{0.0}Sb$	$Ga_{0.9}In_{0.1}Sb$	$Ga_{0.8}In_{0.2}Sb$	$Ga_{0.7}In_{0.3}Sb$	$Ga_{0.6}In_{0.4}Sb$	$Ga_{0.5}In_{0.5}Sb$	$Ga_{0.4}In_{0.6}Sb$
51.5	$In_{1.0}Ga_{0.0}As$	26.7	14.8	9.7	6.9	5.2	4.1	3.3
21.3	$In_{0.9}Ga_{0.1}As$	9.7	6.9	5.2	4.1	3.3	2.7	2.2
12.4	$In_{0.8}Ga_{0.2}As$	5.2	4.1	3.3	2.7	2.2	1.9	1.6
8.3	$In_{0.7}Ga_{0.3}As$	3.3	2.7	2.2	1.9	1.6	1.4	1.2

Table 6: $In_xGa_{1-x}As/Ga_yIn_{1-y}Sb$ critical thickness results with only > 4 nm critical in consideration.

Bottom GaInSb QW thickness (nm)		Top InGaAs QW thickness (nm)						
		$In_{1.0}Ga_{0.0}As$	$In_{0.9}Ga_{0.1}As$	$In_{0.8}Ga_{0.2}As$	$In_{0.7}Ga_{0.3}As$	$In_{0.6}Ga_{0.4}As$	$In_{0.5}Ga_{0.5}As$	$In_{0.4}Ga_{0.6}As$
291.5	$Ga_{1.0}In_{0.0}Sb$	117.1	30.4	15.7	9.9	7	5.2	3.8
76.9	$Ga_{0.9}In_{0.1}Sb$	15.9	10.1	7.1	5.3	4.1	3.3	2.6
26.8	$Ga_{0.8}In_{0.2}Sb$	7.1	5.3	4.1	3.3	2.7	2.3	1.8
14.8	$Ga_{0.7}In_{0.3}Sb$	4.2	3.3	2.7	2.3	1.9	1.6	1.3
9.7	$Ga_{0.6}In_{0.4}Sb$	2.7	2.3	1.9	1.6	1.3	1.2	1.1

Table 7: $Ga_yIn_{1-y}Sb/In_xGa_{1-x}As$ critical thickness result with only > 4 nm critical in consideration.

Considering the critical thickness calculations, QW thicknesses greater than 4 nm will be considered in our simulation, while 3-4 nm will be marked for future reference if further investigation in that thickness range is needed. This criterion is based on two key factors discussed previously in Chapter 4, which are quantum confinement and practical growth considerations. Quantum confinement effects become available at thicknesses around or greater than 4 nm [8,65]. Layers less than 4nm is usually too weak to achieve the desired inverted band structures for robust QSHIs. Quantum confinement effects become pronounced at thicknesses around or greater than 4 nm. Thickness values below 4 nm also pose practical challenges for epitaxial growth precision and uniformity in MBE [77]. Such thin layers increase the risk of interface roughness, structural defects, and unintended interfacial alloying that negatively impact the quality of heterostructures. For each case in Table 6 and Table 7, QW combinations that yield a critical thickness > 4 nm are shown in green, while QWs with critical thicknesses of 3–4 nm appear in yellow, signifying that they lie on the borderline of what may be experimentally useful. QWs with a critical thickness < 3 nm appear in red indicating that they will not be included in our future band structure simulations. With the obtained critical thickness results, we can eliminate unwanted simulation combinations that are experimentally unachievable, allowing us to improve the reliability and applicability of the simulated results. The next sections will focus on hybridization gap results in growable composition/layer thickness combinations to identify which QW heterostructures could allow us to experimentally realize robust QSHIs.

7.2 4–9 nm $In_xGa_{1-x}As/Ga_yIn_{1-y}Sb$ Hybridization Gap Simulation Results

The full simulation set we carried out produced a total of 5930 hybridization gap data points for $In_xGa_{1-x}As/Ga_yIn_{1-y}Sb$ heterostructure, covering thicknesses from 4 nm to 9 nm, and covering the full composition range of x = 0–1 and y = 0–1 for both alloys. After applying the critical thickness criteria obtained in section 7.1, excluding combinations that could not be experimentally realized reduced this number to 347 data points if $In_xGa_{1-x}As$ is grown first and 451 data points if $Ga_yIn_{1-y}Sb$ is grown first. Among these results, just 104 data points of $In_xGa_{1-x}As$ grown first and 209 data points of $Ga_yIn_{1-y}Sb$ grown first exhibit an inverted gap value. This process shows the importance of the critical-thickness filtering discussed in section 7.1, allowing us to eliminate the majority of theoretically interesting combinations that are physically ungrowable, and leaving the focused subset of structures that can be realized without unwanted plastic strain relief via dislocations and other crystallographic defects.

The maximum inverted gaps in the final dataset are shown in Table *8*. The largest-hybridization gaps appear in the structure where the InGaAs QW is grown first and containing no Ga (i.e., pure InAs). From Table 4, although growing the InAs QW first results in lower critical thicknesses for high Ga-content GaInSb alloys in the top QW, it enables compositional options up to $Ga_{0.5}In_{0.5}Sb$. From the pre-simulation results in Chapter 6, lower Ga-content GaInSb will introduce additional compressive strain that could improve the hybridization gap size. In contrast, if the GaInSb layer is grown first, the subsequent InGaAs layer faces a larger lattice mismatch by straining InGaAs to a GaInSb lattice that limits the allowable InGaAs thickness and results in a smaller range of GaInSb compositions that could be used. Considering that the actual QW growth thicknesses will range from 4-9 nm (the range for our simulations), more applicable

composition combinations will enhance the flexibility in growth set up. The advantage of the InAs-first ordering is that it enables combinations of thick InAs and high In-content GaInSb that together produce stronger band inversion. Our simulations identify a 9 nm pure InAs bottom QW + 4 nm $Ga_{0.5}In_{0.5}Sb$ top QW heterostructure as the case with the largest hybridization gap of −147 meV. This structure's large inverted gap is achieved by growing InAs directly on the AlSb bottom barrier, which allows the 9 nm InAs QW to remain fully strained, while the 4 nm $Ga_{0.5}In_{0.5}Sb$ top QW also remains below its own critical thickness. However, if the growth order were reversed, the critical thickness of an InAs top QW on a $Ga_{0.5}In_{0.5}Sb$ bottom QW grown on the AlSb barrier falls below 3 nm due to the larger mismatch between the AlSb barrier and $Ga_{0.5}In_{0.5}Sb$ QW, which makes the growth of the structure unachievable. With that in mind, all the top-performing inverted-gap structures suggest that an InAs-rich bottom layer with a maximized QW thickness strained to the substrate, paired with a relatively thick, In-rich $Ga_xIn_{1-x}Sb$ top layer, is the arrangement that allows more moderate strain on InAs to push the design into a deep inversion regime. This outcome indicates how growth sequence can be exploited to explore optimized heterostructure design by strain limits.

InGaAs Thickness (nm)	In Composition in InGaAs	GaInSb Thickness (nm)	Ga composition in GaInSb	Hybridization gap (meV)	Bottom QW
9	1	4	0.5	-147	InGaAs
9	1	5	0.6	-137	InGaAs
8	1	4	0.5	-127	InGaAs
9	1	4	0.6	-125	InGaAs
9	1	6	0.7	-119	InGaAs
8	1	5	0.6	-118	InGaAs
9	1	5	0.7	-112	InGaAs
8	1	4	0.6	-105	InGaAs
7	1	4	0.5	-102	InGaAs
9	1	9	0.8	-102	InGaAs
9	1	4	0.7	-99	GaInSb

Table 8: Maximum hybridization gap result of filtered 4-9 nm $In_xGa_{1-x}As/Ga_yIn_{1-y}Sb$ and $Ga_yIn_{1-y}Sb/ In_xGa_{1-x}As$ QWs heterostructure. The top 10 results of InGaAs as bottom QW is shown. Only the largest result of GaInSb as the QW is selected because the gap size compared to results of InGaAs as bottom QW is much smaller and couldn't exceed the smallest value of the top 10 results.

The band diagram of the 9nm InAs/4nm $Ga_{0.5}In_{0.5}Sb$ heterostructure is illustrated in Figure 40, and it obtains the largest inverted gap of -147 meV in our simulation sets. Thickening $Ga_yIn_{1-y}Sb$ layer thickness while increasing In content contribute two parameters at same time that raises the valence band edge further to reduce its band gap, while the 9 nm InAs QW provides a low electron confinement energy. As a result, the overlap between the InAs conduction band and GaInSb valence band is more significant, shown in Figure 41. The E_1 state in the InAs quantum well lies low below the HH in the GaInSb layer, which reveals a large inverted gap for a strong topological effect. This structure with such a thick InAs QW can only be grown coherently in the InAs-first order because attempting to grow 4 nm of $Ga_{0.5}In_{0.5}Sb$ first would impose too large of a lattice mismatch with the AlSb barrier and hence exceed the critical thickness for this QW, as shown in Table 7.

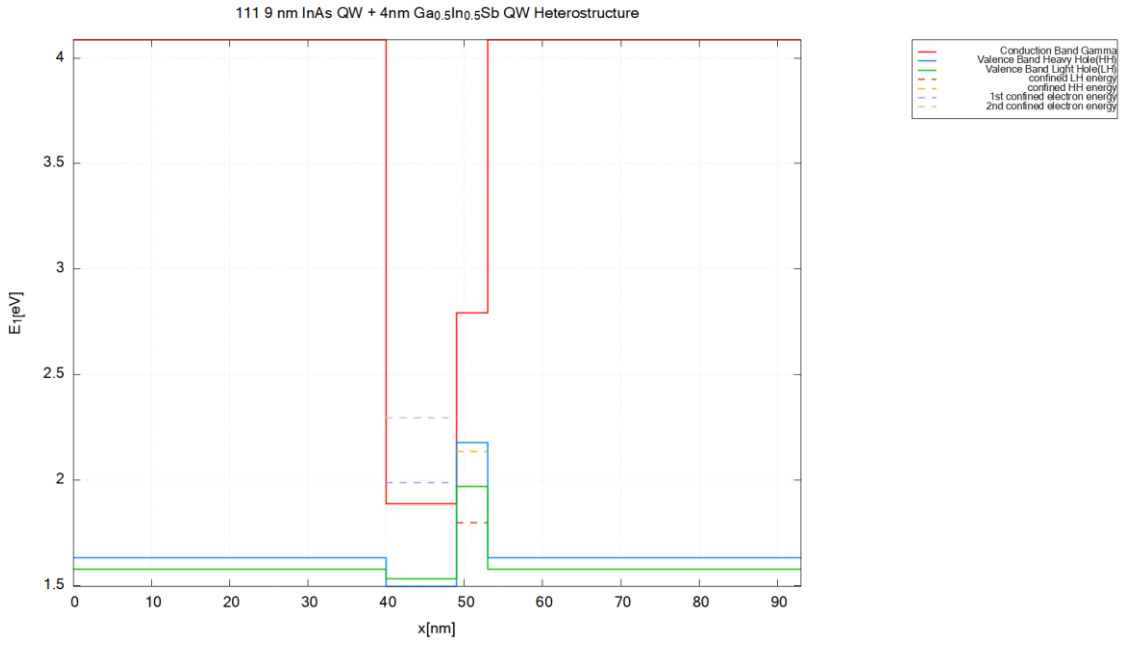

Figure 40: 9nm InAs/4nm $Ga_{0.5}In_{0.5}Sb$ QW band structure with discrete energy levels

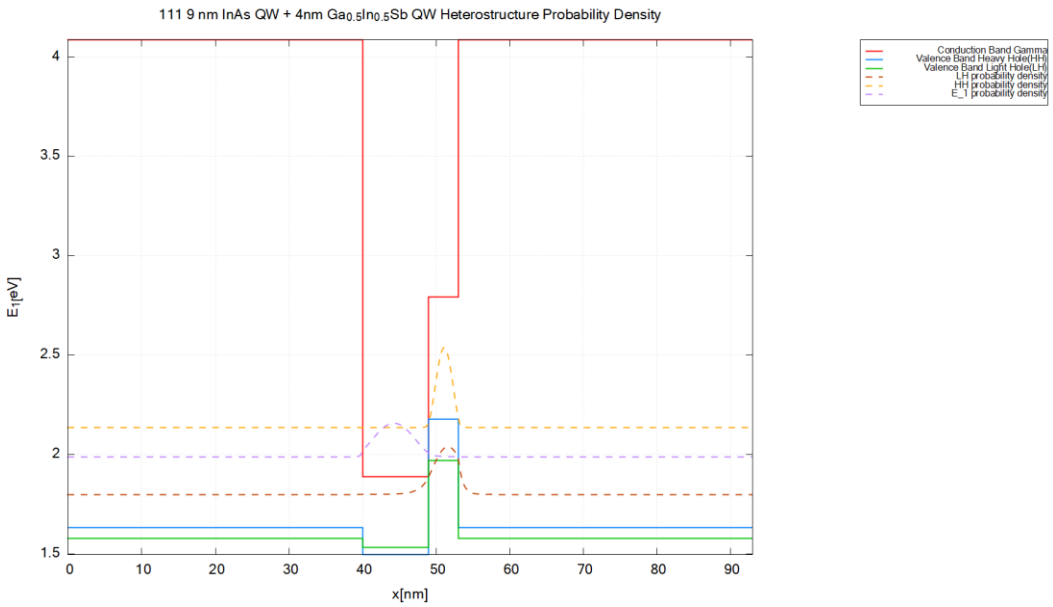

Figure 41: 9nm InAs/4nm $Ga_{0.5}In_{0.5}Sb$ QW band structure with SE solutions

The simulated band-edge diagram for a 4nm $Ga_{0.7}In_{0.3}Sb$/9nm InAs QW shown in Figure 42(a) is the thickness/composition combination that produces the largest result for the inverted gap if GaInSb is grown as the first (i.e., bottom) QW. The conduction band (CB) edge (Γ valley) is shown in red and the valence band HH edge in blue, as a function of position across the heterostructure. The $Ga_{0.7}In_{0.3}Sb$ QW on the left region has a higher valence band edge, while the InAs layer on the right region has a lower conduction band edge that leads to band overlap at the interface, shown in Figure *43*. Dashed lines indicate the quantized energy levels of the E_1 (purple) in the InAs well and the HH state (orange) in the GaInSb well. The electron level lies below the hole level indicating band inversion. This inverted band structure is obtained in our simulation assuming coherent strain. Figure 42b is the band-edge diagram for the same QW heterostructure, but with the InAs QW grown first on the AlSb barrier and the GaInSb QW deposited on top. The band profile is identical to Figure 42a with the same conduction-valence alignment and hybridization gap size (see Table *8*). This result confirms that when both layers remain fully strained to the bottom layer, the electronic structure is determined by the layer

thicknesses and compositions and not by the order in which they are grown, which is an important principle. What is more, in this InAs-first configuration, the thick InAs well is within its critical thickness limit due to the lower lattice mismatch of InAs on AlSb, and the 4 nm $Ga_{0.7}In_{0.3}Sb$ cap is also thin enough to remain coherent. The inverted band alignment could therefore be grown experimentally. In short, Figure 42 illustrates that growth order does not affect the band inversion or gap itself in the ideal coherent case, but the growth ordering will be important to discover more flexible heterostructure designs and enable more options for optimizing the hybridization gap.

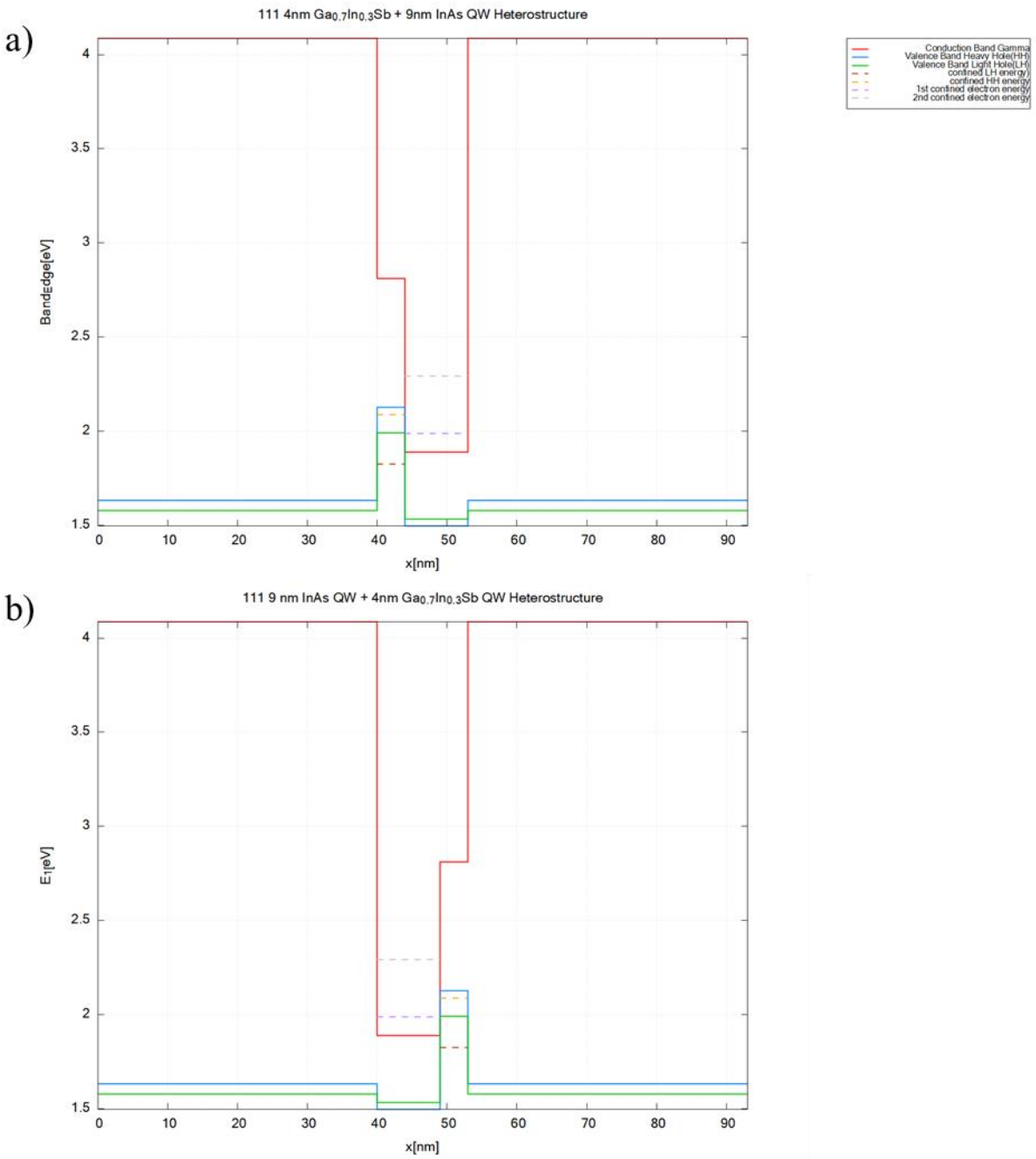

Figure 42: (a) 4nm $Ga_{0.7}In_{0.3}Sb$/9nm InAs QW band structure with discrete energy levels, and x = 0 is the beginning of AlSb barrier and the QW at x = 40 is $Ga_{0.7}In_{0.3}Sb$. (b) 9nm InAs/4nm $Ga_{0.7}In_{0.3}Sb$ QW band structure with discrete energy levels, and the QW at x = 40 is InAs.

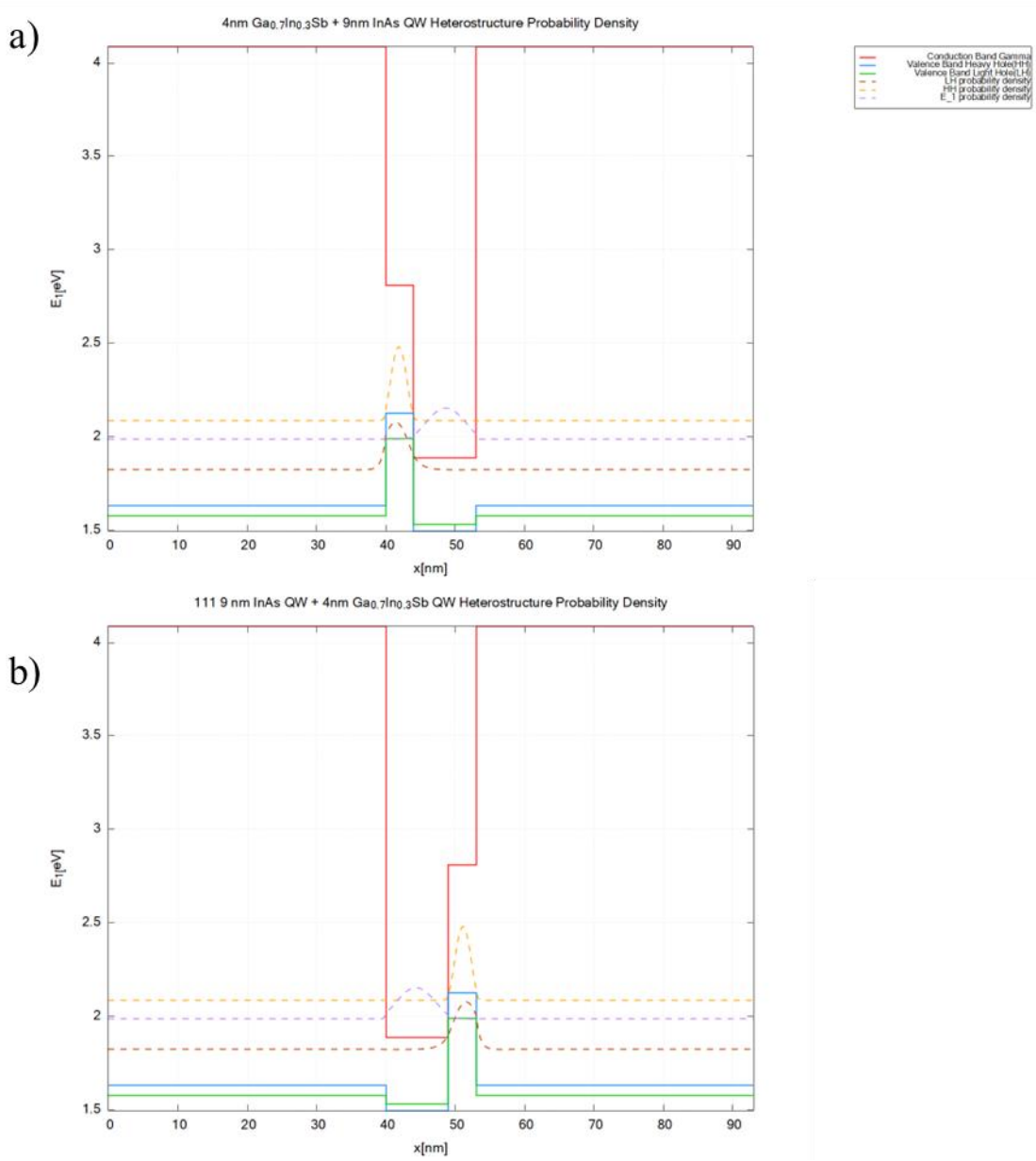

Figure 43: (a) 4nm $Ga_{0.7}In_{0.3}Sb$/9nm InAs QW heterostructure SE solutions (b) 9nm InAs/4nm $Ga_{0.7}In_{0.3}Sb$ QW heterostructure SE solutions

These results are verified through key concepts from earlier chapters. First, the propagation of strain and critical thickness is important because which layer is grown on the substrate first matters for whether each layer can remain fully strained. The principle is evident in the disparity between the two growth sequences. Even though the final strain state is the same (as the total strain will balance out in the final structure), only with correct ordering can that

structure be physically realized without relaxation, as we discussed in Chapter 4. The magnitude of the hybridization gap is governed by the interplay of quantum confinement and band alignment, which is also indicated by the pre-simulation result in Chapter 6. Thicker wells reduce quantum confinement energy in the electron subband, which lowers the conduction level closer to or below the valence level to create and increase band inversion. The alloy composition controls the band offsets to raise the valence band edge and increase the lattice constant to produce a stronger inversion if the resulting strain can be accommodated. The 9 nm InAs/4 nm $Ga_{0.5}In_{0.5}Sb$ result shows the connection of thick-layer confinement and band-offset engineering within the limits for strain tolerance. In summary, by combining optimal thicknesses and compositions within critical thickness limits, our simulations have allowed us to identify a narrow window of heterostructures that produce a significant inverted gap. This demonstrates how strain engineering together with band structure design could enhance hybridization gap size in $In_xGa_{1-x}As/Ga_yIn_{1-y}Sb$ QW heterostructures, and hence highlight their promise for synthesizing robust QSHIs.

7.3 Discussion

This section compares the simulation results of the $In_xGa_{1-x}As/Ga_yIn_{1-y}Sb$ heterostructures presented in this chapter with published studies through the analysis of how thickness and alloy composition will affect the size of hybridization gap. The comparison involves recent works on similar strained-layer QSHIs that focused on heterostructure designs, hybridization gap magnitudes, and strain-driven topological effects. In an inverted InAs/GaSb bilayer system [7] study, an experimental gap measurement around -2 meV was measured to present topological excitonic insulating behavior. Although this experimental study reveals smaller gaps than our simulated maximum gap values, the fundamental mechanism remains the same. The topological

excitonic insulator demonstrated inversion symmetry breaking at the electron-hole interface [7], which creates an excitonic gap in a similar physical mechanism to the band inversion-induced hybridization gaps modeled in our heterostructures. Our larger simulated gaps indicate that further strain and compositional optimization could enhance experimentally realizable gaps compared to the previously observed limits. What is more, the presence of quantized edge transport in their study confirms the viability of these heterostructures as practical platforms for topological device applications [7], further validating our proposed simulation designs.

Another experimental study of strained-layer InAs/GaInSb QWs reported an enhanced hybridization gap measurement up to approximately -20 meV [65], which is a tenfold increase compared to the previous binary InAs/GaSb structures. This improvement was achieved by introducing lattice strain effects from the In-alloyed GaInSb layer into the QW heterostructure with increased electron-hole wavefunction overlap. Their largest reported inverted gap at -20 meV aligns with our simulations, both for our InAs/GaInSb results from Chapter 6, and our $In_xGa_{1-x}As/Ga_yIn_{1-y}Sb$ results from this chapter, where increasing In-content in GaInSb (within the limits of strain relaxation) will significantly improve the size of the hybridization gap. The significantly larger hybridization gaps observed in our simulations underscore the importance of precise compositional tuning and optimized thickness within the critical thickness limits. While this past study experimentally validated the use of strained layer heterostructures to produce robust QSHIs [65], our theoretical simulations expand the range of achievable gaps through exploring the relation of alloy composition and layer thickness to suggest alternative, experimentally feasible designs that could increase the size of the inverted gap.

Another recent study also explored InAs/GaInSb composite QWs with varying In-content and thicknesses, and achieved experimentally measured hybridization gaps as large as -35 meV

[8] for highly strained QWs with the structure of 7.5 nm InAs/ 6nm $Ga_{0.6}In_{0.4}Sb$. This result is similar to the result we obtained in chapter 6, which is a simulated hybridization gap of -38 meV in 8 nm InAs/ 3nm $Ga_{0.68}In_{0.32}Sb$. The observed gap from [8] approaches the lower range of our theoretical simulations in our configuration with In-rich GaInSb QW layers. That paper's findings were concerned with dual gate-controlled topological phase transitions and resulting large gaps [8], which reinforces our simulations' premise. Furthermore, the measured gaps support our methodology by confirming the significant improvement potential that could be achieved by optimizing alloy compositions and structural parameters.

When comparing the inverted gap sizes from these experimental studies to our simulations, a notable observation appears: the roles that strain engineering and QW layer sequence play in achieving large hybridization gaps. Our simulation results suggest higher hybridization gaps up to ~137.6 meV are achievable through optimal composition and thickness selection that satisfy strain relaxation constraints. Compared to the largest experimentally reported gaps of approximately 20–35 meV, our larger simulated gap values suggest further practical implementation for enhanced QSHI device performance even though the exact gap value will not be matched. Our simulations assume perfectly coherent interfaces without defects, idealized lattice strain conditions, and abrupt interfaces with no atomic intermixing. Real heterostructures often exhibit atomic diffusion, interface roughness, and partial strain relaxation that could reduce the effective hybridization gap size [10,65,81]. The comparison to previous studies demonstrates that while previously published studies confirm and experimentally validate essential concepts such as strain-induced enhancement and hybridization-induced band inversion, the exploration in our simulations expand the tunability of parameter space. By optimizing alloy composition and exploiting layer growth sequences and thickness constraints,

our results offer theoretical prediction for future heterostructure designs aimed at maximizing inverted band gaps to push the limits of QSHI applications.

8 Summary

This thesis work has explored QSHIs in III–V semiconductor heterostructures. Previous deployment of QSHI-based devices from Chapter 2-4 has been restricted by the small hybridization gap in known materials, which limit the robustness of the device. Motivated by this challenge, the thesis set to design and investigate heterostructures that could support a large tunable hybridization gap while maintaining the necessary conditions for the QSHE. Utilizing insulating bulk and spin-polarized edge states from TIs, we designed the (111) $In_xGa_{1-x}As/Ga_yIn_{1-y}Sb$ QWs heterostructure in Chapter 7 to simulate how does different parameters such as QW layer thickness and alloy composition affect the size of hybridization, a direct representation of the topological property. The narrative of this research is providing material engineering insights of tunability of substrate orientation, QW thickness, and alloy compositions.

This work is motivated by the lack of tunable parameters and size optimization of hybridization gap. Past studies of well-studied binary InAs/GaSb system [7] only exhibit the a very small hybridization gap that merely past the trivial to topological phase transition, which means the corresponding robustness from the topological is relatively weak. In comparison, InAs/GaInSb binary/ternary system in recent studies [8,65,78] has shown the improvement in hybridization gap with a larger value of -35 meV has been obtained, but it still has not guaranteed a promising topological state. Prior to this work, there have been limited experimental studies on $In_xGa_{1-x}As/Ga_yIn_{1-y}Sb$ double ternary QW heterostructure due to the significant lattice mismatch between the binary endpoints (GaAs and InSb). By introducing tunable In and Ga content in both the As and Sb layers, the band structure can be adjusted through the broken gap alignment. At the same time, alloying induces strain in the layers because each composition has a different lattice constant. This strain engineering can improve the

hybridization gap by modifying band overlaps and splitting. On the other hand, excessive strain can lead to lattice relaxation through dislocations, which will destroy the topological state via rough surface morphology. Therefore, another objective of this research was to find an optimal balance: maximizing the beneficial strain for bandgap enhancement while staying within the critical thickness limits that preserve crystalline coherence.

A comprehensive methodology was developed for this study. The principles of critical thickness were well considered because critical thickness is the maximum film thickness that can be grown fully strained on a substrate without generating misfit dislocations. Exceeding this limit results in defects that degrade electronic properties and leads to elimination of the inverted band ordering required for topological insulation. By applying elasticity theory models [10] and material lattice profiles [9], the critical thickness for various $In_xGa_{1-x}As/Ga_yIn_{1-y}Sb$ heterostructure alloy compositions on was calculated. These calculations guided the design of heterostructure to filter impractical combinations of thickness and composition that would relax. Furthermore, this step ensured that the subsequent band structure simulations focused only on configurations that MBE is able to grow without losing the strain-induced advantages.

The focus of the research involved detailed simulations of the heterostructure's electronic band structure using the NextNano software. NextNano is able to self-consistently solve the Schrödinger and Poisson equations for the multilayer QW that includes the effects of strain and built-in fields. This allowed accurate modeling of the broken gap heterostructure, where the conduction band of one material overlaps with the valence band of the other. In addition, NextNano's multi-band k·p framework incorporates SOC and strain-induced band shifts to predict the emergence of the inverted band ordering and illustrate spin-momentum locking. Through applying different layer thicknesses and alloy compositions, the simulations mapped out

the conditions under which a topological state appears with identification of band inversion and a resultant hybridization gap in the energy spectrum. Together, these tools provided a virtual laboratory to explore a wider design space for QSHI heterostructures.

Another important insight from this work is the role of crystal orientation in maximizing topological effects. Based on the result in Chapter 6, the (111)-oriented heterostructures were found to enter the inverted region at thinner QW thicknesses and to produce larger energy gaps than their (001)-oriented counterparts. The high symmetry of the (111) crystal face also yields a more uniform in-plane strain distribution from the threefold rotational symmetry and different piezoelectric polarization effects, which benefits the band structure in. In our pre-simulation of InAs/$Ga_{0.68}In_{0.32}Sb$, the (111) orientation allowed the QW thickness for band inversion to shift from about 6.6 nm (001) down to 5.9 nm (111), and the inverted gap at a given thickness was consistently larger on (111). At 10 nm QW thickness the (111) structure's gap was about −97 meV, compared to −69 meV for (001). This orientation-dependent enhancement means that by simply choosing a different substrate cut, one can achieve a more robust topological insulating state without changing the material composition. It indicates the relationship between crystal symmetry, strain, and quantum confinement in these systems. Moreover, atomic arrangement in (001) GaSb materials have a mixture of III and V atoms in their surfaces that lacks a built-in electric field compared to (111) GaSb that have either a III or V atom terminated surface to generate an intrinsic electric field /polarization in the material.

The findings of this study shows potential improvement design of robust QSHIs. By using $In_xGa_{1-x}As/Ga_yIn_{1-y}Sb$ QW heterostructure, we have demonstrated the potential for larger hybridization gaps compared to previous study. Alloying proved to be a powerful tool through increasing the In content in $Ga_yIn_{1-y}Sb$ layer in particular improve the band inversion by

deepening the potential well for electrons and raising the energy of the HH states. Our simulations predict a hybridization gap on the order of -38 meV for a QW composed of 8 nm InAs and 3 nm $Ga_{0.68}In_{0.32}Sb$. This specific design was inspired by the best experimental report to date of -35 meV in a similar InAs/$In_{0.4}Ga_{0.6}Sb$ structure[8]. The simulations revealed that the largest hybridization gap is -137 meV. This result represent a major step a much more robust QSHI. Also, these extreme values lie at the edge of the strain stability window. In practice, material imperfections may reduce the gap, but the trend shows it is a promising improvement for the design of TIs.

In short, this thesis work delivers a comprehensive simulation studies of $In_xGa_{1-x}As/Ga_yIn_{1-y}Sb$ on (111)GaSb substrate heterostructure TIs. It reveals how band structure engineering in QWs through alloy composition, layer thickness, and crystal orientation can overcome current limitations and achieve larger hybridization gap. A larger gap QSHI can operate at higher temperatures and tolerate more disorder, which makes it suitable for spintronic devices that aim to use spin currents for logic and memory with low dissipation [4]. Moreover, the robust edge states in these engineered heterostructures could be interfaced with superconductors or magnets to explore quasiparticles and quantum computing elements [2], and the spin-momentum locked edges can serve for spin-based qubits or as a basis for fault-tolerant quantum bits [4]. In conclusion, this research has illustrated the design for QSHI on the purpose of hybridization gap improvement.

Bibliography

1. L. Fu and C. L. Kane, Phys Rev B Condens Matter Mater Phys **76**, (2007).

2. M. Z. Hasan and C. L. Kane, Rev Mod Phys **82**, 3045 (2010).

3. C. L. Kane and E. J. Mele, Phys Rev Lett **95**, (2005).

4. I. Žutić, J. Fabian, and S. Das Sarma, Rev Mod Phys **76**, 323 (2004).

5. Bernevig B. Andrei, Hughes Taylor L., and Zhang Shou-Cheng, Science (1979) **318**, 766 (2007).

6. C. Liu, T. L. Hughes, X. L. Qi, K. Wang, and S. C. Zhang, Phys Rev Lett **100**, (2008).

7. L. Du, X. Li, W. Lou, G. Sullivan, K. Chang, J. Kono, and R. R. Du, Nat Commun **8**, (2017).

8. H. Irie, T. Akiho, F. Couëdo, K. Suzuki, K. Onomitsu, and K. Muraki, Phys Rev Mater **4**, (2020).

9. I. Vurgaftman, J. R. Meyer, and L. R. Ram-Mohan, J Appl Phys **89**, 5815 (2001).

10. J. W. Matthews and A. E. Blakeslee, J Cryst Growth **27**, 118 (1974).

11. J. E. Moore and L. Balents, Phys Rev B Condens Matter Mater Phys **75**, (2007).

12. M. Freedman, C. Nayak, K. Shtengel, K. Walker, and Z. Wang, Ann Phys (N Y) **310**, 428 (2003).

13. L. Euler, Commentarii Academiae Scientiarum Petropolitanae **8**, 128 (1741).

14. D. J. Thouless, M. Kohmoto, M. P. Nightingale, and M. den Nijs, Phys Rev Lett **49**, 405 (1983).

15. B. A. Bernevig and S. C. Zhang, Phys Rev Lett **96**, (2006).

16. X. L. Qi and S. C. Zhang, Rev Mod Phys **83**, (2011).

17. J. Tian, I. Childres, H. Cao, T. Shen, I. Miotkowski, and Y. P. Chen, Solid State Commun **191**, 1 (2014).

18. S. S. Krishtopenko, Sci Rep **11**, (2021).

19. C. F. Schuck, R. A. McCown, A. Hush, A. Mello, S. Roy, J. W. Spinuzzi, B. Liang, D. L. Huffaker, and P. J. Simmonds, Journal of Vacuum Science & Technology B, Nanotechnology and Microelectronics: Materials, Processing, Measurement, and Phenomena **36**, (2018).

20. L. Casparis, M. R. Connolly, M. Kjaergaard, N. J. Pearson, A. Kringhøj, T. W. Larsen, F. Kuemmeth, T. Wang, C. Thomas, S. Gronin, G. C. Gardner, M. J. Manfra, C. M. Marcus, and K. D. Petersson, Nat Nanotechnol **13**, 915 (2018).

21. S. Y. Xu, C. Liu, N. Alidoust, M. Neupane, D. Qian, I. Belopolski, J. D. Denlinger, Y. J. Wang, H. Lin, L. A. Wray, G. Landolt, B. Slomski, J. H. Dil, A. Marcinkova, E. Morosan, Q. Gibson, R. Sankar, F. C. Chou, R. J. Cava, A. Bansil, and M. Z. Hasan, Nat Commun **3**, (2012).

22. C. Xu and J. E. Moore, Phys Rev B Condens Matter Mater Phys **73**, (2006).

23. F. Reis, G. Li, L. Dudy, M. Bauernfeind, S. Glass, W. Hanke, R. Thomale, J. Schäfer, and R. Claessen, Science (1979) **357**, 287 (2017).

24. M. V. Berry, Proceedings of The Royal Society A **392**, 45 (1984).

25. L. Fu and C. L. Kane, Phys Rev B Condens Matter Mater Phys **74**, (2006).

26. T. Fukui and Y. Hatsugai, J Physical Soc Japan **76**, (2007).

27. T. Fukui, T. Fujiwara, and Y. Hatsugai, J Physical Soc Japan **77**, (2008).

28. F. D. M. Haldane, Phys Rev Lett **61**, (1987).

29. G. W. Semenoff, Phys Rev Lett **53**, 2449 (1984).

30. Science (1979) **314**, 1754 (2006).

31. H. Zhang, C. X. Liu, X. L. Qi, X. Dai, Z. Fang, and S. C. Zhang, Nat Phys **5**, 438 (2009).

32. J. G. Checkelsky, Y. S. Hor, R. J. Cava, and N. P. Ong, Phys Rev Lett **106**, (2011).

33. Y. L. Chen, J. G. Analytis, J. Chu, Z. K. Liu, S. Mo, X. L. Qi, H. J. Zhang, D. H. Lu, X. Dai, Z. Fang, S. C. Zhang, I. R. Fisher, Z. Hussain, and Z. Shen, Science (1979) **325**, 178 (2009).

34. Y. S. Hor, A. Richardella, P. Roushan, Y. Xia, J. G. Checkelsky, A. Yazdani, M. Z. Hasan, N. P. Ong, and R. J. Cava, Phys Rev B Condens Matter Mater Phys **79**, (2009).

35. K. Von Klitzing, Review of Modern Physics **58**, 519 (1986).

36. K. von Klitzing, T. Chakraborty, P. Kim, V. Madhavan, X. Dai, J. McIver, Y. Tokura, L. Savary, D. Smirnova, A. M. Rey, C. Felser, J. Gooth, and X. Qi, Nature Reviews Physics **2**, 397 (2020).

37. C. D. Yerino, P. J. Simmonds, B. Liang, D. Jung, C. Schneider, S. Unsleber, M. Vo, D. L. Huffaker, S. Höfling, M. Kamp, and M. L. Lee, Appl Phys Lett **105**, 1 (2014).

38. D. Zhang, W. Lou, M. Miao, S. Zhang, and K. Chang, Phys Rev Lett **111**, 156402 (2013).

39. L. He, G. Bester, and A. Zunger, Phys Rev B **70**, 235316 (2004).

40. M. Buttiker, *Quantized Transmission of a Saddle-Point Constriction* (1990).

41. A. J. Bestwick, Quantum Edge Transport in Topological Insulators, Stanford University, 2015.

42. R. Jackie and C. Rebbi, Physical Review D **13**, (1876).

43. A. P. Schnyder, S. Ryu, A. Furusaki, and A. W. W. Ludwig, in *AIP Conf Proc* (2009), pp. 10–21.

44. C. Wu, B. A. Bernevig, and S. C. Zhang, Phys Rev Lett **96**, (2006).

45. T. Fan, N. H. D. Khang, S. Nakano, and P. N. Hai, Sci Rep **12**, (2022).

46. L. Liu, O. J. Lee, T. J. Gudmundsen, D. C. Ralph, and R. A. Buhrman, Phys Rev Lett **109**, (2012).

47. X.-J. Luo, W.-X. Qiu, and F. Wu, Phys Rev B **109**, (2023).

48. M. S. Lodge, S. A. Yang, S. Mukherjee, and B. Weber, Advanced Materials **33**, (2021).

49. R. Meng, L. M. C. Pereira, J. Van de Vondel, J. W. Seo, J. P. Locquet, and M. Houssa, ACS Omega **9**, 31890 (2024).

50. J. Haruyama, J Appl Phys **129**, (2021).

51. S.-Y. Hwang, R. Lopez, M. Lee, and D. Sanchez, Phys Rev B **90**, (2014).

52. B. R. . Nag, *Physics of Quantum Well Devices* (Kluwer Academic Publishers, 2006).

53. L. Esaki and R. Tsu, IBM J Res Dev **14**, 61 (1970).

54. H. Kroemer, Proceedings of the IEEE **51**, 1782 (1963).

55. J. P. Van Der Ziel, R. Dingle, R. C. Miller, W. Wiegmann, and W. A. Nordland, Appl Phys Lett **26**, 463 (1975).

56. R. Dingle, W. Wiegmann, and C. H. Henry, Phys Rev Lett **33**, 827 (1974).

57. P. J. S. Zory, P. F. Liao, and P. Kelley, *QUANTUM WELL LASERS* (Elsevier Science, Saint Louis, 2014).

58. C. Yi-Ping Chao and S. Lien Chuang, Phys Rev B **46**, 4110 (1992).

59. T. Takagahara and K. Takeda, Phys Rev B **46**, 15578 (1992).

60. E. Schrodinger, Physical Review **28**, 1049 (1926).

61. O. A. Pankratov, S. V. Pakhomov, and B. A. Volkov, Solid State Commun **61**, 93 (1987).

62. P. J. Simmonds and M. Larry Lee, in *J Appl Phys* (2012).

63. P. Atkins and R. Friedman, *MOLECULAR QUANTUM MECHANICS, FOURTH EDITION*, 4th ed. (Oxford University Press, 2005).

64. X. Qian, J. Liu, L. Fu, and J. Li, Science (1979) **346**, 1344 (2014).

65. L. Du, T. Li, W. Lou, X. Wu, X. Liu, Z. Han, C. Zhang, G. Sullivan, A. Ikhlassi, K. Chang, and R. R. Du, Phys Rev Lett **119**, (2017).

66. B. Huang, K. H. Jin, B. Cui, F. Zhai, J. Mei, and F. Liu, Nat Commun **8**, (2017).

67. Q. Liu, X. Zhang, L. B. Abdalla, and A. Zunger, Adv Funct Mater **26**, 3259 (2016).

68. A. Schliwa, M. Winkelnkemper, A. Lochmann, E. Stock, and D. Bimberg, Phys Rev B Condens Matter Mater Phys **80**, (2009).

69. C. D. Yerino, B. Liang, D. L. Huffaker, P. J. Simmonds, and M. L. Lee, Journal of Vacuum Science & Technology B, Nanotechnology and Microelectronics: Materials, Processing, Measurement, and Phenomena **35**, (2017).

70. H. Jiang and J. Singh, Phys Rev B **56**, 4696 (1997).

71. V. N. Kumar, M. Arivanandhan, G. Rajesh, T. Koyama, Y. Momose, K. Sakata, T. Ozawa, Y. Okano, Y. Inatomi, and Y. Hayakawa, NPJ Microgravity **2**, (2016).

72. J. Bardeen and W. Shockley, Physical Review **80**, 72 (1950).

73. A. R. Adams, IEEE Journal on Selected Topics in Quantum Electronics **17**, 1364 (2011).

74. B. Shi and K. M. Lau, *Growth of III–V Semiconductors and Lasers on Silicon Substrates by MOCVD* (Academic Press Inc., 2019).

75. T. P. Ginley, Y. Wang, and S. Law, Crystals (Basel) **6**, 154 (2016).

76. A. Maros, N. Faleev, R. R. King, C. B. Honsberg, D. Convey, H. Xie, and F. A. Ponce, Journal of Vacuum Science & Technology B, Nanotechnology and Microelectronics: Materials, Processing, Measurement, and Phenomena **34**, (2016).

77. T. D. Moustakas, MRS Bull **13**, 29 (1988).

78. T. A. Nilsen, M. Breivik, E. Selvig, and B. O. Fimland, J Cryst Growth **311**, 1688 (2009).

79. C. H. Li, O. M. J. Van't Erve, J. T. Robinson, Y. Liu, L. Li, and B. T. Jonker, Nat Nanotechnol **9**, 218 (2014).

80. J. E. Davey and T. Pankey, J Appl Phys **39**, 1941 (1968).

81. X. Chen, X. C. Ma, K. He, J. F. Jia, and Q. K. Xue, Advanced Materials **23**, 1162 (2011).

82. A. Richardella, D. M. Zhang, J. S. Lee, A. Koser, D. W. Rench, A. L. Yeats, B. B. Buckley, D. D. Awschalom, and N. Samarth, Appl Phys Lett **97**, (2010).

83. H. D. Li, Z. Y. Wang, X. Kan, X. Guo, H. T. He, Z. Wang, J. N. Wang, T. L. Wong, N. Wang, and M. H. Xie, New J Phys **12**, (2010).

84. J. Kiihn, K. T. Miiller, K. R. D. Peccei, A. E. Steiner, I. Triimper, G. P. W61fle, K. Honorary, E. A. Niekisch, J. Springer Berlin, H. New, Y. Barcelona, H. K. London, M. Paris, and S. Tokyo, *Applied RHEED: Reflection High-Energy Electron Diffraction During Crystal Growth.* (Springer, 1999).

85. Z. Chen, L. Zhao, K. Park, T. A. Garcia, M. C. Tamargo, and L. Krusin-Elbaum, Nano Lett **15**, 6365 (2015).

86. S. Birner, Modeling of Semiconductor Nanostructures and Semiconductor-Electrolyte Interfaces, TECHNISCHE UNIVERSITÄT MÜNCHEN, 2011.

87. R. Lake, G. Klimeck, R. C. Bowen, and D. Jovanovic, J Appl Phys **81**, 7845 (1997).

88. C. G. Van De Walle, *Band Lineups and Deformation Potentials in the Model-Solid Theory* (n.d.).

89. P. Y. Yu and M. Cardona, *Fundamentals of Semiconductors*, 4th ed. (Springer, 2010).

90. L. P. Kouwenhoven, D. G. Austing, and S. Tarucha, Reports on Progress in Physics **64**, 701 (2001).

91. M. E. Gurtin and A. I. Murdoch, Arch Ration Mech Anal **57**, 291 (1975).

92. D. M. Wood and A. Zunger, Phys Rev B **53**, 7949 (1996).

93. M. Governale and C. Ungarelli, Phys Rev B **58**, (1998).

94. V. L. Vegard, Zeitschrift Für Physik **5**, 17 (1921).